Proiectul P1: Caracterizarea mecanică a materialelor celulare și a structurilor sandwich cu miez din materiale celulare folosite la fațade inteligente

Parteneri: **Universitatea Politehnica Timișoara (Coordonator)**
Universitatea Tehnică de Construcții București, UTCB (P1)
Universitatea Tehnică Cluj Napoca (P2)

Etapa 1.3. Calibrarea unor modele de material pentru caracterizarea comportării mecanice ale materialelor celulare

Activitatea 1.3.1 Identificarea mecanismelor de cedare folosind termografia si corelare digitala a imaginilor

Metodele termografiei și corelării digitale a imaginilor (Digital Image Correlation, DIC) s-au aplicat pentru determinarea comportamentului materialelor folosite ca miezuri în diferite condiții de solicitare. Tehnica DIC utilizata este o tehnică fotomecanică pentru măsurarea in câmp complet a parametrilor de mișcare a suprafeței pentru diverse materiale, prin compararea imaginilor înainte si după deformare.

Efectul de crestătură în spumele poliuretanice rigide s-a studiat la solicitarea de compresiune a unor blocuri cu dimensiunea de 80x80 mm și grosimea de 25 mm, având prevăzute orificii de diverse diametre D = 16, 28 și 40 mm, Fig. 1.3.1.a. Epruvetele au fost solicitate la compresiune pe o mașină de încercat universala LBG de 100 kN, Fig.1.3.1.b. Testele s-au efectuat la temperatura ambiantă cu o viteză de solicitare de 10 mm/min. Pentru înregistrarea variației temperaturii de pe suprafața piesei s-a folosit un termograf FLIR AM40, fig. 1.3.2.

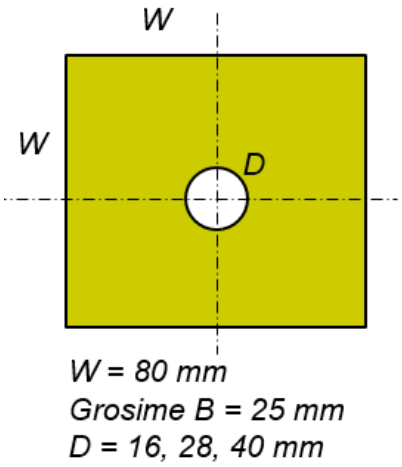

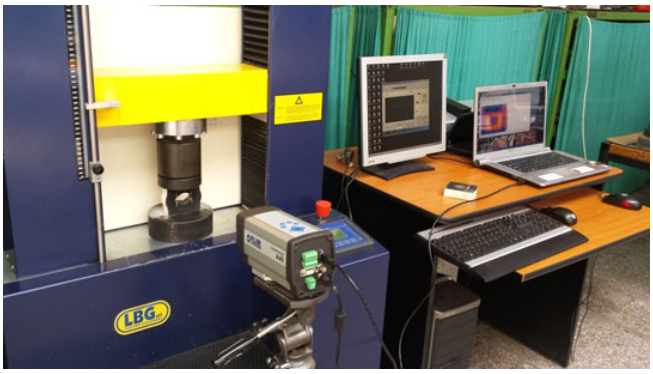

a. Epruveta b. Mașina de încercat LBG 100 și termograful FLIR AM40

Fig. 1.3.1 Teste de compresiune pe blocuri din spumă poliuretanică rigidă cu concentrator de tensiune

Curbele caracteristice pentru cele 3 spume analizate cu densitatea de 100, 145 și 300 kg/m^3 sunt prezentate în Fig. 1.3.2.a înregistrate la încercarea blocurilor cu diametrul de 16 mm. În Fig. 1.3.2.b se prezintă curbele forță deplasare de la încercarea blocurilor din spumă de densitate de 100 kg/m^3 pentru diametrul orificiului de 16, 28 și 40 mm.

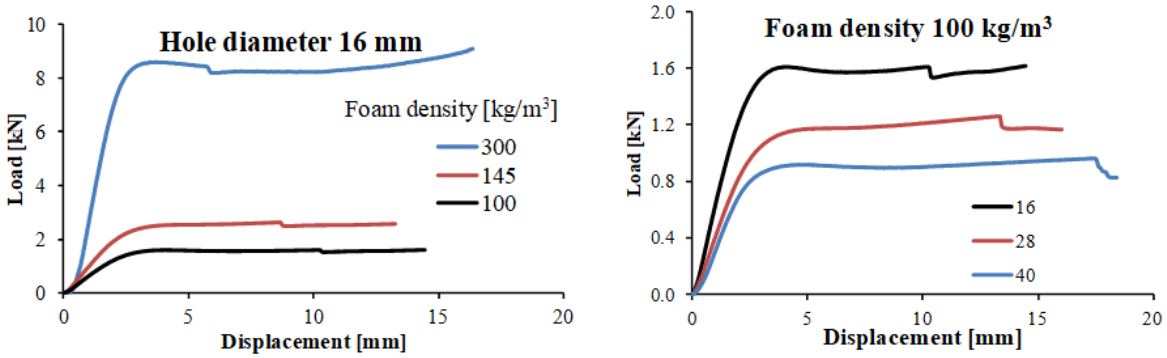

a. Influența densității b. Influența diametrului orificiului

Fig. 1.3.2 Curbe forță - deplasare de la încercarea la compresiune a blocurilor de spumă poliuretanică cu orificiu circular

Rezultatele experimentale arată creșterea proprietăților mecanice cu creșterea densității spumei, dar și scăderea acestora cu creșterea diametrului orificiului circular.

Pe baza rezultatelor experimentale obținute s-a studiat efectul de crestătură reprezentând raportul dintre tensiunea maximă și limita de curgere în funcție de raportul dintre diametrul orificiului D și lățimea epruvetei W, Fig. 1.3.3.

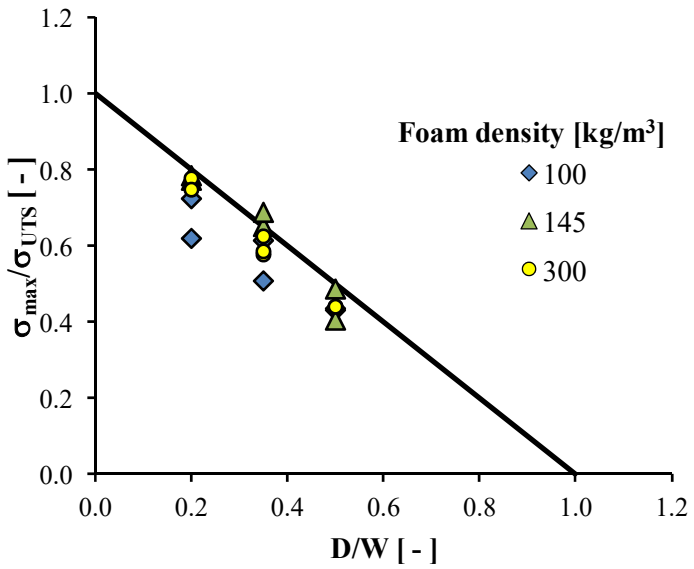

Fig. 1.3.3 Efectul de crestătură

Comportarea blocurilor de spumă cu orificii, diferă de cea a materialelor celulare fără crestătură prin faptul ca dispare porțiunea de densificare caracteristică solicitării la compresiune a spumelor, la finalul zonei de platou inițiindu-se ruperea prin propagarea unor fisuri. Celelalte două domenii cel elastic și de platou menținându-se. Această comportare este clar indicată de imaginile termografice prezentate în Fig. 1.3.4 pentru solicitarea la compresiune a blocurilor de spumă cu densitatea de 145 kg/m^3 și un orificiu cu diametrul de 16 mm. De la o deplasare de 8.5 mm se observă o creștere a temperaturii cu creșterea deplasării, corespunzătoare apariției planelor de deformație, orientate inițial la 45^0.

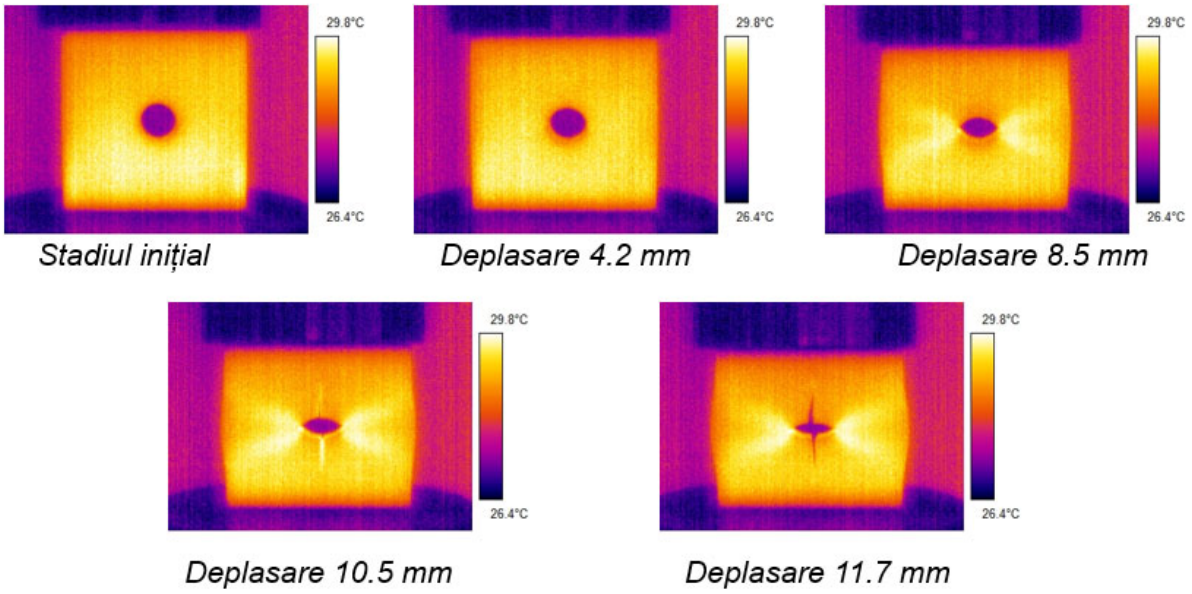

Fig. 1.3.4 Distribuția temperaturii în timpul solicitării la compresiune

Activitatea 1.3.2 Determinarea unor modele micromecanice de material pentru predicția proprietăților mecanice ale materialelor celulare.

În cadrul acestei etape s-au elaborat două lucrări științifice referitor la modelele micromecanice pentru estimarea tenacității la rupere a materialelor celulare. Una este o lucrare de sinteză în care se prezintă metodele experimentale, analitice (micro-mecanice) și numerice pentru determinarea tenacității la rupere a spumelor polimerice, [1]. Fig. 2.a. prezintă variația tenacității la rupere obținute experimental în funcție de densitate pentru diferite tipuri de spume (PUR, PIR, PVC) și modelul micromecanic Gibson – Ashby.

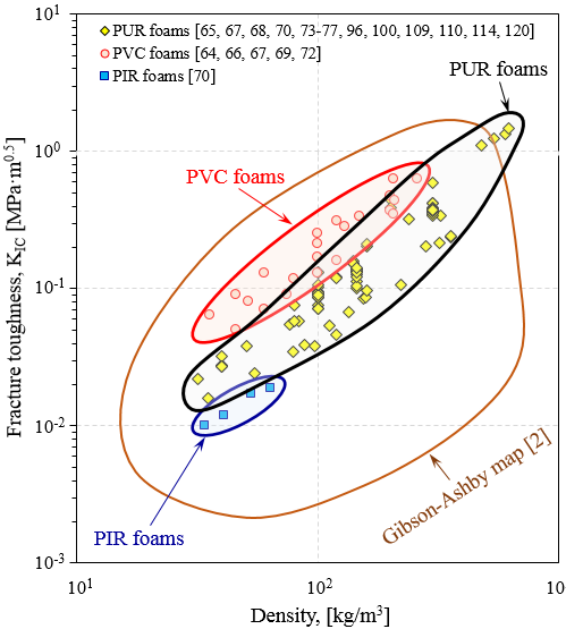

a. Tenacitate la rupere – densitate

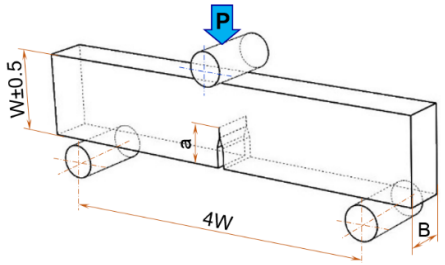

b. Încovoiere în trei puncte

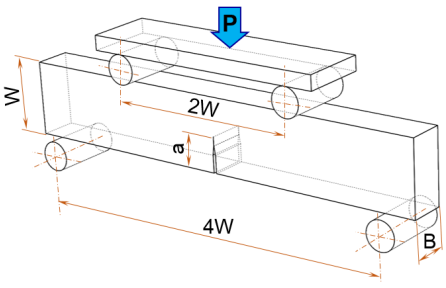

c. Încovoiere în patru puncte

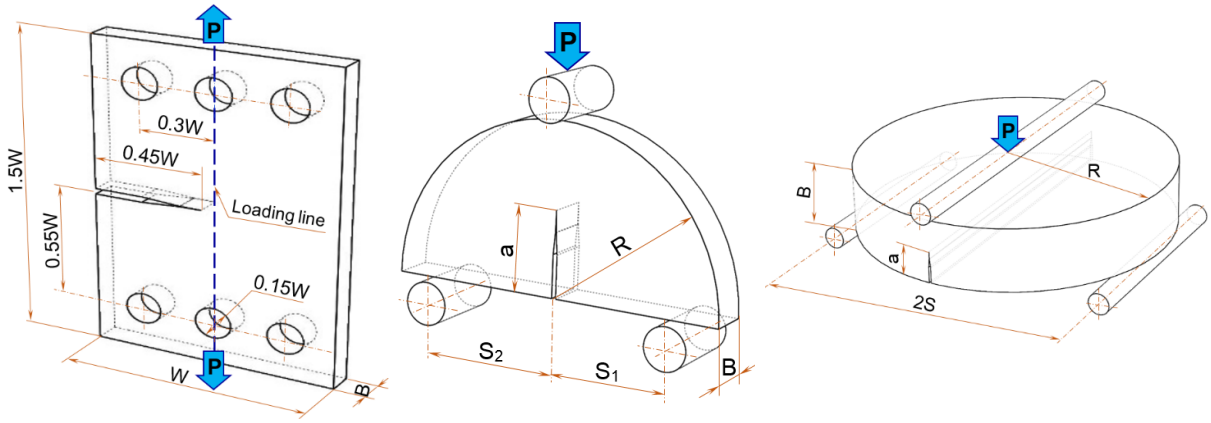

d. Epruvetă cu fisură laterală e. Epruvetă semicirculară f. Epruvetă disc

Fig. 1.3.5 Relația dintre tenacitatea la rupere și densitate și diferite geometrii de epruvete

Cele de-al doilea studiu reprezintă o analiză statistică a rezultatelor experimentale obținute pentru tenacitatea le rupere a spumelor PUR având densități de 100, 145 și 300 kg/m^3, [2]. S-au considerat cinci tipuri de epruvete solicitate la încovoiere in 3, respectiv 4 puncte (Fig. 2 b și c), la tracțiune cu fisură laterală (Fig. 2. d), epruvetă semicirculară cu fisură centrală solicitată la încovoiere în 3 puncte (Fig. 2. e), respectiv epruvetă tip disc cu fisură diametrală solicitată la încovoiere în 3 puncte (fig. 2.f). S-a studiat de asemenea influența vitezei de solicitare (considerând viteze de 2 și 50 mm/min) și direcția de aplicare a forței în planul de creștere al spumei, respectiv perpendicular pe acesta. Analiza statistică a indicat că tenacitatea la rupere nu depinde de tipul epruvetei și modul de solicitare, cea mai mare influență asupra tenacității o are densitatea, apoi o mai mică influență direcția de solicitare și practic nu a putut fi identificată o influență a vitezei de solicitare pentru vitezele considerate. Cel mai bun model micromecanic din punct de vedere statistic a fost unul exponențial de tipul:

$$K_{IC} = 0.0001430 \cdot \rho^{1.366}. \tag{1.3.1}$$

Mai multe detalii asupra acestor determinări sunt prezentate în articolele [1] și [2] atașate prezentului raport. Prima este o lucrare tip Review care face o sinteză a tenacității la rupere a materialelor celulare polimerice, foarte multe dintre aceste rezultate fiind obținute de membrii echipei de cercetare de la Universitatea Politehnica din Timișoara din cadrul Proiectului 1. Cea de-a doua lucrare prezentând o analiză statistică a datelor referitoare la tenacitatea la rupere a spumelor poliuretanice.

Activitatea 1.3.3 Calibrarea unor modele de material pentru simularea numerică a comportării structurilor tip sandwich.

Testele de compresiune a blocurilor de spumă puliuretanice au fost folosite pentru calibrarea unor modele de material pentru a fi utilizate la simularea comportării acestor materiale celulare. S-a considerat un model de material cu ecruisare izotropă, care utilizează o elipsă centrată în originea planului tensiunilor *p*-*q* pentru a reprezenta suprafața de curgere, Fig. 1.3.6:

$$q^2 + \alpha^2 p^2 = B^2 \tag{1.3.2}$$

unde p este tensiunea hidrostatică:

$$p = -\frac{1}{3} trace\, \sigma \tag{1.3.3}$$

q este tensiunea echivalentă Von Mises:

$$q = \sqrt{\frac{3}{2} S : S} \tag{1.3.4}$$

cu S tensiunea deviatorică:

$$S = \sigma + p\, I \tag{1.3.5}$$

iar mărimea elipsei de curgere măsurată pe axa q:

$$B = \alpha\, p_C = \sigma_C \sqrt{1 + \left(\frac{\alpha}{3}\right)^2} \tag{1.3.6}$$

unde: p_c este limita de curgere compresiune hidrostatică,
σ_c valoarea limitei de curgere la compresiune uniaxială,
α factorul de formă al elipsei care definește mărimea relativă pe cele două axe.
Curba evaluează păstrând forma și este guvernată de deformațiile plastice.

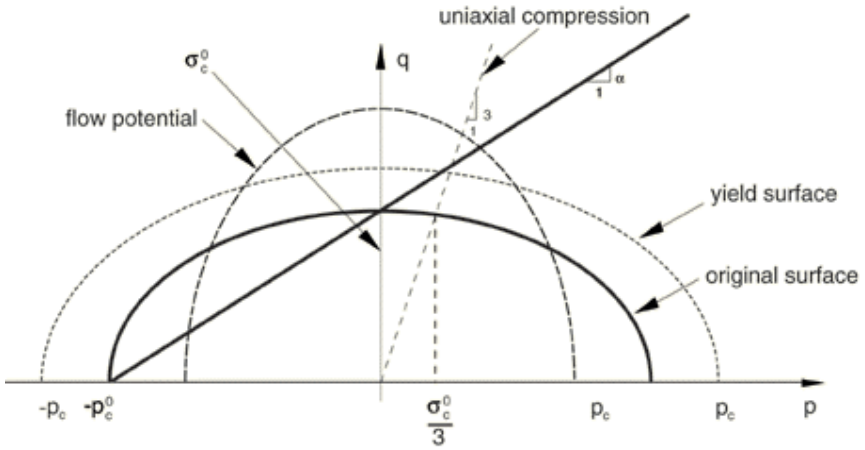

Fig. 1.3.6 Modelul de material cu ecruisare izotropă

Pentru calibrarea modelului s-a folosi un cub cu latura de 15 mm, Fig. 1.3.7. Modelul a fost discretizat în 3375 elemente paralelipipedice cu 8 noduri (C3D8) de mărime 1 mm, în urma unui un studiu de convergență.

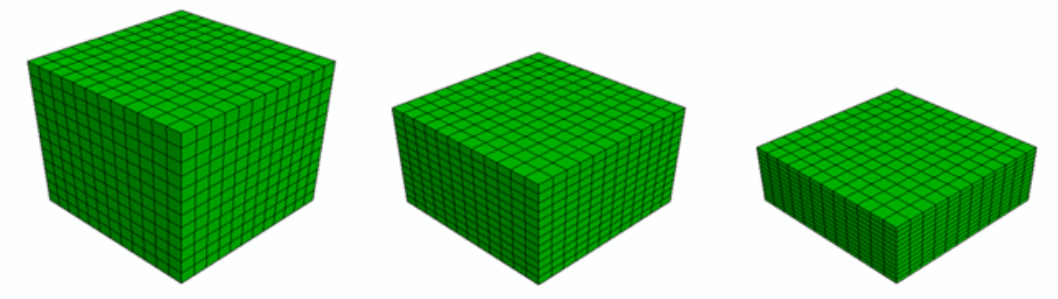

α. Inițial ε = 0 b. ε = 35% c. ε = 75%

Fig. 1.3.7 Modelul discretizat și deformarea cubului la diferite stadii de deformație

Apoi s-a trecut la modelarea blocurilor cu orificii, Fig. 1.3.8. acestea au fost discretizate cu ajutorul elementelor C3D8, rezultând 11850 elemente conectate în 13904 noduri. S-au impus condițiile de simetrie pe axele X și Z și o deplasare de 15 mm a feței superioare pe direcția Y.

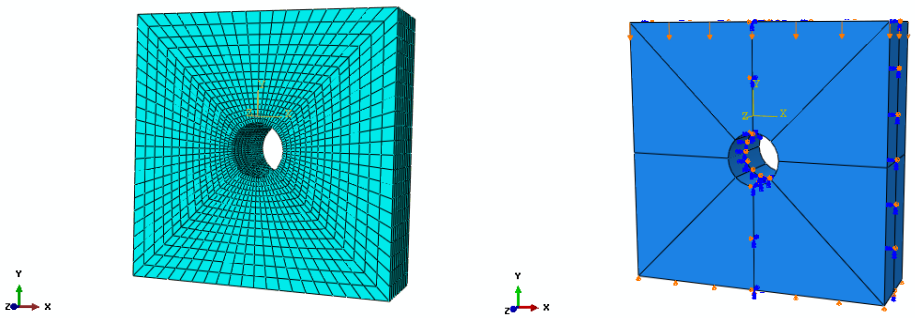

a. Discretizarea blocurilor b. Condițiile pe contur

Fig. 1.3.8 Modelul de calcul al blocurilor cu orificii

Rezultatele în urma analizei neliniare cu elemente finite sunt prezentate în Fig. 1.3.9: tensiunea echivalentă maximă, tensiunea principală maximă și deformațiile plastice echivalente.

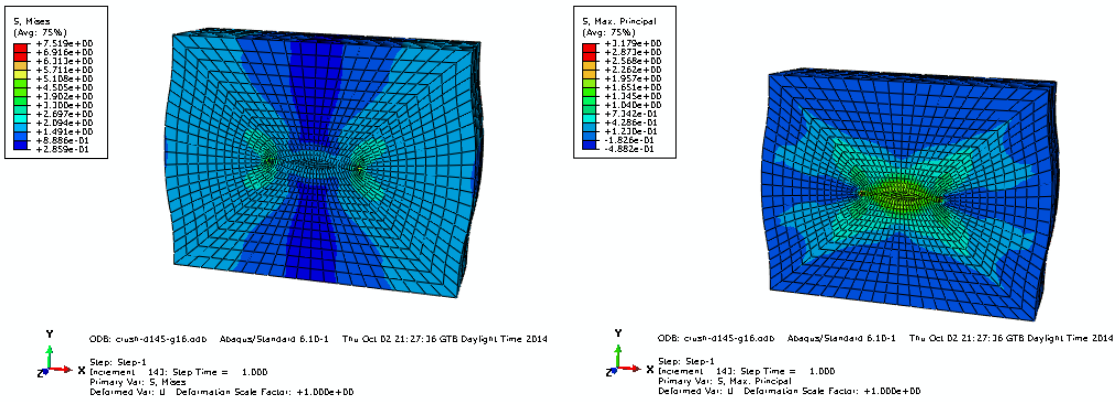

a. Tensiunea echivalentă Von Mises b. Tensiunea principal maximă

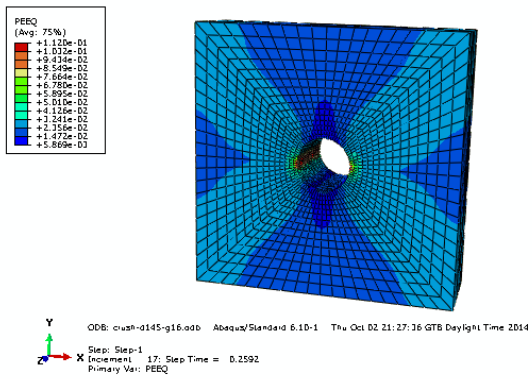

c.Deformațiile plastice echivalente

Fig. 1.3.9 Rezultatele simulării cu elemente finite a comportării blocurilor cu orificii

În Fig. 1.3.10 sunt prezentate comparativ curbele forță – deplasare de la încercarea la compresiune a spumelor cu densitatea de 300 kg/m^3 cu orificiu de 40 mm și rezultatele simulării. Se observă o bună corelare.

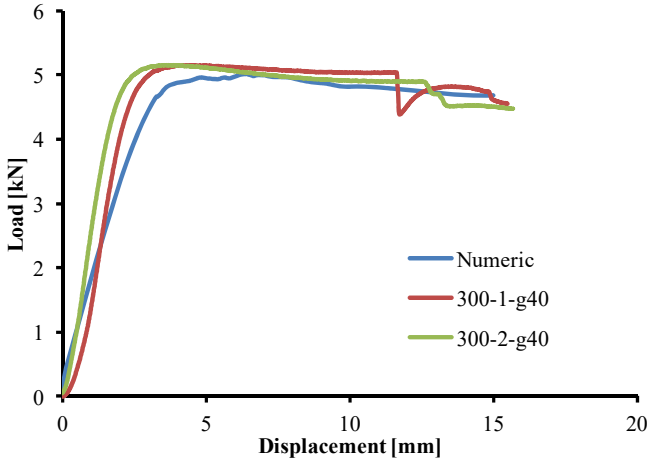

Fig. 1.3.10 Comparație între rezultatele numerice și cele experimentale

Degradarea structurilor de tip sandwich poate avea mai multe forme în funcție de parametrii geometrici (grosimea fețelor și a miezului, distanța dintre reazeme) și proprietățile materialelor utilizate. Principalele mecanisme de degradare sunt încrețirea fețelor (datorată compresiunii), ruperea fețelor (datorată întinderii), indentarea miezului (datorată solicitării de compresiune) și cedarea miezului (datorată forfecării).

Încercările experimentale au constat în teste de încovoiere în trei puncte pe structuri compozite având fețe de aluminiu și miez din spumă poliuretanică de două densități (100 kg/m^3 respectiv 300 kg/m^3). În scopul reducerii masei structurilor de tip sandiwch, au fost investigate și grinzi cu miez perforat. În timpul solicitării, aceste componente sunt supuse la stări complexe de triaxialitate a tensiunii datorate neregularității geometriei. În modelarea degradării spumei poliuretanice, s-a utilizat un model de degradare care presupune că deformația plastică critică este o funcție de viteza de deformație plastică, de starea de triaxialitate a tensiunii

Pentru a determina deformația plastică critică pentru diferite valori ale stării de triaxialitate a tensiunii s-au fabricat epruvete cilindrice din poliuretan cu diferite raze de racord [3] Fig. 1.3.11.a, acești concentratori determinând diferite stări de triaxialitate pentru fiecare tip de epruvetă. Asupra acestora s-au efectuat teste de tracțiune, rezultatele fiind prezentate în Fig. 1.3.11.b. Pe baza acestor rezultate, s-au efectuat analize numerice asupra unor modele având geometrii identice și ca model de material, o formulare elastic-plastică bazată pe curbele de tracțiune obținute anterior. Epruvetelor li s-a impus deplasarea critică determinată experimental, în acel stadiu înregistrându-se deformația plastică și starea de triaxialitate a tensiunii. Pe baza rezultatelor, s-a trasa o variație a deformației plastice critice cu starea de triaxialitate a tensiunii [3], Fig. 1.3.12.

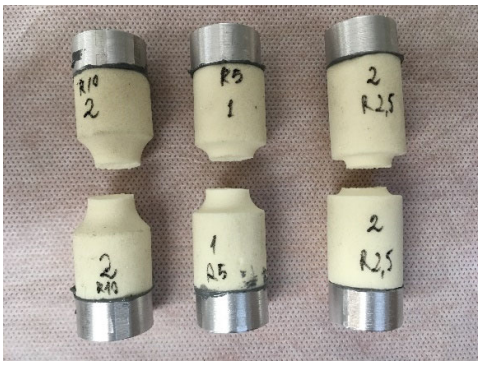

a. Epruvetele cilindrice din spumă poliuretanică rigidă

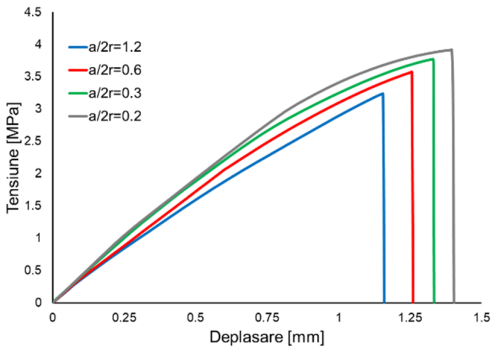

b. Curbele de tracțiune

Fig. 1.3.11 Determinarea deformațiilor critice pentru spuma poliuretanică

Pentru modelarea cedării structurilor tip sandwich s-a realizat o analiză cu elemente finite folosind soft-ul Abaqus Explicit, [3]. Structura tip sandwich a fost realizată din două fețe din aluminiu de 1,5 mm, lipite cu ajutorul a două straturi de adeziv de 0,5 mm de miezul din spumă cu grosime de 28 mm compact, respectiv cu găuri de 7,5 și 18 mm diametru, Fig. 1.3.13.a. Reazemele au fost considerate cilindri rigizi cu raza de 20 mm, iar aplicarea forței s-a realizat cu un cilindru de rază 30 mm (pentru a reduce indentarea), Fig. 1.3.13.b. Aluminiul și adezivul au fost modelate utilizând formulări elastic-plastice, obținute din teste de tracțiune (epruvetele de aluminiu au fost frezate din tablele utilizate pentru fețe iar epruvetele de adeziv au fost turnate în forme). Modelelor elasitc-plastice ale aluminiului respectiv adezivului li s-au adăugat modele de degradare bazate pe formularea Johnson-Cook.

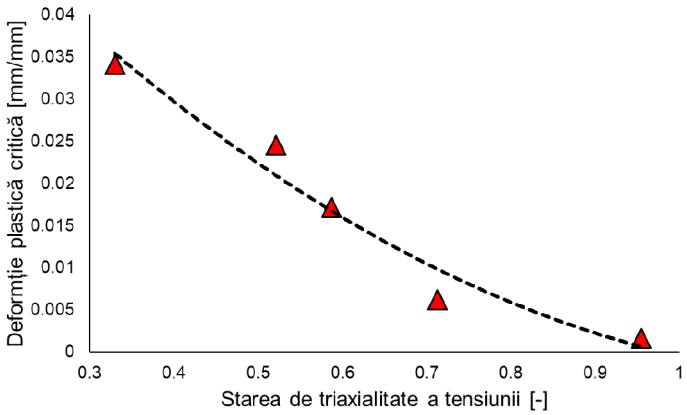

Fig. 1.3.12. Variația deformației plastice critice cu starea de triaxialitate a tensiunii pentru spuma poliuretanică

În urma analizelor numerice s-au replicat modurile de cedare ale structurilor de tip sandwich pentru fiecare configurație: ruperea miezului (în cazul structurilor cu miez compact de densitate 100 kg/m^3, Fig. 1.3.13.c), indentarea miezului (în cazul structurilor cu miez compact de densitate 300 kg/m^3, Fig. 1.3.13.d) respectiv forfecarea miezului (în cazul structurilor cu miez perforat pentru ambele densități, Fig. 1.3.13 e și f)

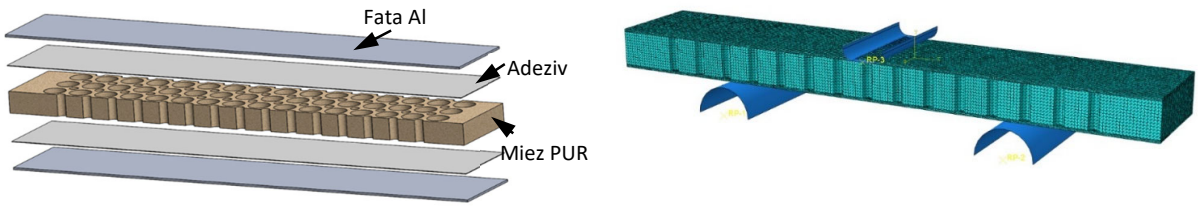

a. Modelul numeric (fețe oțel, miez spumă PUR, adeziv)

b. Discretizare

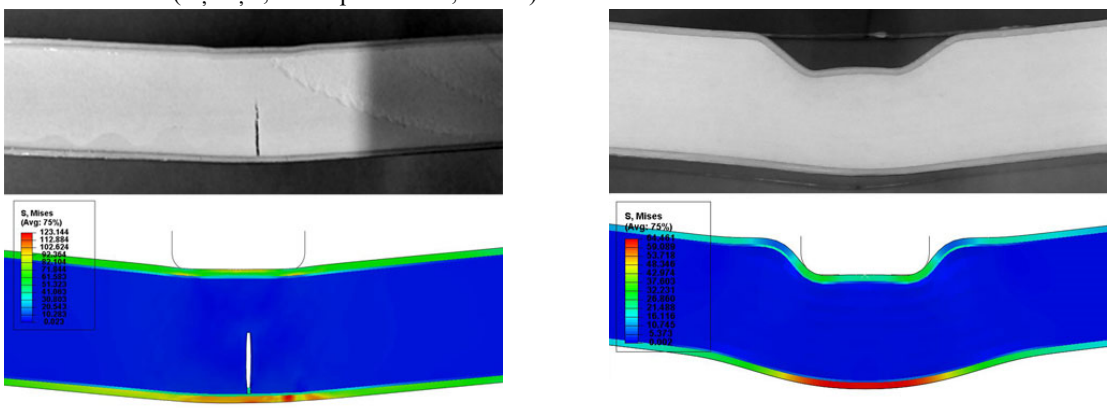

c. Miez compact, densitate 100 kg/m^3

d. Miez compact, densitate 300 kg/m^3

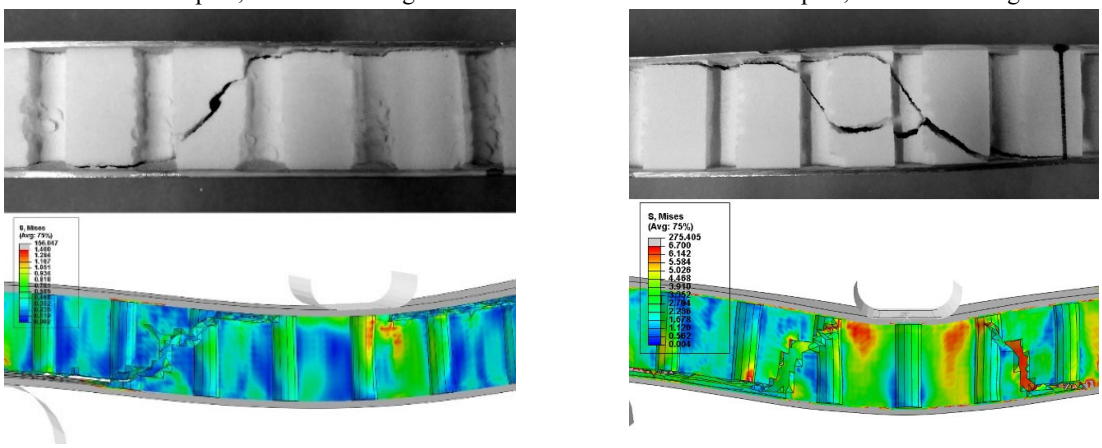

e. Miez perforat, densitate 100 kg/m^3

f. Miez perforat, densitate 300 kg/m^3

Fig. 1.3.13. Simularea numerică a cedării structurilor tip sandwich

Rezultatele au fost publicate în articolul [3].

Activitatea 1.3.4 Comportamentul la impact al polistirenului expandat prin metode experimentale și numerice

Astăzi, polistirenul expandat este utilizat în aproape toate domeniile. Este foarte utilizat în domeniul construcțiilor, pentru izolarea fațadelor clădirilor datorită caracteristicilor termice foarte bune. Polistirenul utilizat pentru izolarea fațadelor este supus la diverse solicitări, cum ar fi solicitări de îndoire, solicitări dinamice și solicitări prin șoc. În continuare sunt prezentate rezultatele obținute la testele de impact dinamic ale polistirenului expandat, dar și rezultatele obținute la analizele dinamice de impact efectuate cu software-ul de analiză ANSYS. Pentru teste dinamice și analize ale probelor s-au folosit spumă de polistiren tip EPS 50, EPS 80, EPS 100 și EPS 120.

Polistirenul Expandat este durabil, puternic și poate fi utilizat ca sisteme de panouri izolate pentru fațade, acoperișuri și pardoseli în clădiri, ca material de flotație în construcția de porturi și pontoane și ca umplutură ușoară în construcția de drumuri și căi ferate [4, 5, 6].

Investigațiile după furtună au arătat că obiectele purtate de vântul și impactul acestora asupra fațadelor reprezintă o cauză majoră de deteriorare a fațadei clădirii, inclusiv a izolației termice cu panouri realizate din EPS. Resturile transportate de vânt pot pătrunde în izolația clădirii, ceea ce duce la deteriorarea mai gravă a clădirii.

Studiul este structurat în două părți principale. Prima parte, prezintă realizarea experimentală a testelor de impact asupra epruvetelor din EPS cu densități diferite. În a doua parte, pe baza unor condiții de încărcare similare, s-a efectuat o analiză numerică explicită (analiză dinamică de impact) pentru a investiga comportamentul la impact al EPS.

Au fost efectuate teste experimentale de impact pe epruvete din EPS disponibile comercial. Materialul utilizat a fost polistiren expandat cu următoarele densități: EPS 50: densitate 11 kg/mc; EPS 80: densitate 15 kg/mc; EPS 100: densitate 20 kg/mc; EPS 120: densitate 25 kg/mc.

Pentru testele experimentale de impact au fost realizate probe din polistiren expandat, având dimensiunile (L x l x h): 200x200x30mm tăiate din materialele EPS enumerate mai sus.

Pentru efectuarea experimentală, a fost realizat un pendul gravitațional (a se vedea figura 1) astfel încât să creeze condiții reale de impact ale panourilor din EPS. Bila metalică cu un diametru de 120 mm și o masă de 9 kg va lovi suprafața probelor de polistiren. Lungimea brațului pendulului poate fi reglabilă pentru a atinge diferite viteze de impact. Pentru experiment, bila a fost considerată la o înălțime de 0,5m și aceasta va produce conform formulelor pendulare gravitaționale o viteză de impact de 3344,2 mm/s. În Fig. 1.3.14 este prezentată și poziția probelor în timpul experimentului. Tipurile de polistiren menționate mai sus au fost afectate cu aceeași viteză de impact și respectiv, aceași orietare de masă.

După efectuarea testului de impact, s-au măsurat urmele lăsate de bilă pe suprafața probelor. Suprafața probei a fost lovită cu bila o singură dată. Fig. 1.3.15 arată valoarea măsurată a urmelor lăsate de bilă pe suprafața probei din EPS 80.

Fig. 1.3.14 Echipamentul de testare

Fig. 1.3.15 Degradarea produsă de impact

Software-ul utilizat pentru analizele dinamice explicite a fost ANSYS 2019R2 Academic. Pentru a efectua simularea dinamică, condițiile de încărcare pentru bilă au constat în viteza inițială (egală cu viteza de impact calculată a pendulului 3344,2 mm / s) și suportul fix pentru partea inferioară a probei din EPS (a se vedea Fig 1.3.16).

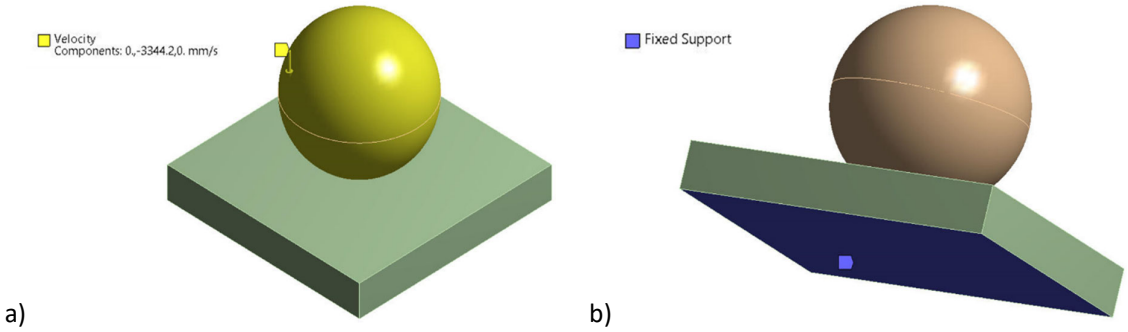

Fig. 1.3.16 Condiții limită

a. viteza inițială a bilei de impact b. fixarea suprafeței inferioare a probei EPS.

După stabilirea condițiilor de încărcare și rezemare a fost realizată rețeaua de discretizare. Pentru zonele de contact (între suprafața bilei și suprafața probei din EPS) a fost realizată o rețea mai fină, valoarea elementului fiind de 1mm (a se vedea Fig. 1.3.17).

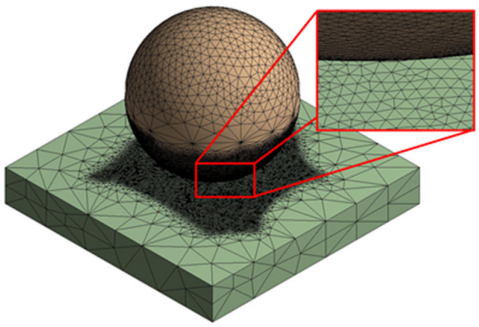

Fig. 1.3.17 Discretizarea modelului

După efectuarea analizei s-au obținut valori ale deformațiilor și energiilor absorbite pentru probele din EPS cu densități diferite. În Fig. 1.3.18 sunt prezentate valorile deformațiilor obținute din analiza dinamică explicită a impactului.

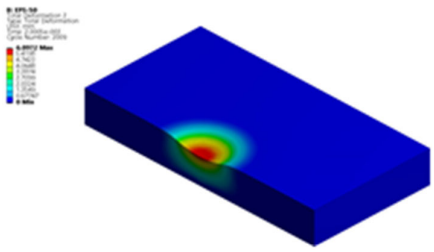

Fig. 1.3.18 Deplasarea numerică pentru EPS50 după impact.

Fig. 1.3.19 prezintă valoarea energiei absorbite a EPS 120, obținută din analiza dinamică explicită de impact.

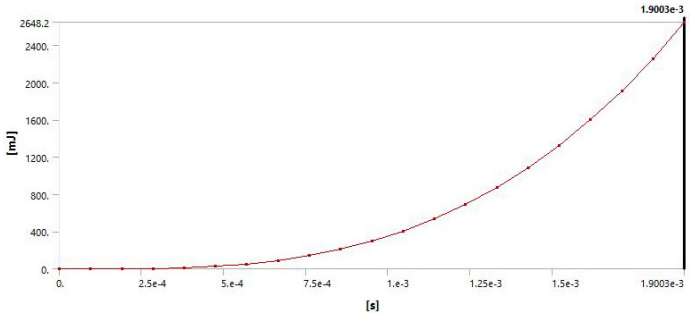

Fig. 1.3.19 Variația energiei interne pentru EPS 120 după impact.

Rezultate

Valorile deformațiilor și energiei interne obținute în urma analizelor numerice de impactului și ale deformațiilor obținute în urma testelor experimentale sunt prezentate în Tabelul.1.

Tabel 1. Deplasarea și energia internă

EPS	Deplasare (experimentală) [mm]	Deplasare (numerica) [mm]	Energia internă [mJ]
50	**5,9933**	**6,0972**	**418,33**
80	**5,7790**	**5,8655**	**828,32**
100	**5,7711**	**5,7645**	**2159,1**
120	**5,7560**	**5,7552**	**2648,3**

Pentru o mai bună vizualizare a rezultatelor din Tabelul 1, a fost realizată o comparație grafică între deplasările numerice și experimentale, prezentate în Fig. 1.3.20.

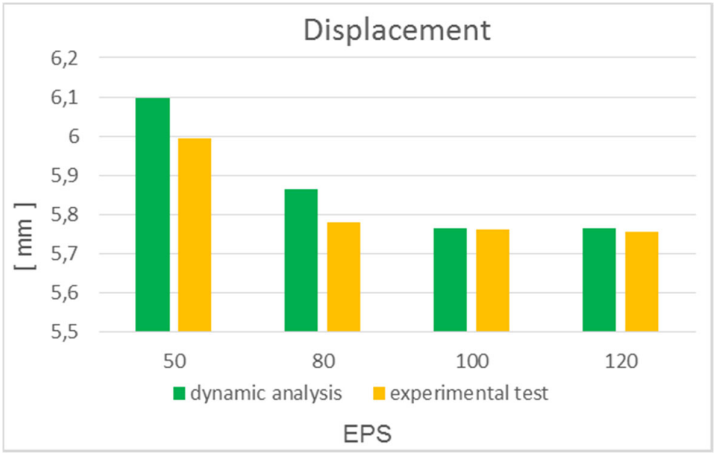

Fig. 1.3.20 Comparație între rezultatele numerice și cele exoperimentale

Deoarece materialul are o revenire elastică, la valoarea măsurată a urmei lăsate de bilă se va adăuga deformarea elastică calculată pe baza curbei tensiune - deformare a materialului obținută după testul experimental de compresie.

Astfel, de exemplu pentru EPS 80, deformarea totală în timpul impactului va fi:

$$4{,}53 \text{ mm} + 1{,}249 \text{ mm} = 5{,}779 \text{ mm}$$

În această expresie, 4,53mm reprezintă valoarea adâncimii lăsate de bilă după impact (deformare permanentă), iar 1,249mm este deformarea elastică a EPS 80, rezultând o deformație totală de 5,779 mm. Această valoare a fost considerată valoarea experimentală a deformării în timpul impactului și comparată cu rezultatele simulării numerice.

S - a analizat comportamentul la impact al polistirenului, fenomen întâlnit adesea în construcții atunci când fațada unei clădiri este lovită cu diverse obiecte. Pentru a înțelege comportamentul mecanic de impact au fost efectuate atât cercetări numerice cât și experimentale. Testele experimentale de impact efectuate pe probele EPS de diferite densități au fost comparate cu modelarea numerică utilizând analize dinamice explicite în aceleași condiții de încărcare. Modelul materialului utilizat în simulare a fost validat și experimental prin test de compresie la diferite viteze de testare.

Concluzii

- Studiile experimentale realizate prin termografie au arătat că aceste metode pot fi folosite cu succes pentru identificarea cedărilor materialelor celulare folosite ca miez în structurile tip sandwich.
- Studiile statistice au indicat că tenacitatea la rupere a spumelor PUR poate fi considerată o caracteristică de material nedepinzând de tipul epruvetelor și al încercărilor. Influența principală asupra tenacității la rupere o are densitatea, apoi un efect mai mic are direcția de solicitare. Legătura dintre tenacitatea la rupere și densitate este cel mai bine reprezentată de un model micromecanic exponențial.
- Metodologia de simulare a cedării structurilor tip sandwich a fost validată experimental de testele la încovoiere în trei puncte.
- A fost analizat comportamentul la impact al polistirenului, fenomen des întâlnit in cadrul construcțiilor când fațada este lovita cu diverse obiecte. Au fost realizate atât modelari numerice utilizând analiza explicita si curbele de material determinate experimental prin compresiune precum si o validare experimentala cu ajutorul unui dispozitiv de impactare de tip pendul. Rezultatele obținute prin cele doua metode sunt în bună concordanță, fapt care certifică valabilitatea lor.

Bibliografie

1. L. Marsavina, E. Linul, Fracture toughness of rigid polymeric foams: A review, *FATIGUE AND FRACTURE OF ENGINEERING MATERIALS AND STRUCTURES*, 2020, 43, 2483–2514. (Jurnal indexat ISI – Q1)
2. A. Pugna, R. Negrea, E. Linul, L. Marsavina, Is fracture toughness of PUR foams a material property? A statistical approach, *MATERIALS*, 2020, 13, 4868 (Jurnal indexat ISI – Q2).
3. D.A. Șerban, R. Negru, H. Filipescu, L. Marsavina, Investigations on the influence of the triaxial state of stress on the failure of polyurethane rigid foams, *CONTINUUM MECHANICS AND THERMODYNAMICS*, 2020, https://doi.org/10.1007/s00161-020-00924-x (Jurnal indexat ISI – Q2).
4. https://omnexus.specialchem.com/selection-guide/expanded-polystyrene-eps-foam-insulation.
5. U. Caliskan, M K. Apalak, Bending impact behaviour of sandwich beams with expanded polystyrene foam core: Analysis, Journal of Sandwich Structures and Materials 2019, Vo l. 21(1) 230–259.
6. U. Caliskan, M. K. Apalak, FEM analyses of low velocity impact behaviour of sandwich panels with eps foam core, Journal of Thermal Engineering, Vol. 3, No. 6, Special Issue 6, pp. 1544-1552, December, 2017.
7. C. Vilau, M.C. Dudescu, Impact behaviour of expanded polystirene by experimental and numerical methods, *ACTA TECHNICA NAPOCENSIS*, 2020, în recenzie

Received: 24 April 2020 | Revised: 22 July 2020 | Accepted: 1 August 2020

DOI: 10.1111/ffe.13327

INVITED CONTRIBUTION

FFEMS Fatigue & Fracture of Engineering Materials & Structures WILEY

Fracture toughness of rigid polymeric foams: A review

Liviu Marşavina | **Emanoil Linul**

Department of Mechanics and Strength of Materials, University Politehnica Timisoara, Blvd. Mihai Viteazu, No.1, Timisoara, 300 222, Romania

Correspondence
Liviu Marşavina, Department of Mechanics and Strength of Materials, University Politehnica Timisoara, Blvd. Mihai Viteazu, No.1, Timisoara 300 222, Romania.
Email: liviu.marsavina@upt.ro

Funding information
European Commission, Grant/Award Number: Horizon 2020, No. 857124; Romanian Ministry of Research and Innovation, Grant/Award Numbers: 10PFE/16.10.2018, PERFORM-TECH-UPT, PN-III-P1-1.2-PCCDI-2017-0391

Abstract

Polymeric foams have good capacity of absorbing energy in compression but are brittle in tension. Linear elastic fracture mechanics is successfully applied to assess the integrity of polymeric foam-based composite structures. The fracture toughness represents an important parameter. The different approaches to estimate the fracture toughness of polymeric foams are reviewed: analytical and numerical micromechanical models and experimental investigations. Focus is given on the parameters influencing the fracture toughness of polymeric foams like specimen type, solid material, density, loading speed, size effect and temperature. Data on mixed-mode loading and dynamic fracture toughness are also presented. The last part of the paper presents some results to increase the fracture toughness by reinforcing of polymeric foams.

KEYWORDS

experimental data, fracture toughness, micromechanical models, mixed-mode fracture, numerical analysis, polymeric foams

1 | INTRODUCTION

The polymeric foams belong to the class of manufactured cellular materials (Figure 1). The properties of cellular materials depend on the properties of the solid from which they are produced; the cell shapes, dimensions and topology and the relative density (density of the foam divided to density of solid material) (Figure 2).[1]

Polymeric foams are made of interconnected networks of solid struts and cell walls incorporating voids with entrapped gas, resulting a cellular structure with open (the solid material is found in the edges of the cells), closed (the solid material is found in both the edges and faces of the cells) or mixed (partially open, partially closed) cells. The main characteristics of foams are lightweight, high porosity, good energy absorption capacity and floatability.[2,3] The use of polymeric foams increases considerably in the last three decades. The main applications are in construction and civil engineering for thermal isolation, in packing, in aeronautics and automotive industries, in buoyancy due to their floatability and in sport for shoes, helmets and other protection systems.

Most of the plastic foam materials crush progressively in compression until they reach full densification,[2] whereas in tension fail by propagating of a single crack.[4] Polymeric foams have an elastic–plastic behaviour in tension, whereas in the presence of notches and cracks, they behave linear-elastic up to fracture and highlight a brittle failure.[4,5] Therefore, they can be treated using linear elastic fracture mechanics (LEFM) criteria. Consequently, the fracture toughness of such porous materials became an important characteristic, because cracks weaken the foam structures capacity of carrying load.

The objective of this paper is to review the analytical, numerical and experimental studies carried on to determine the fracture toughness of rigid polymeric foams.

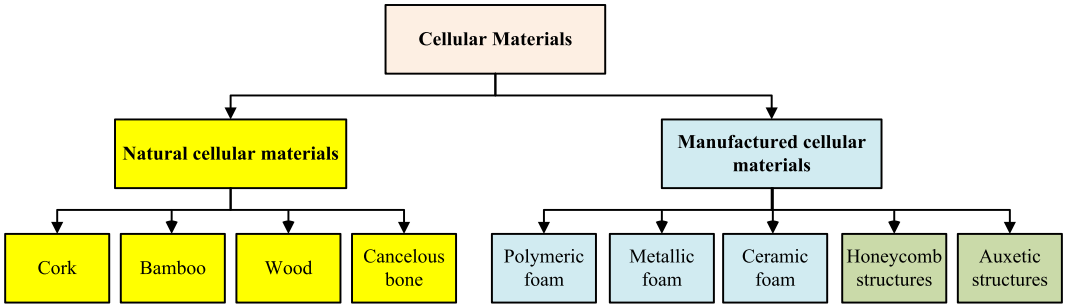

FIGURE 1 Classes of cellular materials, adapted from Ashby[1] and Gibson and Ashby[2] [Colour figure can be viewed at wileyonlinelibrary.com]

Particular attention will be paid to the effects of density, anisotropy, loading speed, specimen type and temperature on fracture toughness. The mixed-mode fracture, the size effect on polymeric foam and dynamic loading will be also presented. Finally, some new methods of increasing the fracture toughness by reinforcing the foams are discussed.

2 | MICROMECHANICAL MODELS FOR FRACTURE TOUGHNESS OF FOAMS PREDICTION

Micromechanical models are often used to predict the properties of cellular materials,[2] such as foams Pr_f, based on the properties of solid material Pr_s and the relative density ρ_f/ρ_s:

$$\mathrm{Pr}_f = C\mathrm{Pr}_s\left(\frac{\rho_f}{\rho_s}\right)^n \tag{1}$$

where C and n are fitting parameters.

Micromechanical analysis can estimate the full multiaxial properties and response of cellular materials, which are usually anisotropic.[6–12] Such properties are often difficult to measure experimentally, but they are very important in design of the lightweight composite structures containing foam cores. Micromechanical analysis also allows to describe the structural damage and failure of cellular materials.[13–21] Gibson and Ashby,[2] Mills[3] and Fleck et al.[22] presented extensive studies of micromechanical models for cellular materials. In this chapter, only the main models regarding the fracture toughness will be reviewed.

The micromechanical models used to predict the fracture toughness K_{IC} of the foams are based on the fracture strength of the cell wall materials σ_{fs}, the relative density ρ_f/ρ_s and the cell dimension l.[23] Gibson and Ashby[2] assumed that the crack tip is located at half-edge and advances discrete with one cell width (Figure 3). Applying a tensile load to cellular structure, the cell walls deform elastically in mode I, and load is transmitted through the foam as a set of forces and moments acting on the cell edges.

Considering that the crack extends when the tensile strength on the strut reaches the fracture strength of the solid material, Maiti et al.[24] proposed the following micromechanical models:

- for open cells

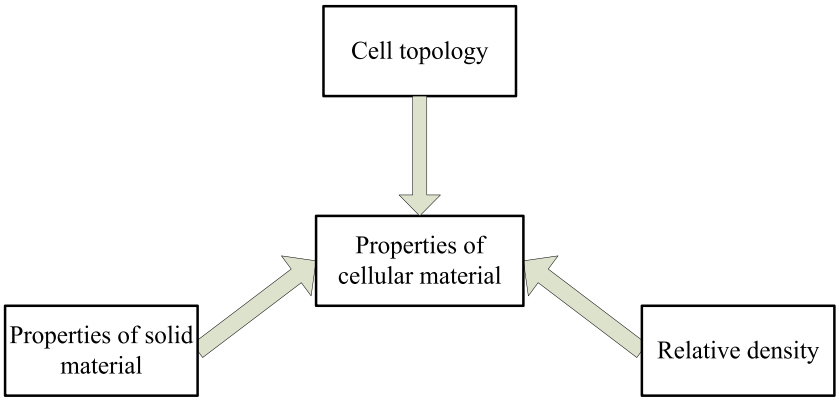

FIGURE 2 Factors influencing the cellular material properties, adapted from Ashby[1] [Colour figure can be viewed at wileyonlinelibrary.com]

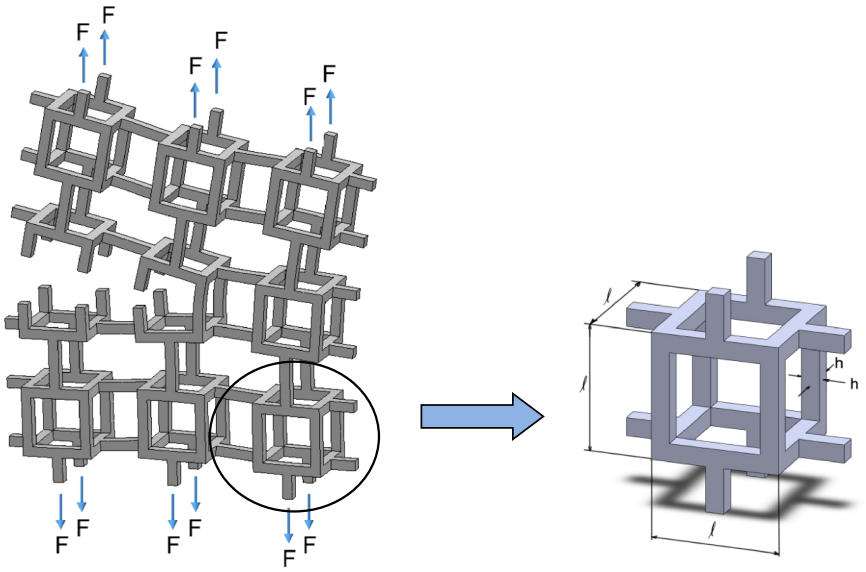

(A) crack propagation trough brittle open-cell foam[2] (B) unit cell

FIGURE 3 Cracked cellular structure, adapted from Gibson and Ashby[2] [Colour figure can be viewed at wileyonlinelibrary.com]

$$K_{IC} = C_1 \sigma_{fs} \sqrt{\pi l} \left(\frac{\rho_f}{\rho_s}\right)^{1.5} \tag{2a}$$

- for closed cells

$$K_{IC} = C_2 \sigma_{fs} \sqrt{\pi l} \left(\frac{\rho_f}{\rho_s}\right)^{2} \tag{2b}$$

where C_1 and C_2 are proportionality constants. For determining the constant C_1 from Equation 2a, a series of experimental data obtained for different foam materials such as polyurethane,[25,26] PMMA[24] and ceramic[27] were interpolated, resulting $C_1 = 0.65$.

Huang and Gibson[28,29] investigated the factors affecting the fracture toughness of brittle honeycombs and foams. Experimental results on reticulated carbon foams show that Equations 2a and 2b are valid only for crack length higher than 10 times the cell length.[28]

Green[30] proposed a similar correlation considering elastic deformation in shell theory of hollow sphere model for foam cells:

$$\frac{K_{IC}}{\sigma_{fs}\sqrt{\pi l}} = 0.28 \left(\frac{\rho_f}{\rho_s}\right)^{1.3} \tag{3}$$

Choi and Sankar[31] using LEFM relate the stress intensity factors to the stress filed in the crack tip ligament of the foam. Apart from considering only the tensile of struts, they also take into account the effect of bending moment (Figure 4).

Assuming that fracture of strut occurs when the maximum stress, for combined state of load bending and tensile, equals the ultimate tensile strength of the ligament material σ_{fs}, Choi and Sankar[31] relate the fracture toughness K_{IC} to the tensile strength of solid material, cell dimensions (l and h) and crack length (a) in the form of Equation 4:

$$K_{IC} = \sigma_{fs} \frac{h^2}{l} \sqrt{\frac{\pi}{2a}} \frac{1}{\left(1 + 2\frac{a}{h}\right)} \tag{4}$$

Similarly, the mode II fracture toughness was obtained considering the shear stress ahead of the crack tip[31] as follows:

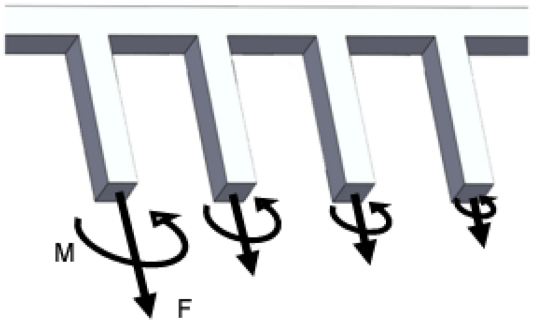

FIGURE 4 Forces and moments at the crack in foam, adapted from Choi and Sankar[31] [Colour figure can be viewed at wileyonlinelibrary.com]

$$K_{IIC} = \sigma_{fs} \frac{h^3}{3l^2} \sqrt{\frac{\pi}{2a}} \tag{5}$$

Choi and Lakes[32] proposed another model, which take into account the crack blunting and the nonsingular stress field ahead of the crack tip. The fracture toughness was obtained considering that the maximum stress in bending reaches the tensile strength of solid results:

$$K_{IC} = 0.20 \sigma_{fs} \sqrt{\pi l} \left(\frac{h}{l}\right)^2. \tag{6}$$

For regular tetrakaidecahedron cell packing, the relation between relative density and cell dimensions is

$$\left(\frac{\rho_f}{\rho_s}\right) = 1.06 \left(\frac{h}{l}\right)^2 \tag{7}$$

and the resulted fracture toughness is

$$\frac{K_{IC}}{\sigma_{fs}\sqrt{\pi l}} = 0.19 \left(\frac{\rho_f}{\rho_s}\right). \tag{8}$$

Considering a rectangular void shape of the strut cross section with the thickness h and void h_i (Figure 5), the fracture toughness could be expressed in the form[2]:

$$K_{IC} = C \sigma_{fs} \sqrt{\pi l} \left(\frac{\rho_f}{\rho_s}\right)^{3/2} \frac{1 + \left(\frac{h_i}{h}\right)^2}{\sqrt{1 - \left(\frac{h_i}{h}\right)^2}}. \tag{9}$$

Fan and Fang[33] presented a complex analysis of hollow structures. They concluded that the hollow-strut foams have superior mechanical properties compared with solid-strut foams for the same relative density. The hollow-strut foams are more damage tolerant than the solid-strut foam, because of their enlarged bending stiffness. The enhancements of stiffness, buckling strength, plastic collapse strength, brittle failure strength and fracture toughness were substantially increased according to their analysis. Three types of hollow struts were investigated with square, equilateral triangle and circular cross sections. Regarding the fracture toughness of hollow-strut foams, this is related to the ratio $f = h_i/h$, between length of inner side h_i and outer length h. The enhancement is 4.15 when the value of f is 0.9.

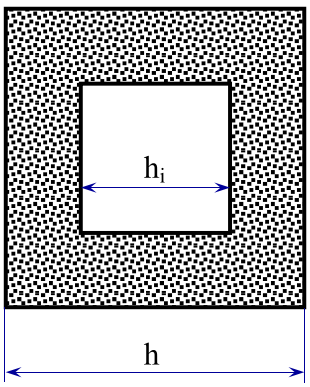

FIGURE 5 Strut with a rectangular void shape, adapted from Gibson and Ashby[2] [Colour figure can be viewed at wileyonlinelibrary.com]

Chen et al.[34] present a micromechanical analysis of cellular materials based on a strain gradient model. A generalized continuum model was applied considering the equivalence of strain energy at macroscale and microscale. The asymptotic field near crack and the full field solutions were obtained for different cell lattices: hexagonal, triangular and square. The fracture toughness was determined using the maximum tensile stress fracture criterion of cell wall. The fracture toughness is proportional with the cell thickness h and inversely proportional with square of cell size $l^{0.5}$ in the form:

$$K_{iC} = C_i \frac{\sigma_{fs} h}{\sqrt{l}} \tag{10}$$

where i corresponds to mode I and mode II of loading.

The values of C_i (i = I and II) for the considered cell lattices are shown in Table 1.

Lipperman et al.[35] considered a lattice model consisting of rigidly connected Euler beams, which can fail when the skin stress reaches a critical value. The fracture toughness for mode I and mode II was estimated, and the influence of the relative density was highlighted. The crack was modelled considering several broken beams. Four different cell topologies were defined as follows: kagome, triangular, square and hexagonal honeycombs (Figure 6), and the solution was determined analytically with discrete Fourier transform reducing the initial problem for unbounded domain to the analysis of a finite repetitive module in the transform space. For investigating the anisotropy of lattices, the results of the normalized fracture toughness $K_{IC}/\sigma_{fs}\sqrt{l}$ are shown in the form

TABLE 1 Values of C_I and C_{II} for the different cell lattices[34]

Cell shape	C_I	C_{II}
Hexagonal	1.8	0.77
Triangular	4.6	1.5
Square	1.4	0.068

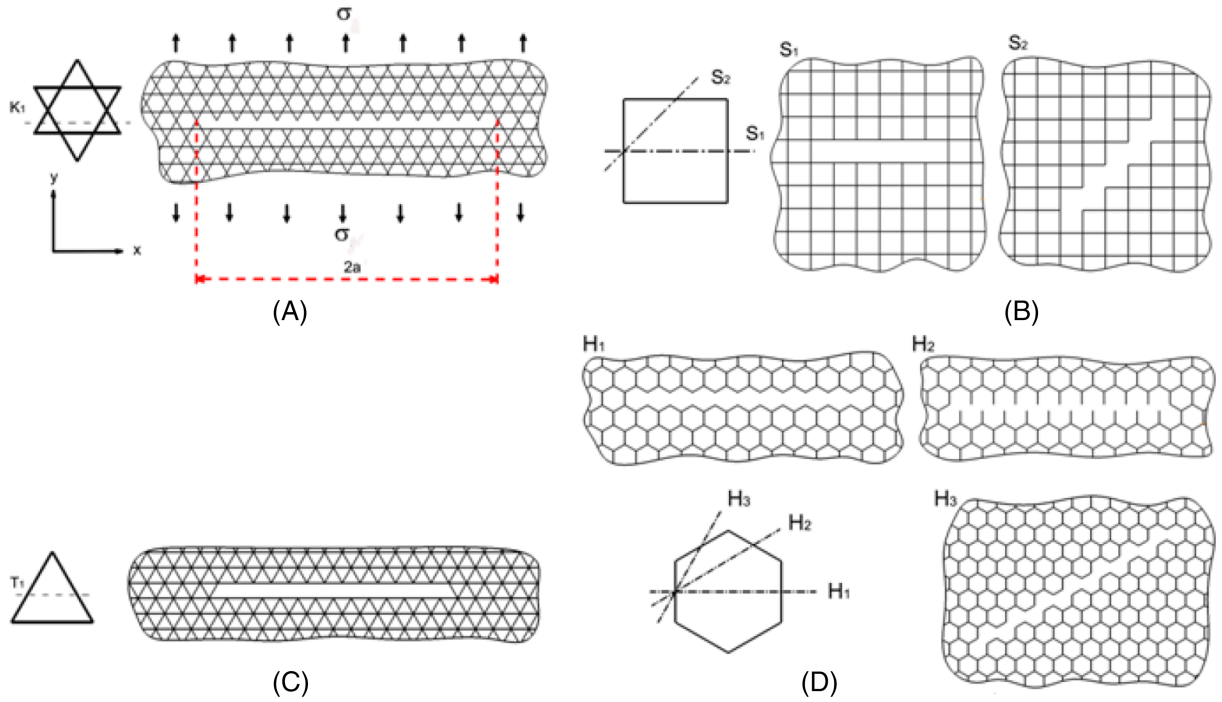

FIGURE 6 Lattice cracked models (A, kagome; B, square; C, triangular and D, hexagonal), adapted from Lipperman et al.[35] [Colour figure can be viewed at wileyonlinelibrary.com]

of polar diagrams, and quasi-isotropic fracture behaviour was observed for all investigated structures.

The variation of fracture toughness with relative density is investigated for different types of cell lattice. This is close to linear for kagome and triangular lattices and is in agreement with other published data.[2,34] The mode II fracture toughness is smaller than the mode I for almost all investigated cases.[35]

All the above micromechanical models relate the foam fracture toughness to the tensile strength of the solid material and microstructure parameters: cell length and relative density. The methodology assumes that the load is transmitted through the foam as a set of discrete forces and moments acting on cell struts. Different integration limits were used in order to determine the forces and moments. Singular[2,31] and nonsingular stress fields[32] in front of crack were considered. The fracture toughness was obtained by considering that the crack extents when the stress in the first strut in front of the crack reaches the tensile strength of the solid. When micromechanical models are used, the size effect regarding the variation of the tensile strength of the solid material σ_{fs} with strut size should be considered.[30] Huang and Gibson[29] proposed a statistical analysis based on Weibull distribution in order to show the effect of cell size on fracture toughness.

Choi and Lakes[32] relate the fracture toughness of foam K_{IC} to the fracture toughness of solid material K_{ICs}:

$$K_{ICs} = \sigma_{fs}\sqrt{\pi a}, \tag{11}$$

with a small defect in the bulk material, starting from a generalized expression of Equations 2a and 2b:

$$\frac{K_{IC}}{\sigma_{fs}\sqrt{\pi l}} = C\left(\frac{\rho_f}{\rho_s}\right)^{1+n} \tag{12}$$

with $n \geq 0$.

Substituting σ_{fS} between Equations 11 and 12, we obtain

$$\frac{K_{IC}}{\frac{K_{ICs}}{\sqrt{\pi a}}\sqrt{\pi l}} = C\left(\frac{\rho_f}{\rho_s}\right)^{1+n} \quad \text{yielding to}$$
$$\therefore \frac{K_{IC}}{\rho_f} = \frac{K_{ICs}}{\rho_s}\sqrt{\frac{l}{a}}C\left(\frac{\rho_f}{\rho_s}\right)^{n}. \tag{13}$$

More recently, Jelitto and Schneider[36,37] proposed some interesting geometric micromechanical models relating the fracture toughness K_{IC} of foams to the fracture mechanics of solid material K_{ICs}, considering three models:

- closed cell foams

$$\frac{K_{IC}}{K_{ICs}} = \left(1-P^{\frac{2}{3}}\right)^{\frac{1}{2}} \left(\frac{1-d}{-d^2+2d} + \frac{1}{-d+2+(1-d)^2 d^{-\frac{1}{2}}}\right)^{-\frac{1}{2}} \tag{14}$$

where $d = h/l$ represents a geometric parameter and $P = (1 - d)^3$ represents the porosity.

- open cell foams

$$\frac{K_{IC}}{K_{ICs}} = d^2 \left(\frac{-2d+3}{2d^2-4d+3}\right)^{\frac{1}{2}} \tag{15}$$

- open cell with discontinuities

$$\frac{K_{IC}}{K_{ICs}} = d\frac{\left(-2d^3+3d^2\right)^{m+\frac{1}{2}}}{\left(2d^2-4d+3\right)^{\frac{1}{2}}} \tag{16}$$

with m representing the amount of disconnected ligaments (Figure 7).

For the open cell and open cell with discontinuities structures, the relation between porosity and geometric parameter d is given by

$$d = \cos\left(\frac{2\pi - \cos^{-1}(2P-1)}{3}\right) + \frac{1}{2}$$

These micromechanical models were compared with different types of foams (polymeric and ceramic), and good correlation was observed. The model assumes that the toughness is proportional to the relative amount of substantial crack surface and that fracture occurs along the path with the minimum area of substantial crack face. It can be applied for any porosity between 0 and 1. An advantage of the models is that they are not dependent on the cell size.

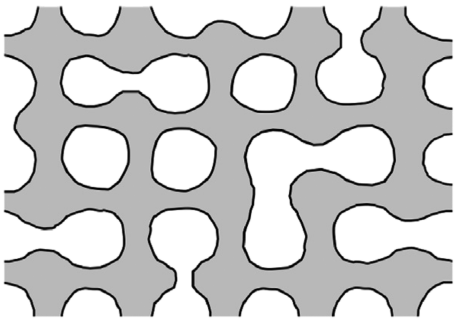

FIGURE 7 Typical cross section through the ligaments in a cell structure with disconnections, adapted from Jelitto and Schneider[36]

Fewer solutions are presented in the literature for mode III fracture toughness. Rivkin[38] proposed an analytical micromechanical model for a mode III crack in a lattice model using discrete Fourier transform and the solving the Wiener–Hopf equation. The expression of mode III fracture toughness is similar with Equations 2a and 2b:

$$K_{IIIC} = C\sigma_{fs}\sqrt{l}\left(\frac{\rho_f}{\rho_s}\right)^{1.5} \tag{17}$$

where C depends on the struts cross section and on the ratio between strut thickness h and cell size l.

A micromechanical model to investigate the influence of the cell size was presented by Huang and Lin[39] for mode II fracture toughness, considering two foams of the same density but with different cell size, in the form:

$$\frac{K_{IIC,1}}{K_{IIC,2}} = \left(\frac{l_1}{l_2}\right)^{\frac{1}{2}-\frac{2}{m}} \tag{18}$$

where $K_{IIC,1}$ and $K_{IIC,2}$ represent the fracture toughness of same density foam, but for different cell size l_1 and l_2. Fracture toughness of brittle foams increases with increasing cell size if $m > 6$, when $m < 6$ K_{IIC} decreases with increasing cell size, whereas if $m = 6$, there is no cell size effect.

Huang and Lin[39] also proposed a fracture criterion of brittle foam for mixed-mode loading, in the form of linear combination:

$$\frac{K_I}{K_{IC}} + \frac{K_{II}}{K_{IIC}} = 1. \tag{19}$$

At the end of this chapter, we can conclude that wide ranges of micromechanical models are available in the literature to predict the fracture toughness of polymeric foams considering different cell shapes (square, triangular, hexagonal and kagome). However, the use of these should be made with precaution without experimental validation.

3 | NUMERICAL PREDICTION OF FRACTURE TOUGHNESS FOR CELLULAR MATERIALS

Srivastava and Srivastava[40] presented a review of the polymeric foam modelling considering open and closed

cells, respectively regular and irregular cell topology. The available foam material models for finite element analysis (FEA) are reviewed, and the features of these models (like strain rate, damage, effect of temperature, failure, damage and anisotropy) are summarized. The material models have been validated through a series of tests such as tensile, compression, shear, hydrostatic stress, impact, drop test and indentation.

Finite element (FE) modelling methods are used to describe the mechanical behaviour and to predict the properties of cellular structures.[18,41–44]

In recent years, FE is increasingly applied to numerically investigate the fracture and damage of cellular materials.[31,45–47] FEA is particularly implemented for closed cell foams where the analytical formulations are more complex. Quintana-Alonso et al.[48] investigated the fracture toughness of cordierite square lattice.

Also, an FE-based method developed by Choi and Sankar[31] has been used by Wang[49] to study the fracture toughness of two types of foams: foams with rectangular prism unit cells, including homogeneous foams and functionally graded foams, and tetrakaidecahedral foams. He obtained the plain-strain fracture toughness of the foam by relating the fracture toughness to the tensile strength of the cell struts. In addition, he studied the effects of various geometric parameters that describe the cell. Two crack propagation criteria, one at the microscale and one at the macroscale, were used. The fracture toughness of brittle foam is calculated based on the stress intensity factor and the corresponding maximum tensile stress in the struts ahead of the crack. Fleck and Qiu[50] performed an FEA on hexagonal honeycomb, regular triangular honeycomb and Kagome lattice models using Euler Bernoulli beam elements with cubic interpolation functions, considering each beam with thickness t and length l. They present the prediction of fracture toughness related to the solid material in the form:

$$\frac{K_{IC}}{\sigma_{fs}\sqrt{\pi l}} = D\left(\frac{\rho_f}{\rho_s}\right)^d \tag{20}$$

where D is 0.212 (Kagome lattice), 0.5 (regular triangular honeycomb) and 0.8 (hexagonal honeycomb), whereas exponent d equals 2 for hexagonal honeycomb, 1 for regular triangular honeycomb and 0.5 for Kagome lattice loaded in mode I.

Christodoulou and Tan[51] present a study regarding the competing effects of cell regularity and relative density upon the fracture toughness under different loading modes of Voronoi honeycombs. To investigate the effects of the random cell topology, sufficiently large models of Voronoi tessellations were generated. The cell regularity was defined as nondimensional parameter Λ in the interval (0, 1] corresponding to complete irregular structure to a regular hexagonal honeycomb. A square FE mesh for each tessellation was created in ABAQUS/Standard software. Then periodic boundary conditions (BCs) were imposed on the lattice boundaries. The average fracture toughness of the lattices was fitted to the scaling law similarly with Equation 9. For mixed-mode loadings, the fracture loci were presented as K_{II}/K_{IC} versus K_I/K_{IC} (Figure 8) for different cell-regularity parameter Λ. The conclusion is that for pure mode I, fracture toughness of a lattice decreases as it becomes more irregular with an overall reduction of up to 25% for completely random lattices. The mode I fracture toughness of the lattices is more sensitive to cell topological variations than mode II.

Most of the micromechanical models considered the cell walls in a form of beams.[2,24,35,50] Linul and Marsavina[52] proposed a 2D solid FE model, based on rectangular cell geometry, similar with the cell topology of a 200-kg/m^3 PUR foam, for estimating the mode I and mode II fracture toughness. In order to obtain the fracture toughness, the model was loaded progressively, with a normal σ stress for mode I (Figure 9A), respectively with tangential stress τ for mode II (Figure 9D), up to the maximum normal stress in the first uncracked strut (positioned in front of the crack), reaches the fracture strength of solid material σ_{fs} (Figure 9B,E). The fracture toughness of cellular material was determined using Murakami[53] solution for crack (length 2a) in a plate (dimensions 2 W × 2H):

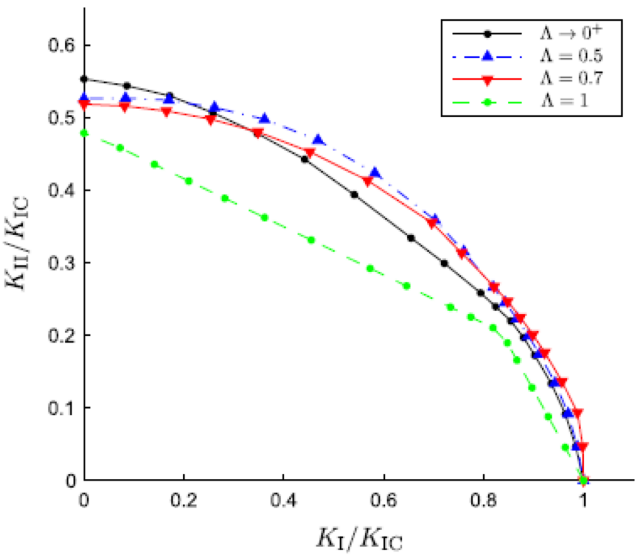

FIGURE 8 Fracture loci for regular and irregular Voronoi lattices, adapted from Christodoulou and Tan[51] [Colour figure can be viewed at wileyonlinelibrary.com]

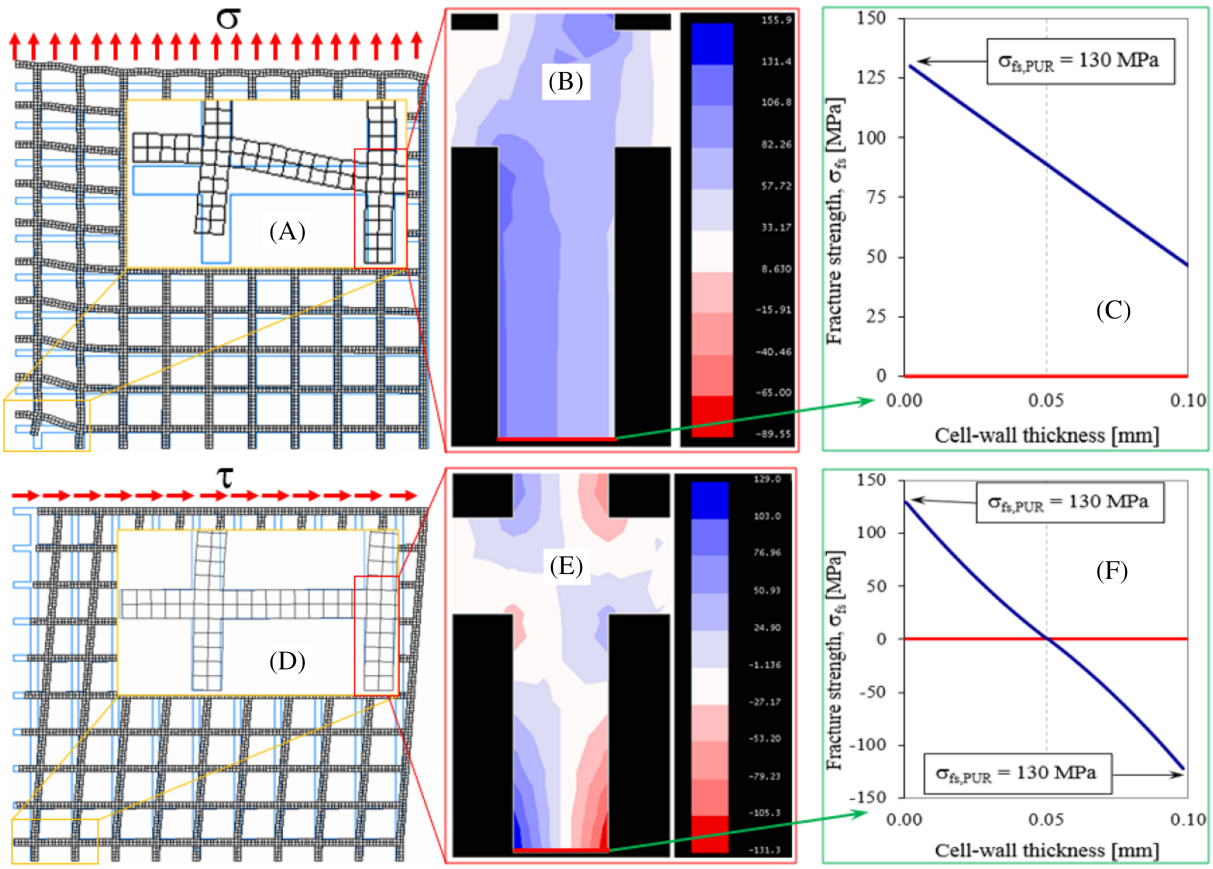

FIGURE 9 The 2D solid model from Linul and Marsavina[52] [Colour figure can be viewed at wileyonlinelibrary.com]

$$K_I = \sigma\sqrt{\pi a}\, F_I(a/W) = K_{IC}$$
$$K_{II} = \tau\sqrt{\pi a}\, F_{II}(a/W) = K_{IIC} \quad (21)$$

The mechanical characteristics of the solid polyurethane material were density, ρ_f = 1170 MPa; fracture strength, σ_{fs} = 130 MPa; Young's modulus, E = 1600 MPa and Poisson's ratio, ν = 0.4. The simulation was performed in Franc2D software, considering constant cell length, l = 0.52–0.60 mm, and variable strut thickness h (0.1, 0.05 and 0.02 mm), respectively constant strut thickness, h = 0.05 mm, and variable cell length l (0.55, 0.75 and 0.95 mm).

A convergence study was performed considering models from 4 × 4 cells to 10 × 10 cells for the same crack length. The results show small differences for mode I fracture toughness between 5 × 5 cells model and 10 × 10 cell model (Figure 10A). The effect of crack length was also investigated considering six different crack lengths: 1.4, 2.35, 3.3, 4.25, 5.2 and 6.15 mm (Figure 10B).

No influence of crack length on mode I (Figure 10) fracture toughness was observed. Figure 11 presents the values of fracture toughness for a PUR foam with 0.39 relative density and different cell numbers (36, 64, 100, 144, 196, 256 and 324) and crack lengths (0.85, 1.25, 2.05 and 2.65 mm) loaded in mode II. The mean value of K_{IIC} = 0.12 MPa m$^{0.5}$ with a scatter of ±0.02 MPa m$^{0.5}$. The relative differences in fracture toughness were small enough to conclude that the predicted fracture toughness could be considered independent on crack length (Figures 10 and 11).

The advantage of this model is that fully describe the stress field in the solid struts. The stress distribution in the first uncracked strut shows a complex stress (bending and tension) for mode I loading (Figure 9C), whereas for mode II loading (Figure 9F), a pure bending occurs. The comparison with other micromechanical models and experimental data of fracture toughness validates the solid 2D micromechanical model.

Based on real microstructures of the PUR foams, Linul et al.[54] extended the previous study (square cells) considering other types of PUR foams cell topologies, such as hexagonal and circular cells (Figure 12).

Different relative densities were considered for the three investigated cell topologies. The results for mode I fracture toughness are shown in Figure 13. It could be observed a linear correlation between K_{IC} and relative density, and the fracture toughness for hexagonal cells is the highest, whereas minimum values were obtained for square cells.

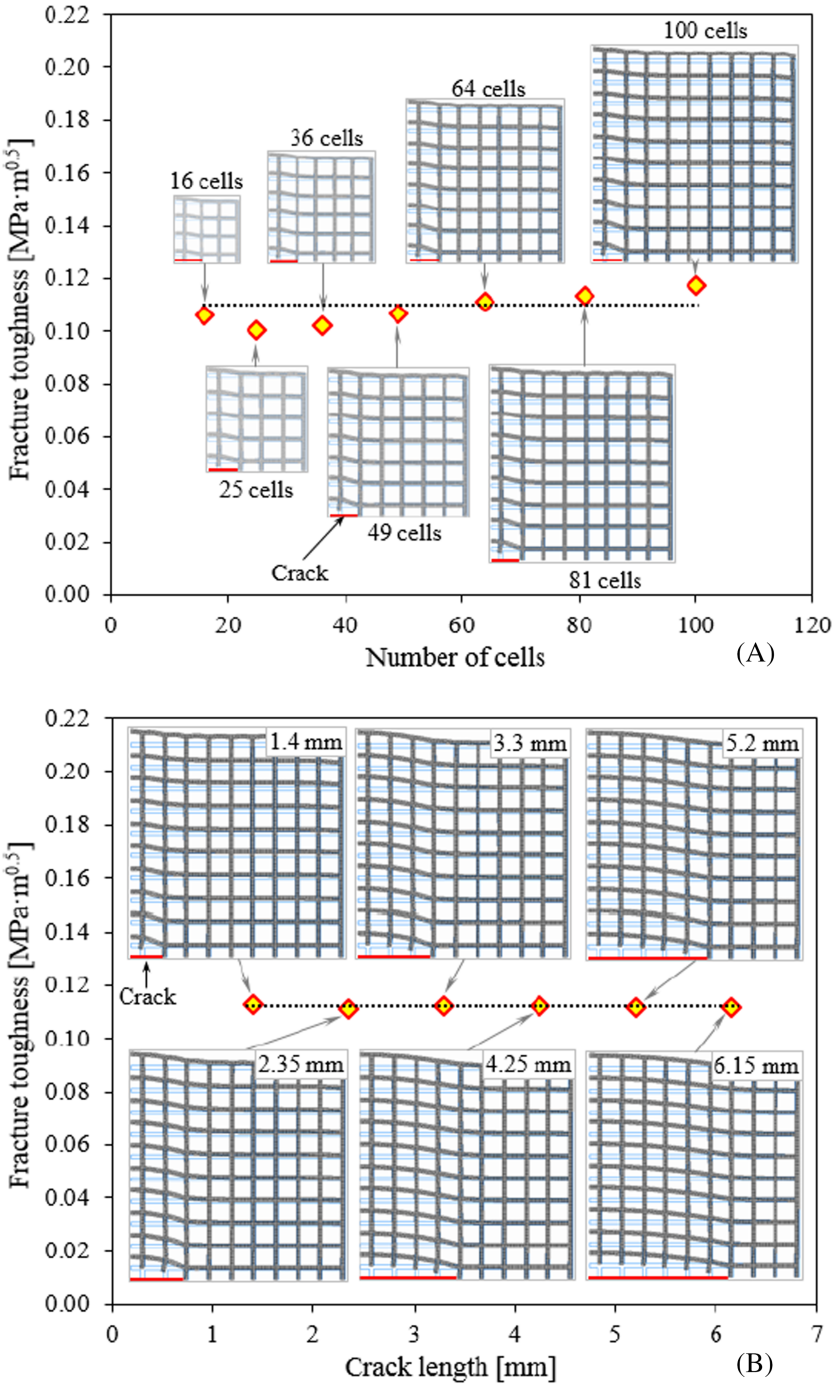

FIGURE 10 Effect of the number of cells (A) and crack length (B) on K_{IC} values [Colour figure can be viewed at wileyonlinelibrary.com]

Choi and Sankar[31] (Figure 14) presented a comparison between a solid 3D model and a beam model to predict fracture toughness of carbon foam. They obtained good agreement between the predicted values and experimental values.

Thiyagasundaram et al.[55] developed a 3D FE micromechanical model based on tetrakaidecahedral unit cell. The foam was modelled as homogeneous orthotropic material in the outer region, whereas in the crack dominant zone, a beam structure having a tetrakaidecahedral unit cell and a triangular cross section of the struts (Figure 15). The FE was obtained by repeating unit cell with strut length $l = 1$ mm and cross-section dimension $h = 0.06$ mm resulting a relative density $\rho_f/\rho_s = 0.00165$. The solid material from the cell struts has density of $\rho_s = 1650$ kg/m^3, Young's modulus, $E_s = 23.42$ GPa; Poisson's ratio, $v_s = 0.33$ and tensile strength, $\sigma_{fs} = 685.5$ MPa. The crack was introduced by removing the cells along the crack length. The imposed BCs were the displacements near the crack tip for homogeneous

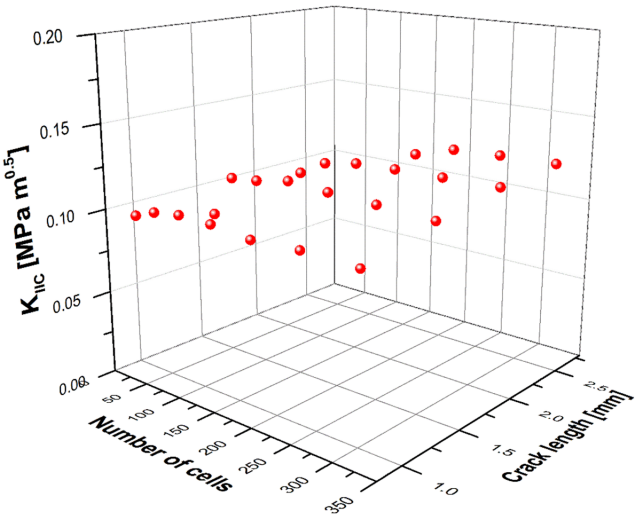

FIGURE 11 Effect of the number of cells and crack length on K_{IIC} values [Colour figure can be viewed at wileyonlinelibrary.com]

orthotropic material. The predicted fracture toughness results converge as the size of micromechanical model increased above 700 cells.

Wang,[49] in order to determine the plane strain fracture toughness, used a tetrakaidecahedral unit cell having 14-sided polyhedron with six square and eight hexagonal faces. The normalized fracture toughness of tetrakaidecahedral foam mainly depends on its relative density and is expressed in a similar relation to Equation 9. The relative density depends on the strut length l and dimension of strut (considered as equilateral triangle) h by $\frac{\rho_f}{\rho_s} = 0.4593\left(\frac{h}{l}\right)^2$.

The variation of mode I and mode II fracture toughness versus relative density for $l = 2$ mm is shown in Figure 16.

Arakere et al.[47] investigating the BX-265 foam insulation material, with 35.2 kg/m^3 density, used a solid 3D for middle tension specimen. The specimen was modelled as transversally isotropic linear elastic solid, and different crack orientations were defined for modes I, II and III combinations. Fracture toughness was estimated equating with the stress intensity factor obtained with the fracture load from tests.

Settgast et al.[56] modelled reticulated Kelvin open cell containing sharp edges cavities using 3D FE method. The interaction integral was employed to compute the local stress intensity factors under multiaxial loading. Using a homogenization approach, a criterion for brittle failure based on the effective stress state is presented.

Investigating the fracture behaviour of rigid closed-cell PVC foam Divinycell HT-90 (density 90 kg/m^3), Rizov and Mladensky[57] presented experimental and numerical results. The fracture toughness was calculated based on nodal displacement correlation from the near crack zone. A fracture toughness value of

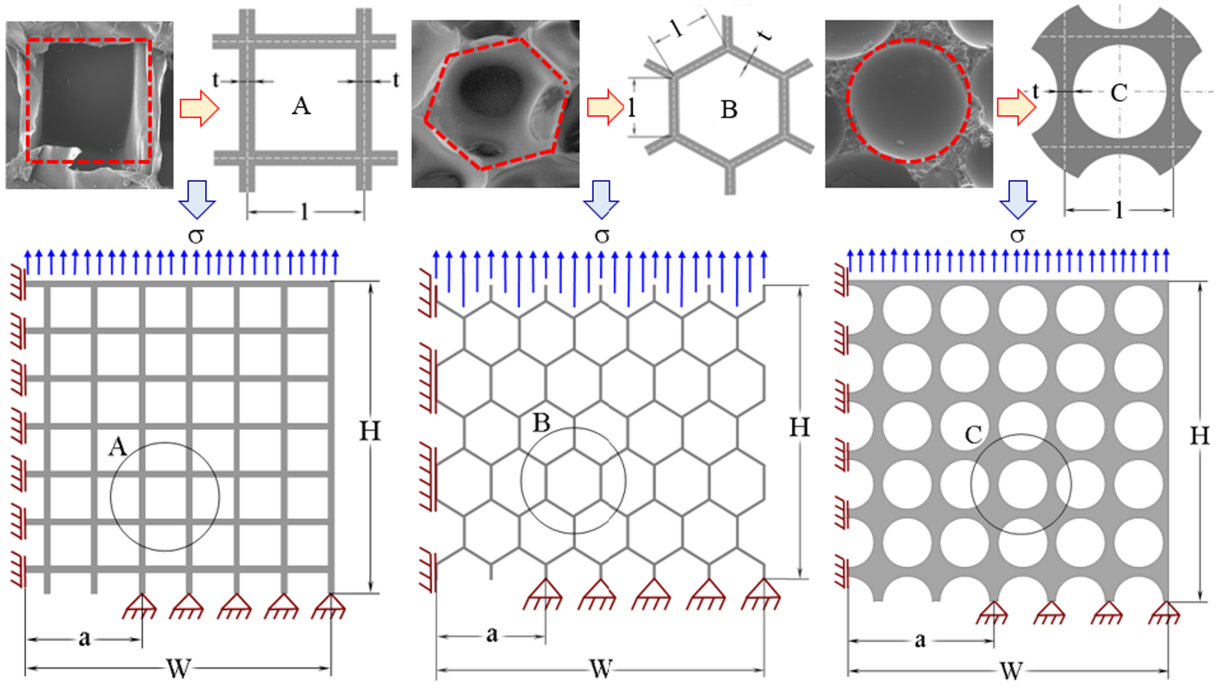

(A) square cells (B) hexagonal cells (C) circular cells

FIGURE 12 The 2D models dimensions and boundary conditions for square, honeycomb and circular cells[54] [Colour figure can be viewed at wileyonlinelibrary.com]

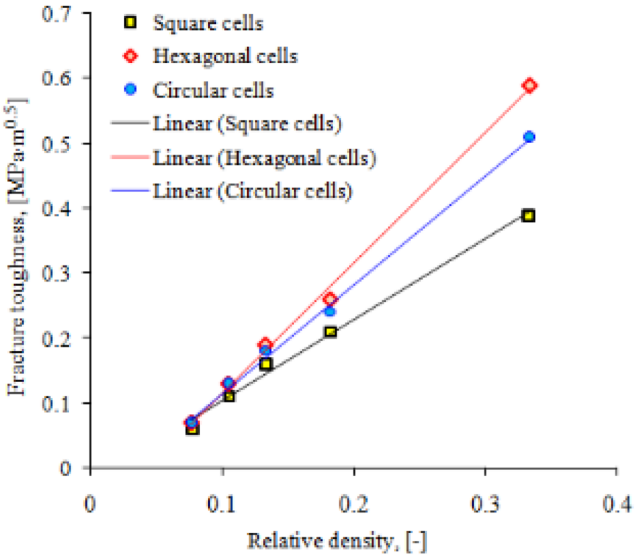

FIGURE 13 Fracture toughness versus relative density[54]
[Colour figure can be viewed at wileyonlinelibrary.com]

K_{IC} = 0.222 MPa $m^{0.5}$ was found, and it was concluded that the three-dimensional model represents an accurate tool for analysing the mechanical response of the compact tension (CT) specimen.

The FE micromechanical models offer an alternative to analytical micromechanical models. Most of the numerical investigations relate the fracture properties to solid material of the foam, relative density, cell size, cell shape, cellular topology, cell walls thickness and distributions of solids between struts and faces. Two and three-dimensional foam models were considered, with cells of different shapes (beams, 2D and 3D solids). Both mode I and II fracture toughness were predicted.

4 | EXPERIMENTAL DETERMINATION OF MODE I FRACTURE TOUGHNESS

The testing methods for mechanical characterization of polymeric materials are described in Landrock,[58] Brown,[59,60] Ward and Sweeney[61] and Park et al.[62] However, up to now, there are no standards for fracture toughness determination of polymeric foams. Most of the experiments were performed using the plane strain fracture toughness of plastic materials procedure from ASTM D5045-99.[63]

4.1 | Types of specimens

Single-edge notched bending (SENB) specimens (Figure 17A) and CT specimens (Figure 17B) are recommended because they exhibit a predominantly bending stress state, which allows smaller specimen sizes to achieve plane strain conditions. If the material is supplied in the form of a sheet, the specimen thickness, B, should be identical with the sheet thickness. The plain strain condition could be achieved only if specimen thickness B is big enough and the ligament in the crack area ($W - a$) is sufficient to avoid excessive plasticity. The introduction of a crack in the specimen is possible by machining a sharp notch. Subsequently, one can initiate a natural crack by inserting a fresh razor blade and tapping. If a natural crack cannot be successfully initiated by tapping, a sufficiently sharp crack can alternatively be generated by sliding or sawing with a new razor blade across the notch root.

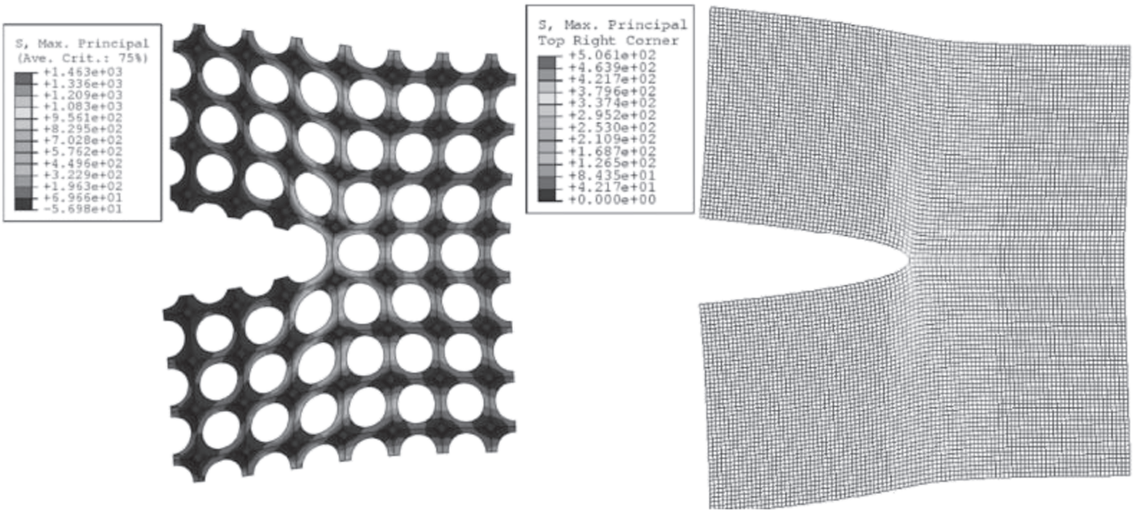

(A) Solid model (B) Beam model

FIGURE 14 Finite element micromechanical models[31]

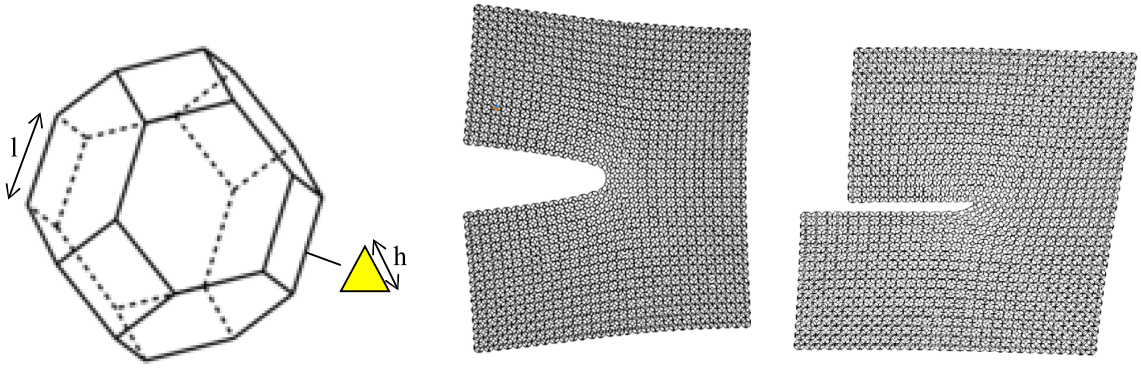

FIGURE 15 The tetrakaidecahedral unit cell and the cross section of a strut, adapted from Thiyagasundaram et al.[55] [Colour figure can be viewed at wileyonlinelibrary.com]

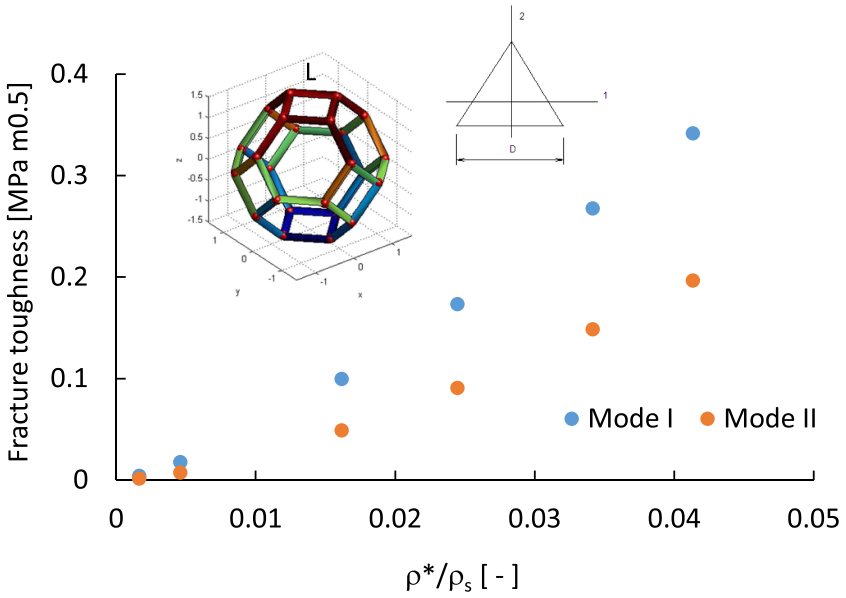

FIGURE 16 The fracture toughness versus relative density, adapted from Wang[49] [Colour figure can be viewed at wileyonlinelibrary.com]

Fowlkes[25] performed one of the first experimental investigation on fracture toughness of PUR foams with a density of 88 kg/m^3. He considered different types of specimens: middle cracked (MC) specimen (Figure 17C), double-edge crack specimen, single-edge crack (SEC) specimen (Figure 17D) and double cantilever beam (DCB) (Figure 17F) and determined the critical energy release rate G_{IC}. The results obtained on DCB were 0.22 kJ/m^2, and on the other specimens, 0.193 ± 10% kJ/m^2. He also highlighted that the fracture toughness results do not depend on specimen type, representing a material property. On the contrary, Poapongsakorn and Carlsson[64] using SENB specimens showed that symmetric four point-bending (FPB) loading (Figure 17A) gives a fracture toughness two times higher compared with loading in three-point bend (TPB) (Figure 17A) configuration, because of indentation that occurs in the cracked cross-section area, reducing the ligament size.

Figure 17 presents some of the most used specimens in fracture toughness tests of polymeric foams.

Table 2 summarizes the fracture toughness K_{IC} experimental results for different polymeric foams, different densities and specimen configurations from literature.

Because of the diversity of polymeric foams, specimen types and dimensions are hard to compare with those values of mode I fracture toughness. However, some correlations could be made. Most of the fracture tests were performed on one type of specimen SENB. Marsavina et al.[75,76] presented results of PUR foam fracture toughness using different types of specimens. Their results for three different densities and four types of specimens and loading configurations are summarized in Figure 18. It could be seen that the mode I fracture toughness values are similar, with the exception of those obtained on SEC specimens, which are higher with 12% (density 300 kg/m^3) to 32% (density 100 kg/m^3) than those obtained using SENB specimens loaded on TPB.

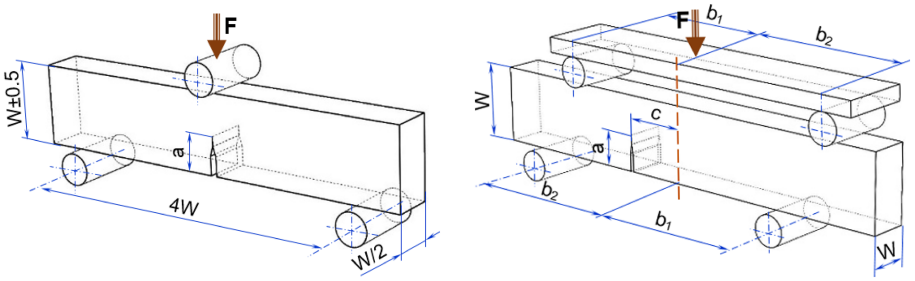

loaded in three point bending (TPB) loaded in four point bending (FPB)

(A) Single Edge Notch Bend (SENB) specimen

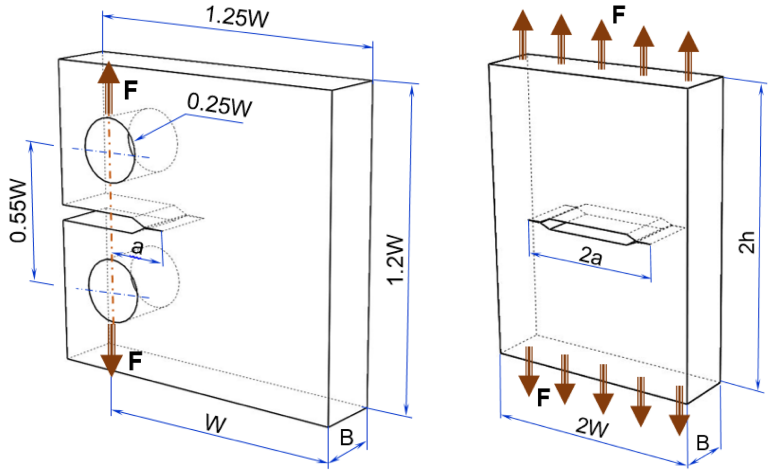

(B) Compact Tension (CT) specimen (C) Middle Crack (MC) specimen

FIGURE 17 Types of specimens for fracture toughness tests [Colour figure can be viewed at wileyonlinelibrary.com]

4.2 | Influence of solid material

Kabir et al.[67] compared the fracture toughness of PVC and PUR foams of 260-kg/m^3 density and highlighted that $K_{IC,PVC}$ is 2.2 times higher than those obtained for PUR $K_{IC,PUR}$. Similar results could be seen if we compare the foams with 100-kg/m^3 density for H100 PVC foam (Viana and Carlsson[66]) and PUR 100 (Marsavina et al.[75]) (Table 2). All these results together with the foam microstructure are shown in Figure 19. This figure could be explained on one hand on the higher fracture toughness of solid material PVC $K_{IC,PVCs}$ = 2.45 MPa m$^{0.5}$ in comparison with PUR $K_{IC,PURs}$ = 0.35 MPa m$^{0.5}$. In addition, the topology of the compared foams is different: PVC foams have a hexagonal structure, whereas the PUR ones have a spherical microstructure (Figure 19).

Bureau and Kumar[78] investigated the fracture toughness of microcellular polycarbonate foam with relative density between 0.7 (density 830 kg/m^3) and 0.9 (density 1073 kg/m^3) manufactured by solid-state foam and obtained fracture toughness values between 2.6 ± 0.1 and 4.3 ± 0.3 MPa m$^{0.5}$.

Saenz et al.[79] experimentally determined the fracture toughness G_{IC} (in kJ/m^2) of PVC and PES foam using SENB and DCB specimens. Their results are shown in Table 3.

It also could be observed that at almost the same density (54 kg/m^3), the fracture toughness of PES-P50 foam is 52% higher compared with the corresponding density of PVC foam (H60). The authors explain that the cross-inked PVC foams failed in a linear elastic brittle manner, whereas the thermoplastic PES foams displayed much more ductility and substantially higher fracture toughness. The differences on fracture toughness for the same PVC foam density obtained using SENB, respectively DCB specimens are due to the different loading speeds and specimen orientation. The SENB specimens were cut out-of-plane and tested at 12.7 mm/min, whereas the DCB specimens were cut in-

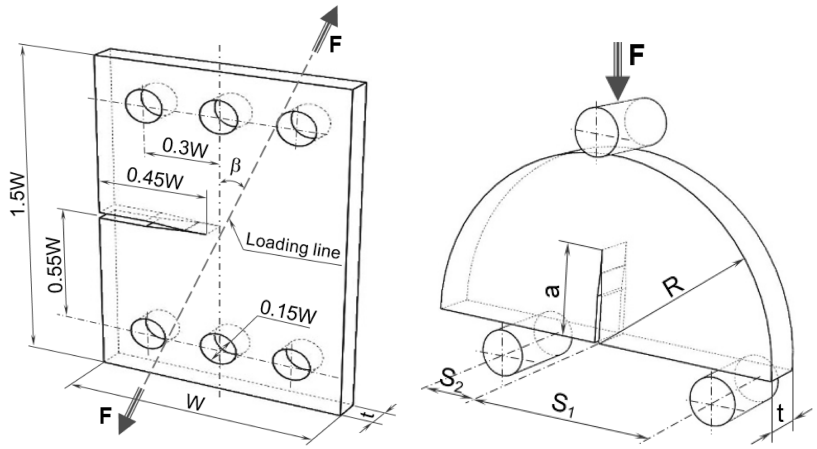

(D) Single Edge Crack (SEC) specimen (E) Asymmetric Semi Circular Bend (ASCB) specimen

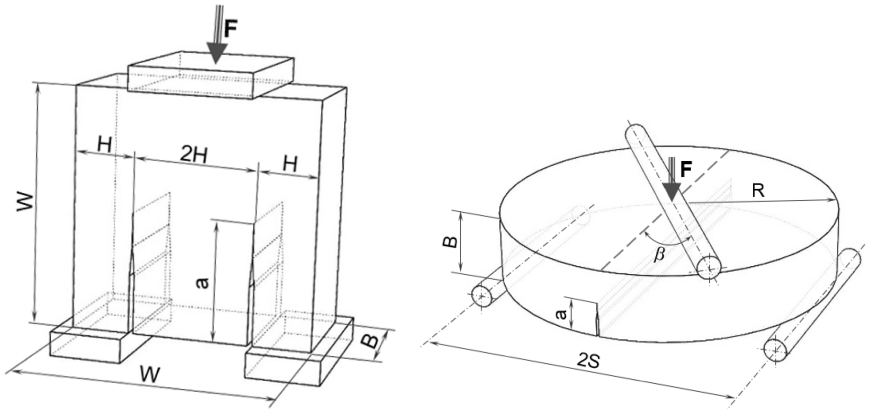

(F) Compact Shear (CS) specimen (G) Edge Notch Bend Disc (ENDB) specimen

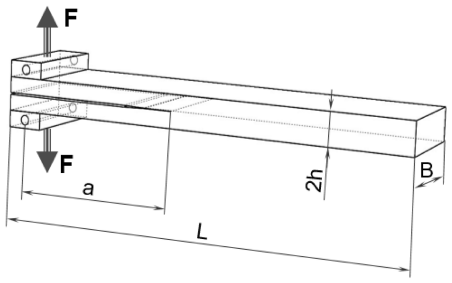

f. Double Cantilever Beam (DCB) specimen

FIGURE 17 (Continued)

plane and tested at 1.27 mm/min. Similar results for G_{IC} of H100 PVC foam obtained using DCB specimens with different core thicknesses (from 3.18 to 40.6 mm) were obtained by Matteson et al.[80] and Shivakumar et al.,[81] and the G_{IC} values range between 1.02 and 0.88 kJ/m^2.

Saenz et al.[82,83] also investigated the propagation of crack in PVC and PES foams using SEC specimens loaded in tensile and concluded that for both foams, the cells failed in a stretching mode of deformation.

4.3 | Influence of loading speed

The influence of density and loading speed for PVC foams was presented by Kabir et al.[67] The fracture toughness increases with loading speed, and this increase is lower for the high-density foam: 22% for 75-kg/m^3 density, respectively 18% for 260-kg/m^3 density, considering a 100 times increase of loading speed (Figure 20A). This increase appears only for loading in flow direction, whereas in the rise direction, the loading speed has

TABLE 2 Fracture toughness K_{IC} values of polymeric foams

Foam type/grade	Density ρ_f (kg/m^3)	Specimen type	Crack length a (mm)	Fracture toughness K_{IC} (MPa m$^{0.5}$)	References
PUR	35	SENB/TPB	Not available	0.010	McIntyre and Anderton[65]
PUR	55	SENB/TPB	Not available	0.024	
PUR	79	SENB/TPB	Not available	0.035	
PUR	88	SENB/TPB	Not available	0.039	
PUR	97	SENB/TPB	Not available	0.038	
PUR	112	SENB/TPB	Not available	0.054	
PUR	120	SENB/TPB	Not available	0.046	
PUR	135	SENB/TPB	Not available	0.067	
PUR	155	SENB/TPB	Not available	0.085	
PUR	158	SENB/TPB	Not available	0.087	
PUR	160	SENB/TPB	Not available	0.097	
PUR	222	SENB/TPB	Not available	0.107	
PUR	280	SENB/TPB	Not available	0.202	
PUR	356	SENB/TPB	Not available	0.238	
PUR	358	SENB/TPB	Not available	0.243	
PVC/H30	36	SENB/TPB	19.5	0.064	Viana and Carlsson[66]
PVC/H80	80	SENB/TPB	18.5	0.117	
PVC/H100	100	SENB/TPB	27.6	0.168	
PVC/H200	200	SENB/TPB	24.0	0.370	
PVC/R400	400	SENB/TPB	13.5	0.450	
PVC/R75	75	SENB/TPB	$0.40 < a/W < 0.60$	0.09	Kabir et al.[67]
PVC/H130	130	SENB/TPB	$0.40 < a/W < 0.60$	0.28	
PVC/HD130	200	SENB/TPB	$0.40 < a/W < 0.60$	0.47	
PVC/R260	260	SENB/TPB	$0.40 < a/W < 0.60$	0.63	
PUR/240	240	SENB/TPB	$0.40 < a/W < 0.60$	0.32	
PUR	40	SENB/TPB	12.0	0.034	Marsavina and Linul[68]
PUR	80	SENB/TPB	12.0	0.058	
PUR	120	SENB/TPB	12.0	0.120	
PUR	140	SENB/TPB	12.0	0.153	
PUR	145	SENB/TPB	12.0	0.210	
PUR	200	SENB/TPB	12.0	0.390	
PUR	300	SENB/TPB	12.0	0.590	
PVC/H45	46.1	SENB/TPB	$0.45 < a/W < 0.55$	0.05	Poapongsakorn and Carlsson[64]
PVC/H60	60.4	SENB/TPB	$0.45 < a/W < 0.55$	0.07	
PVC/H100	100	SENB/TPB	$0.45 < a/W < 0.55$	0.13	
PVC/H130	121	SENB/TPB	$0.45 < a/W < 0.55$	0.16	
PVC/H200	208	SENB/TPB	$0.45 < a/W < 0.55$	0.35	
PVC/H45	46.1	SENB/FPB	$0.45 < a/W < 0.55$	0.09	
PVC/H60	60.4	SENB/FPB	$0.45 < a/W < 0.55$	0.13	
PVC/H100	100	SENB/FPB	$0.45 < a/W < 0.55$	0.25	
PVC/H130	121	SENB/FPB	$0.45 < a/W < 0.55$	0.31	

(Continues)

TABLE 2 (Continued)

Foam type/grade	Density ρ_f (kg/m^3)	Specimen type	Crack length a (mm)	Fracture toughness K_{IC} (MPa m$^{0.5}$)	References
PVC/H200	208	SENB/FPB	0.45 < a/W < 0.55	0.63	
PMI/WF51	52	SENB/TPB	0.20 < a/W < 0.80	0.08	Burman[69]
PVC/H100	100	SENB/TPB	0.20 < a/W < 0.80	0.21	
PIR	34	CT	Not available	0.010	Andersons et al.[70]
PIR	41	CT	Not available	0.012	
PIR	53	CT	Not available	0.017	
PIR	64	CT	Not available	0.019	
PUR	32	CT	Not available	0.022	
PUR	51	CT	Not available	0.038	
PUR	77	CT	Not available	0.055	
PUR	84	CT	Not available	0.058	
PUR	320	SENB	10.2	0.215	Jin et al.[71]
Styrene/A800	150	SENB	Not available	0.334	Kidane[72]
Styrene/A1200	210	SENB	Not available	0.435	
PUR	100	SENB/FPB	12.0	0.075	Apostol et al.[73,74]
PUR	145	SENB/FPB	12.0	0.100	
PUR	300	SENB/FPB	12.0	0.369	
PUR	100	ASCB	20.0	0.087	Marsavina et al.[75]
PUR	145	ASCB	20.0	0.131	
PUR	300	ASCB	20.0	0.372	
PUR	100	SEC	33.75	0.131	Marsavina et al.[76]
PUR	145	SEC	33.75	0.140	
PUR	300	SEC	33.75	0.421	
PUR	100	ENDB	15.0	0.091	Aliha et al.[77]
PUR	145	ENDB	15.0	0.112	
PUR	300	ENDB	12.5	0.344	

practically no influence. Poapongsakorn and Carlsson[64] investigated the influence of crosshead rate and cell size for three different 60-kg/m^3 PVC foams (two normal H60, H60N and one with large cells H60L) using SENB specimen loaded in FPB. Three different cross speed rates were considered 0.254, 1.27 and 12.7 mm/min. The results show that crosshead rate does not have significant influence on the fracture toughness for foams with normal cells H60 and H60N. The H60L foam with large cells tested at a low rate of 0.245 mm/min displayed low fracture toughness values.

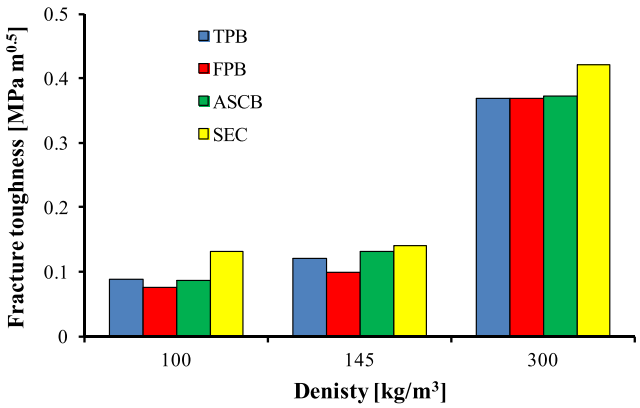

FIGURE 18 Influence of specimen type on fracture toughness[75,76] [Colour figure can be viewed at wileyonlinelibrary.com]

For PUR foam with 140-kg/m^3 density, the fracture toughness decreases with 11% when loading speed increases 200 times.[68] The different tendency could be again explained on the topology of the cells.

4.4 | Influence of foam anisotropy

Cellular materials and particularly foams are often anisotropic, and their properties depend on the direction in

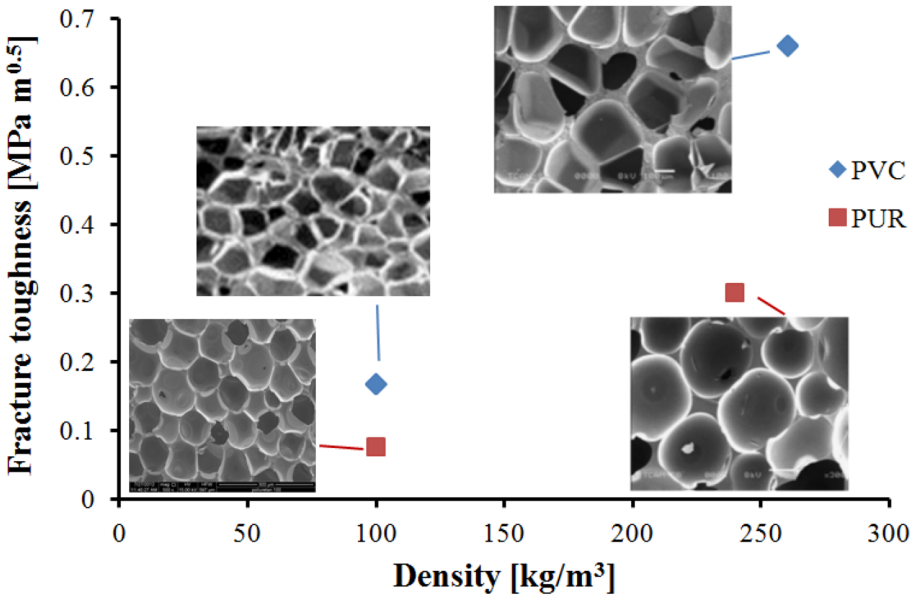

FIGURE 19 Influence of solid material on fracture toughness [Colour figure can be viewed at wileyonlinelibrary.com]

TABLE 3 Fracture toughness of PVC and PES foams[79]

Foam type		Density (kg/m³)	Fracture toughness G_{IC} (kJ/m²) SENB	DCB
PVC	H45	48.3 ± 0.39	0.11 ± 0.01	0.24 ± 0.03
	H60	54.9 ± 0.63	0.24 ± 0.01	0.38 ± 0.04
	H100	107.0 ± 1.79	0.43 ± 0.04	0.89 ± 0.05
PES	P50	54.3 ± 0.84	-	0.58 ± 0.15
	P90	86.0 ± 4.04	-	0.72 ± 0.08
	F130	125.0 ± 4.53	-	1.53 ± 0.30

which they were measured.[2] Huber and Gibson[84] proposed scaling relations for mode I fracture toughness of brittle anisotropic foams, using rectangular parallelepiped unit cell of foams and brittle fracture in bending as the crack growth mechanism. The fracture toughness of an anisotropic foam depends on the direction in which the crack propagates. The anisotropy is influenced by the cell dimensions and topology, which could be identified for three directions: two in the flow direction, in-plane (1), (2) and one out-of-plane corresponding to rise direction (3) (Figure 21).

The average geometrical anisotropy factor defined as follows[70]:

$$Q = \frac{1}{N}\sum_{i=1}^{N}\frac{l_{R,i}}{l_{F,i}} \tag{22}$$

is based on the geometrical dimensions h (cell dimension in the rise direction) and l (cell dimension in the flow direction), with N the number of cells for a given sample. They correlate the ratio between fracture toughness on different direction to the ratio of cell dimensions $Q = l_{\text{rise}}/l_{\text{flow}}$:

$$\frac{(K_{IC})_i}{(K_{IC})_j} = Q^N \tag{23}$$

with $i, j = 1, 2, 3$ direction, $N = 0.5, 1, 1.5$.

Figure 22 presents the analytical predictions of $K_{IC\_\text{rise}}/K_{IC\_\text{flow}}$ versus h/l given by Equation 23, together with the experimental results for

- SENB specimens (yellow circle for 100-kg/m³ density, blue circle for 145-kg/m³ density and black circle for 300-kg/m³ density);
- ASCB specimens for 100-kg/m³ density (yellow square) and 145-kg/m³ density (blue square) obtained for PUR foams[75,76];
- MT specimens of 35.2-kg/m³ BX-265 PUR foam[47];
- SENB specimens from PVC foam of density 130 kg/m³.[67]

It could be observed that the ratio $K_{IC\_\text{rise}}/K_{IC\_\text{flow}}$ is higher than 1, and the anisotropy decreases with increasing the foam density.

Ganpatye and Kinra,[85] investigating the fracture toughness of low-density (35.2 kg/m³) polyurethane closed-cell foam BX-265, used for insulation of external tanks of space shuttles, highlighted similar anisotropy effect $(K_{IC})_{32}/(K_{IC})_{21} = 1.43$, where $(K_{IC})_{32} = 0.029$ MPa m$^{0.5}$ and $(K_{IC})_{21} = 0.020$ MPa m$^{0.5}$.

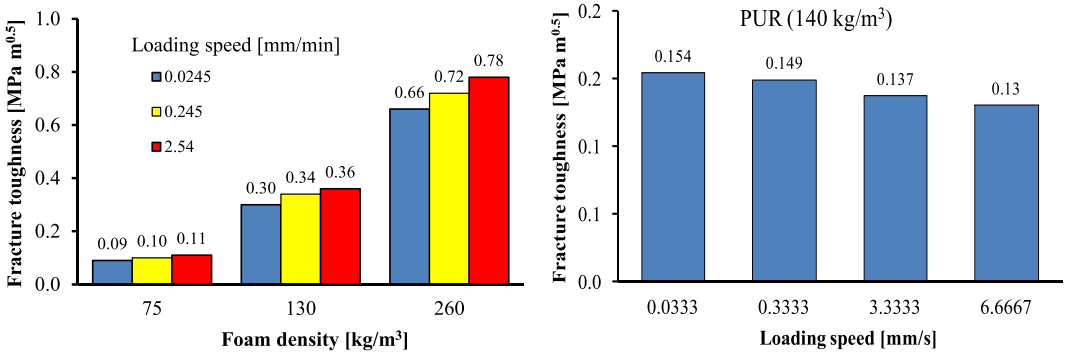

(A) PVC foam[64] (B) PUR foam[68]

FIGURE 20 Influence of loading speed on fracture toughness [Colour figure can be viewed at wileyonlinelibrary.com]

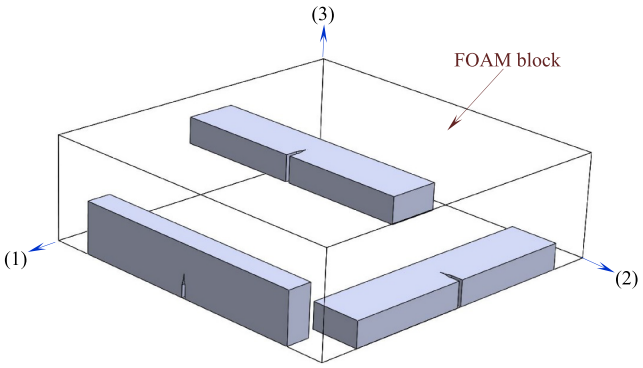

FIGURE 21 Single-edge notched bending specimens orientation [Colour figure can be viewed at wileyonlinelibrary.com]

4.5 | Influence of testing temperature

The main physical and mechanical properties of different polymeric foams have been investigated in detail by different researchers under low temperatures (between 0°C and −196°C), especially at cryogenic temperature.[86–92] On the other hand, the literature presents very limited studies regarding the determination of fracture toughness values under extreme temperature conditions. Knudsen[93] presents a summary of tests performed at NASA for BX-265 foam insulation at room temperature and −178°C, using different types of specimens (SENB, MC and CT).

Fracture mechanics experimental tests of cellular materials under low- or high-temperature conditions are very difficult to perform, both due to the clamping devices and to the cooling/heating installations.

Using an insulation chamber, Yu et al.[94] investigated the K_{IC} of the neat (unreinforced) and chopped glass fibre (CGF) reinforced polyurethane foams (70 kg/m^3) at cryogenic temperature. The authors adopted the eccentrically loaded, CT specimen, and they used CGF lengths of 7-mm length and different percentages. The experimental tests were performed at −150°C, using a CGF length of 7 mm and different percentages of CGF (2.5, 5.0, 7.5 and 10.0 wt%). The authors observed that the K_{IC} increased as the weight percentages of the CGF were increased. More precisely, the K_{IC} of the CGF reinforced PUR foam increased by 360% at −150°C with the reinforcement of 10 wt% of CGF. Furthermore, because of the increase of

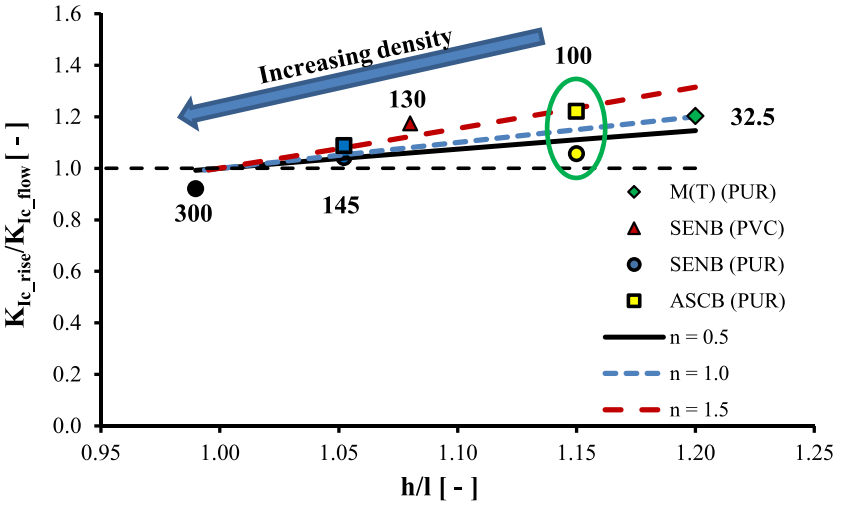

FIGURE 22 Influence of foam anisotropy [Colour figure can be viewed at wileyonlinelibrary.com]

brittleness of PUR foam, they observed that the K_{IC} of the neat PUR foam decreased at the cryogenic temperature compared with that of the room temperature. However, the K_{IC} of the CGF reinforced PUR foams increased more at −150°C than that at the room temperature (by about 20%). According to their SEM images, this phenomenon is associated with the bridging effect that will increase the intermolecular force of the polyurethane polymer during cryogenic temperature tests. When the crack tip propagates, some bridged CGFs will be pulled out from the PUR foam, which will dissipate much the strain energy stored in the reinforced foam. The dissipation of strain energy will increase the K_{IC} of the CGF reinforced foam.[95]

Recently, Linul et al.[96] determined the quasi-static K_{IC} of rigid PUR foams under cryogenic temperature by using SENB specimens. The authors investigated both the influence of foam density (100, 145 and 300 kg/m^3) and foam anisotropy (in-plane and out-of-plane loading direction) at −196°C (the specimens being totally immersed in liquid nitrogen). They found that the cryogenic temperature in-plane K_{IC} values are lower than the out-of-plane ones with about 16%, especially for low densities, whereas for high densities, the K_{IC} difference is below 6%. Moreover, regardless of foam density and loading direction, all PUR foam specimens highlighted a significant increase in K_{IC} at −196°C, compared with room temperature (i.e., 30%–39% for 100 and 145 kg/m^3, and 15% for 300 kg/m^3) (Figure 23). It seems that because of the different test parameters (e.g., different cooling systems of the specimens, different testing temperature, different test type and different specimen shape) and foam type (e.g., foam density and foam microstructure), the results reported by Yu et al.[94] and Linul et al.[96] highlight different answers.

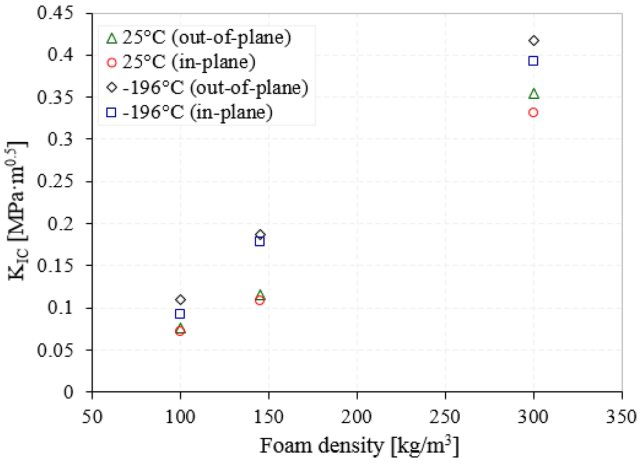

FIGURE 23 In-plane and out-of-plane K_{IC} results according to operating temperature[96] [Colour figure can be viewed at wileyonlinelibrary.com]

Based on their data, Linul et al.[96] proposed a linear correlation for estimation of K_{IC} at cryogenic temperature ($K_{IC,-196}$) according to room temperature values, in the form of Equation 24:

$$K_{IC,-196} = 1.0728\ K_{IC,+25} + 0.0405 \quad \text{with} R^2 = 0.9825. \tag{24}$$

4.6 | Size effect

It was proven that the brittle materials exhibit a pronounced size effect.[97] The size effect on fracture of polymeric foams (PVC, density 100 kg/m^3) was first investigated by Bazant et al.[98] They used notched tensile specimens with the same thickness (25.40 mm) but having three different widths (6.35, 43.94 and 304.80 mm) and a constant length to width ratio (5:2). According to their results, a strong size effect in closed cell PVC foams occurs. The foams behaviour agrees well the size effect law of Bazant,[99] based on asymptotic matching, which represents a smooth transition between asymptotic case corresponding to LEFM and no size effect.

Linul et al.[100] and Marsavina et al.[75] studied the size effect on PUR foams by using SENB specimens. They investigated the dependence of the nominal stress $\sigma_N = (3P_{max}S)/(2BW^2)$ as a function of the characteristic size of the specimen W, in this case, the specimen width. The specimens were cut from plates and had the same thickness B of approximately 53 mm for PUR foams of 100- and 145-kg/m^3 density, respectively 25 mm for 300 kg/m^3. Similar geometrical specimens with different width W = 5.5 (XS), 10.0 (S), 25.4 (M), 53.7 (L) and 224.5 (XL) mm and length-to-width ratio 4 were tested in TPB. Typical load–displacement curves obtained for testing the different size specimens are shown in Figure 24 for 100-kg/m^3 foam density. The results are plotted in Figure 25; in logarithmic coordinates Log (σ_N) versus Log (W), the markers represent the average experimental results and the black line the asymptotic Equation 25. If the failure of the foam obeys LEFM, the logarithmic size effect plot would have to be a straight line with the slope −1/2, shown dotted in Figure 25. A ductile behaviour following the strength criteria (SC) with no size effect would be a horizontal line $\sigma_N = \sigma_f$, with σ_f fracture or yield stress of the foam. The obtained experimental results are asymptotic to these approaches having the form[97,99]:

$$\sigma_N = \frac{\sigma_{N0}}{\sqrt{1 + \frac{W}{W_0}}} \tag{25}$$

where σ_{N0} and W_0 are fitting parameters.

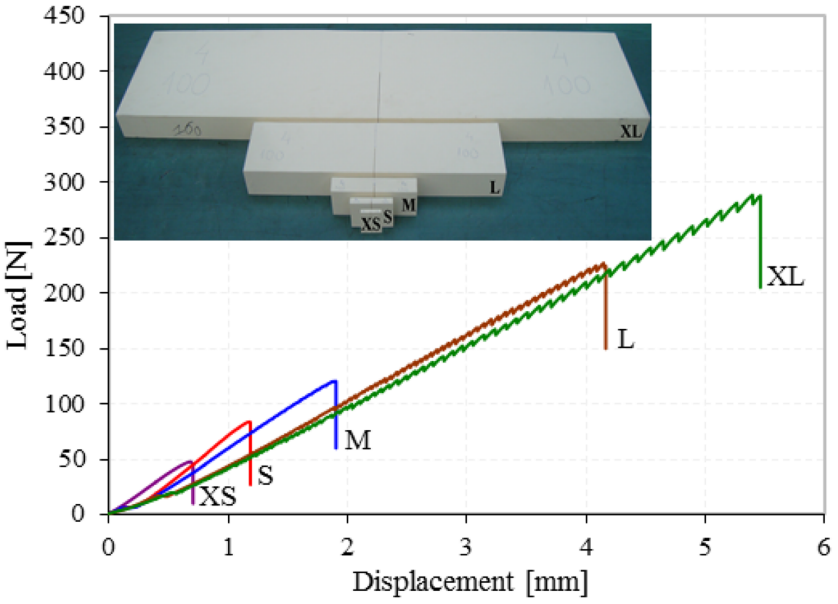

FIGURE 24 Typical load–displacement curves for different specimen sizes of foam with 100-kg/m^3 density [Colour figure can be viewed at wileyonlinelibrary.com]

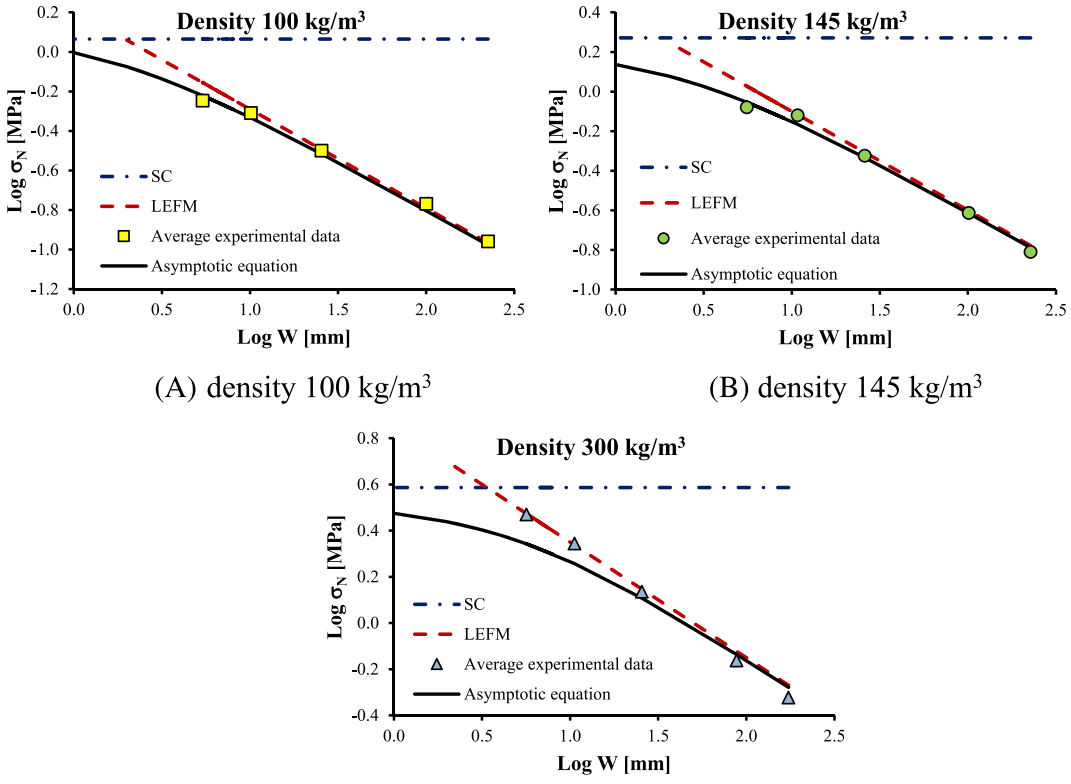

(A) density 100 kg/m^3 (B) density 145 kg/m^3

(C) density 300 kg/m^3

FIGURE 25 The size effect of three different PUR foam densities with single-edge notched bending specimens subjected to three-point bending [Colour figure can be viewed at wileyonlinelibrary.com]

It can be seen that for all specimen sizes, the LEFM fits better the experimental results. The fitting parameters from Equation 25 σ_{N0} and W_0 increase with foam density and are shown in Table 4. These results show that the design of PUR foam structures based on strength or plasticity criteria is generally valid only for small structural parts, whereas for large components, the LEFM concepts should be used.

Touliatou and Wheel[101] observed also a prominent size effect on brittle materials with low and medium

TABLE 4 Size effect results

Density (kg/m^3)	Cell size (mm)	σ_f (MPa)	σ_{N0} (MPa)	W_0 (mm)
100	0.104	1.16	1.275	1.542
145	0.084	1.87	1.651	2.232
300	0.068	3.86	3.297	4.545

porosity. As the specimen size increases, the material becomes less tough, until it converges to a specific value. As expected, a weakening effect is also exhibited with increasing porosity.

5 | MIXED-MODE FRACTURE TOUGHNESS

Structures containing foams, such as sandwich structures, are often subjected to mixed-mode loading. However, only few fracture toughness results are published for mixed-mode loading of plastic foams.

5.1 | Phenomenological models

The interpretation of in-plane mixed-mode (opening and in-plane shear) fracture results were based on the well-known phenomenological fracture criteria, which implies a relationship between stress intensity factors (K_I and K_{II}) and the fracture toughness (K_{IC}): $f(K_I, K_{II}, K_{IC}) = 0$, respectively the angle of crack initiation θ_c.

Among these criteria, the *maximum circumferential tensile stress* (MTS) of Erdogan and Sih,[102] *minimum strain energy density* (SED) of Sih,[103] *maximum energy release rate criterion* (Gmax) of Hussain et al.[104] and *equivalent stress intensity factor* (ESIF) of Richard[105,106] are often employed. Hallsträm and Grenestedt[107] investigated mixed-mode fracture of cracks and wedge-shaped notches in expanded PVC foams. Different types of specimens made of Divinycell H100 were investigated and the non-singular *T*-stress was considered in the formulation of fracture criteria. It was concluded that for predominantly mode II, the use of *T*-stress improved the facture predictions. Noury et al.[108] tested three different PVC foams densities (90, 130 and 200 kg/m^3) using a SEC specimen with Arcan grips in order to produce mixed-mode conditions. Figure 26 presents their results together with fracture envelopes based on the mentioned criteria. It could be concluded that for rigid PVC foams the Richard's ESIF criterion is most reliable to predict mixed-mode fracture. This could be also explained by the fact that it takes into account the ratio between mode I and mode II fracture toughness $\alpha = K_{IC}/K_{IIC}$.

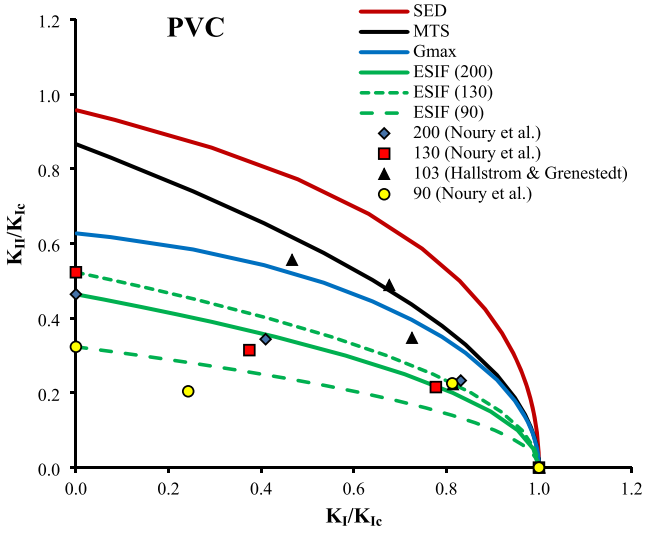

FIGURE 26 Mixed-mode fracture results for PVC rigid foams, adapted from Hallsträm and Grenestedt[107] and Noury et al.[108] [Colour figure can be viewed at wileyonlinelibrary.com]

Burman[69] experimentally determined the mode I (on CT specimens) and mode II (on end notched flexure specimens) fracture toughness of PVC foam Divinicell H100 (density 100 kg/m^3) and WF51 (density 52 kg/m^3) resulting: $K_{IC,H100} = K_{IIC,H100} = 0.21$ MPa m$^{0.5}$, respectively $K_{IC,WF51} = 0.08$ MPa m$^{0.5}$, $K_{IIC,WF51} = 0.13$ MPa m$^{0.5}$.

Marsavina et al.[75] using ASCB specimens, Linul et al.[109,110] on SEC specimens and Apostol et al.[111] on SENB specimens loaded on FPB presented extensive studies on the assessment of mixed-mode fracture criteria for PUR foams. The experimental results and fracture envelopes are summarized in Figure 27A–C. Figure 27 presents the mean values of the ratio between K_{II}/K_{IC} versus K_I/K_{IC}, together with the fracture curves predicted by the phenomenological criteria. For foams with densities 100 and 145 kg/m^3, the effect of cell orientation was also investigated.

It can be observed that for low-density foams (100- and 145-kg/m^3 densities), the experimental results fall between the G_{max} and ESIF criteria for all types of specimens, whereas for the foam with 300 kg/m^3, the experimental data are more scattered and close to SED and ESIF criteria. Based on these results, it could be concluded that also for rigid PUR foams, Richard's ESIF criterion is most reliable to predict mixed-mode fracture. This could be explained by the fact that Richard[105] criteria trigger the fracture data with $\alpha = K_{IC}/K_{IIC}$. The mixed-mode fracture is slightly different on the two considered cell orientations (rise and flow directions) (Figure 27A,B).

An important parameter for mixed-mode loading is the ratio between mode II and mode I fracture toughness

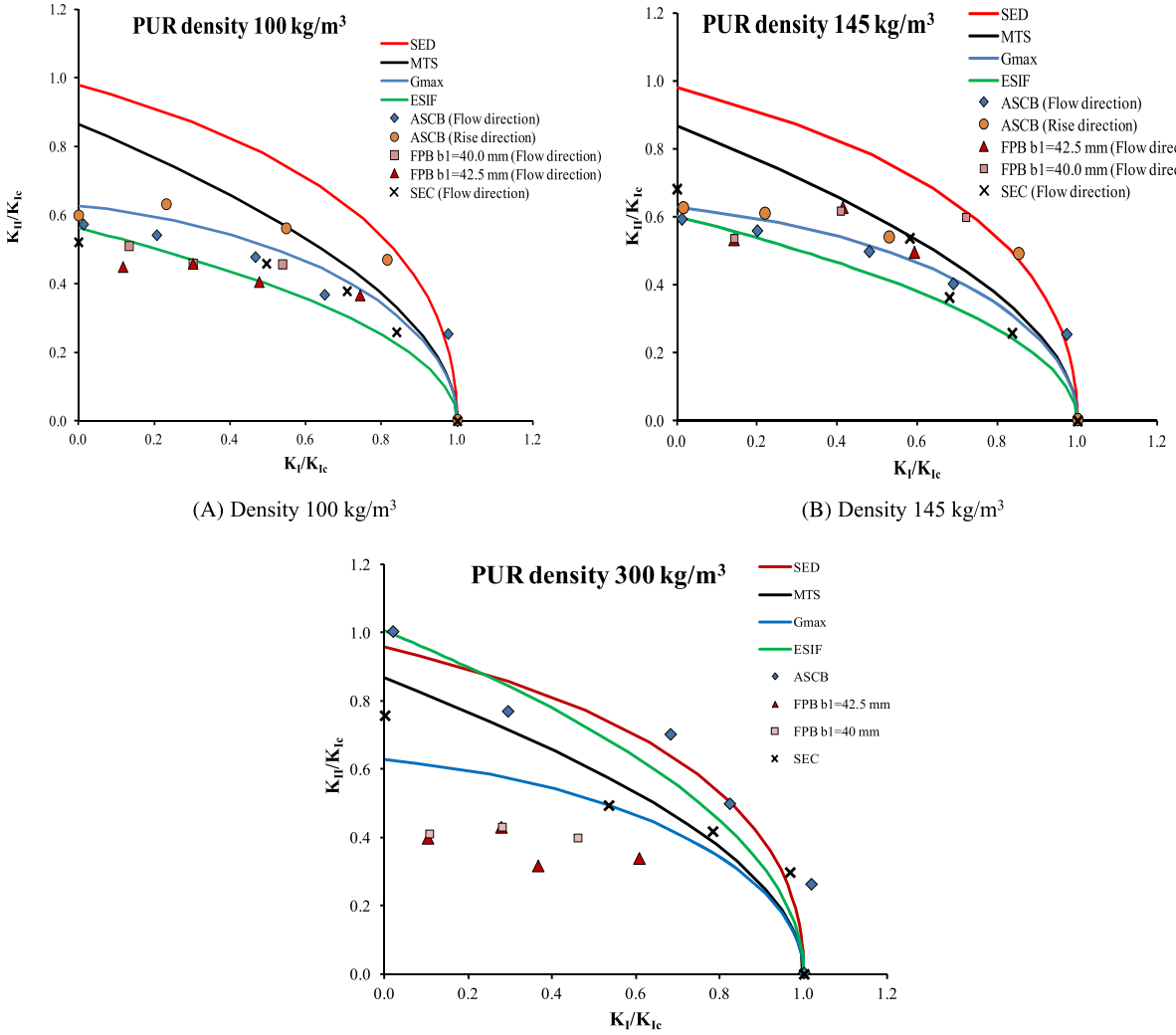

(A) Density 100 kg/m^3

(B) Density 145 kg/m^3

(C) Density 300 kg/m^3

FIGURE 27 Mixed-mode fracture results for rigid PUR foams of different densities, based on Marsavina et al.[75] on asymmetric semicircular bend (ASCB) specimens, Linul et al.[109,110] on single-edge crack (SEC) specimens and Apostol et al.[111] on single-edge notched bending specimens loaded in four-point bending (FPB) [Colour figure can be viewed at wileyonlinelibrary.com]

K_{IIC}/K_{IC}. Experimental results performed on ASCB, SENB loaded in TPB and FPB and SEC highlighted that ratio K_{IIC}/K_{IC} is between 0.47 and 1 for PUR foams increasing with density, which is in agreement with results of Noury et al.[108] for PVC foam with a ratio in the range 0.36 to 0.6 (Figure 28).

Figure 29 presents the mean values of the crack initiation angle θ_c measured on ASCB and SEC PUR foam specimens versus applied mixed-mode loading $Me = (1/\pi)\tan^{-1}(K_{II}/K_I)$, side by side with the predicted crack initiation angles predicted by fracture criteria. It could be observed that for predominantly mode I loadings $Me < 45^\circ$, the measured values of the crack initiation angle are in good agreement with the predicted ones. For predominantly mode II loading ($Me > 45^\circ$), the experimental crack propagation angles differ to the predicted values, the closest to the phenomenological predictions were obtained for SEC specimens.

Simulation of crack initiation and propagation in PUR foams was investigated numerically using extended FE method by Marsavina et al.[112,113] for mixed-mode cracks and by Apostol et al.[114] for mode II cracks. In both studies, the simulated crack propagation paths are in good agreement with the observed experimental paths (Figure 30).

As an important conclusion to be drawn is that the phenomenological fracture criteria, developed for solid materials, could be successfully extended to predict the fracture limit and the crack initiation angle for foam materials.

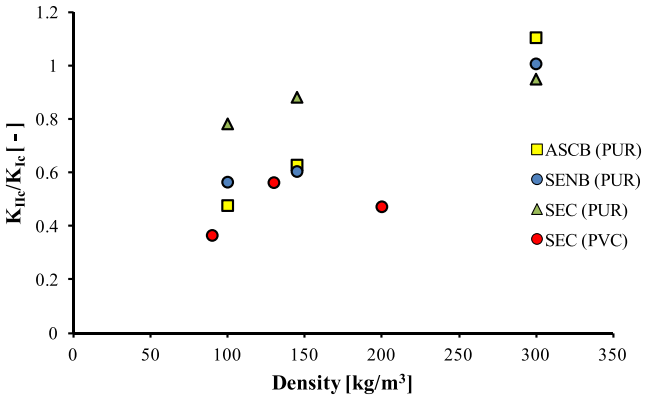

FIGURE 28 The ration K_{IIC}/K_{IC} versus density for PUR foams (asymmetric semicircular bend [ASCB] specimens from Marsavina et al.,[75] single-edge notched bending [SENB] in three-point bending from Marsavina et al.,[68] SENB in four-point bending from Apostol et al.,[73,74] single-edge crack (SEC) from Linul and Marsavina[110] and PVC foam from Noury et al.[108]) [Colour figure can be viewed at wileyonlinelibrary.com]

5.2 | Empirical models

Empirical relationships between ratios K_{II}/K_{IIC} and K_I/K_{IC} were proposed in the literature to assess mixed-mode fracture.[115,116] A general relation can be expressed in the form:

$$\left(\frac{K_I}{K_{IC}}\right)^p + \left(\frac{K_{II}}{K_{IIC}}\right)^q = 1 \tag{26}$$

where p and q are fitting parameters. The parameters can be equal $p = q = \alpha$ according to Lim et al.,[115] or $p \neq q$ ($p = 1$ and $q = 2$).[116] For exemplification empirical prediction, for $\alpha = 1.5$, 1.75 and 2 respectively $p = 1$ and $q = 2$, are plotted with the experimental fracture toughness results obtained on PUR specimens of three different densities and two types of specimens (ASCB and SEC) and indicate a good correlation for all foam densities (Figure 31).

In a recent study, Aliha et al.[77] presented some results on mode III and mixed-mode (I + III) fracture toughness of PUR foams. They employed edge-notched disc bend (ENDB) specimens, for three foam densities (100, 145 and 300 kg/m^3). The specimen dimensions were $R = 75$ mm, $B = 30$ mm, $a = 15$ mm and $S = 37$ mm (Figure 32). The experimental data expressed in the fracture plane K_{III}/K_{IC} versus K_I/K_{IC} show good agreement with the maximum tangential strain energy density (MTSED) criterion (Figure 33).

They also investigate the crack initiation angle and propagation paths for mixed-mode I and III (Figure 34).[117]

The experimental studies for determining K_{IC} were performed using wide range of specimens and different solid materials (PUR, PVC and PIR). The obtained results vary between 0.01 and 0.63 MPa m$^{0.5}$. The effect of loading speed, foam anisotropy, testing temperature and the size effect was also experimentally investigated. Fewer studies investigated the fracture criteria under mixed-mode loading (I + II and I + III) and the crack initiation angle, using phenomenological or empirical models.

6 | DYNAMIC FRACTURE TOUGHNESS

There are only few results reported in the literature regarding the dynamic fracture toughness of plastic foams. Kabir et al.[67] investigated the mode I dynamic fracture toughness of PVC foam with 260-kg/m^3 density and obtained a maximum value of 2.74 MPa m$^{0.5}$, which is approximately 3.75 times higher than the static fracture toughness of the same foam.

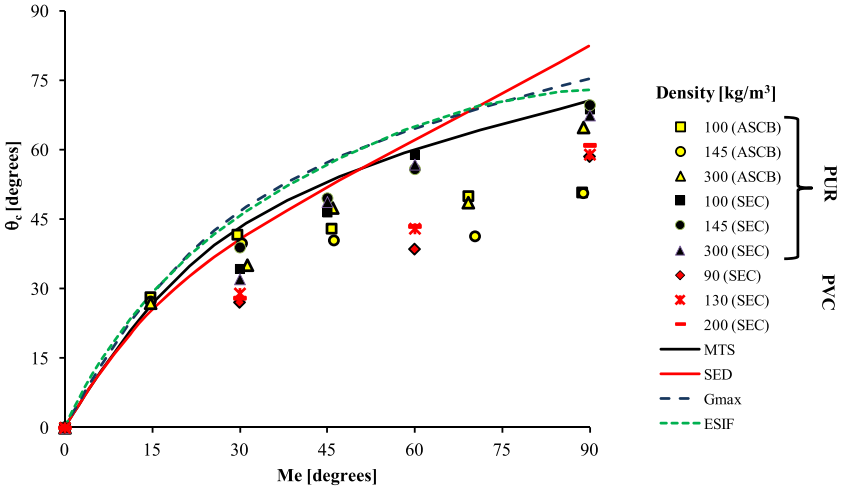

FIGURE 29 Comparison of predicted and experimental crack initiation angles[75,108,109] [Colour figure can be viewed at wileyonlinelibrary.com]

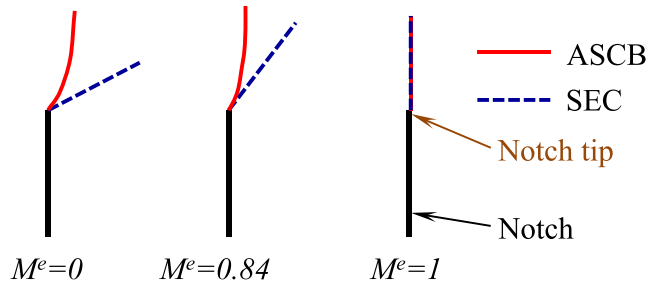

FIGURE 30 Crack propagation paths for mixed-mode I/II fracture (asymmetric semicircular bend [ASCB] and single-edge crack [SEC] specimens)[111,112] [Colour figure can be viewed at wileyonlinelibrary.com]

Mills and Kang[118] used CT specimens (20 mm thick and 50 mm × 50 mm size) made from polystyrene (PS) and a special designed falling mass equipment with 1.85-m/s velocity in order to determine the dynamic fracture toughness. The investigated PS is used for helmet and box lid having the density in the range 20–85 kg/m^3, and some tests were carried on specimens immersed in water for 24 h. They proposed a correlation between dynamic fracture toughness and relative density in the form $K_{ID} = 0.955\,\rho^{1.119}$.

Marsavina and Sadowski[119] investigated the effect of an impregnation layer on dynamic fracture toughness of polyurethane rigid foams. They investigated closed cell rigid PUR foam with 200-kg/m^3 density, manufactured and supplied in the form of flat panels of 12-mm thickness. The foam faces were impregnated with epoxy (layer of 170 μm) and polyester (layer of 100 μm) resin. SENB specimens (12 mm × 12 mm × 60 mm) were adopted with a notch of 1.5 mm (cut with a razor blade), a span of 40 mm was used for the test and the impact load was applied using an instrumented impact hammer. The

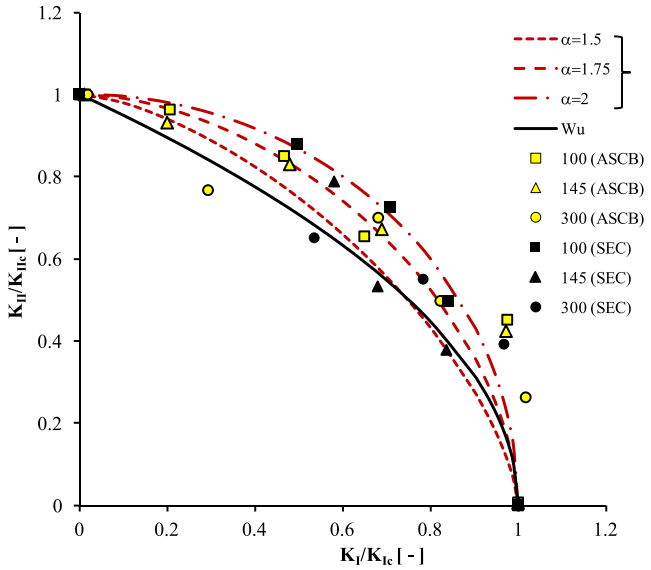

FIGURE 31 Empirical fracture models together with experimental data for PUR foam using asymmetric semicircular bend (ASCB)[75] and single-edge crack (SEC) specimens[109,110] [Colour figure can be viewed at wileyonlinelibrary.com]

mean values of the dynamic fracture toughness for unimpregnated specimens was 0.202 MPa m$^{0.5}$ and approximately 26% higher for the impregnated specimens.

Marsavina et al.[120] presented a correlation between static and dynamic fracture toughness for PUR foams in the density range 40–160 kg/m^3. Single-edge notched specimens (thickness B = 13 mm, width W = 25 mm) under TPB (span S = 100 mm) were used for both static and dynamic tests. The impact tests were carried out using a KB Pruftechnik instrumented pendulum. Linul et al.[96] presented the dynamic fracture toughness for PUR foams of three densities (100, 145 and

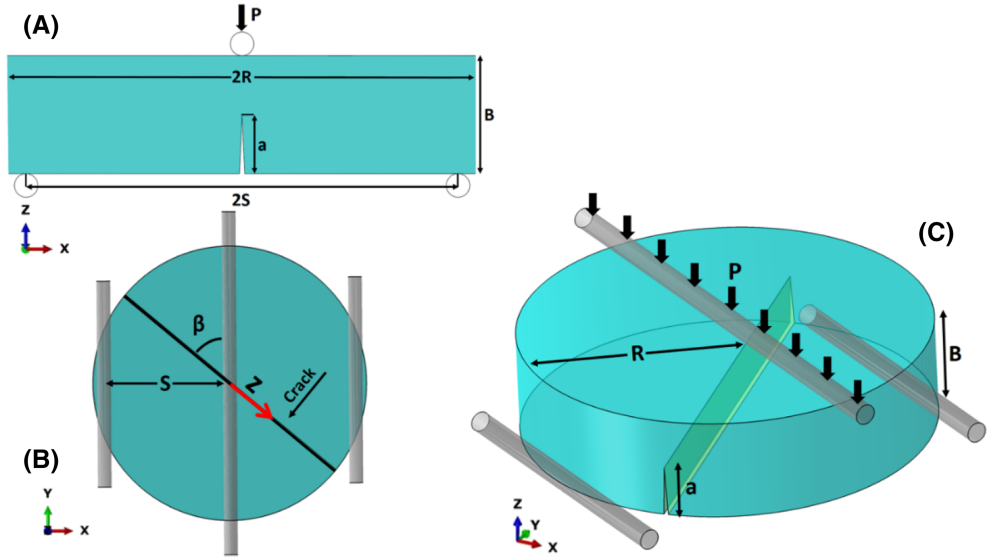

FIGURE 32 Loading configurations of the edge notched disc bend specimen[77] [Colour figure can be viewed at wileyonlinelibrary.com]

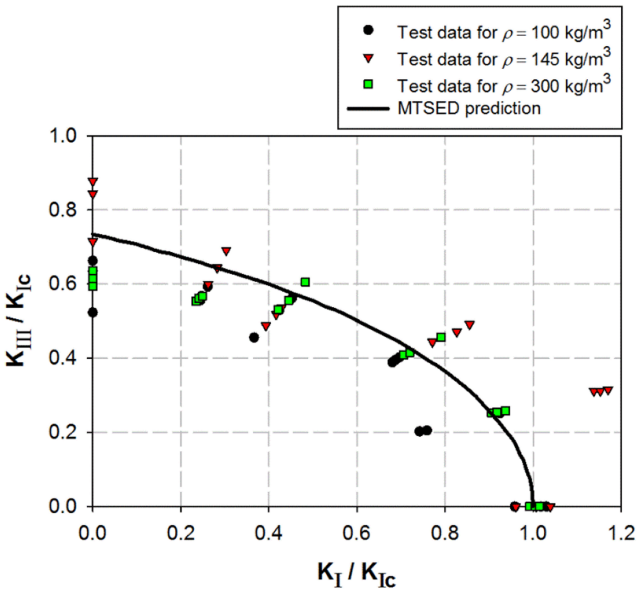

FIGURE 33 Mixed-mode (I + III) fracture results for rigid PUR foams of different densities together with maximum tangential strain energy density (MTSED) criterion[77] [Colour figure can be viewed at wileyonlinelibrary.com]

300 kg/m^3) determined following the same methodology of Marsavina et al.[120]

For each density, the dynamic fracture toughness values are higher than the static fracture toughness values and a linear correlation between K_{IC} and K_{ID} was proposed (Figure 35), valid in the considered density range, which could be useful for estimation of dynamic fracture toughness if static fracture toughness values are available.

7 | IMPROVING FRACTURE TOUGHNESS BY REINFORCING THE FOAMS

Different materials for reinforcement (Rajak et al.[121]) are used to improve the physical and mechanical properties of polymeric foams starting from glass fibre (Serban et al.[122]) or aluminium microfibres (Linul et al.[123,124]) to potato protein (Członka et al.[125]).

Cotgreave and Shortall[126] presented one of the first investigation to improve the fracture toughness of rigid closed cell PUR foam, by reinforcing with CGFs. The incorporation of GFs provides an extension of the natural toughening mechanism, arising from microstructural features that provide for multiple arrests and diversions to occur along the path of a propagating crack. The fibres serve to increase the elastic modulus of the foam and this result in higher fracture toughness values even though the fracture surface energy shows no increase. Some

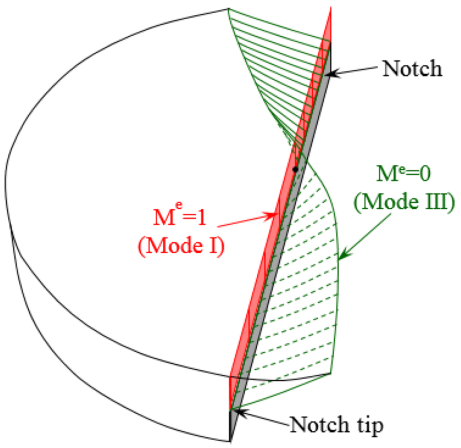

FIGURE 34 Crack propagation paths for mixed-mode I/III fracture (edge-notched disc bend specimens)[117] [Colour figure can be viewed at wileyonlinelibrary.com]

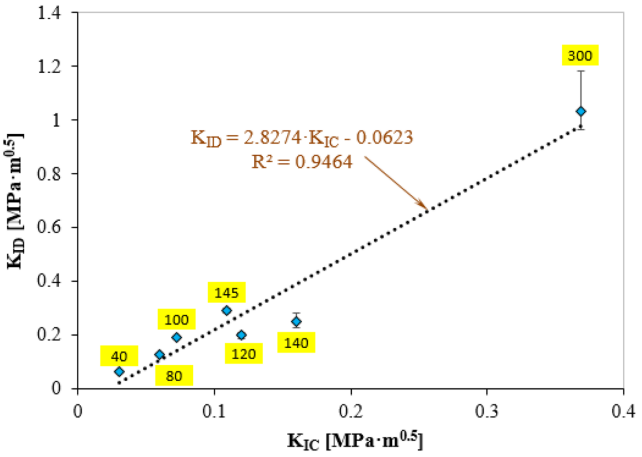

FIGURE 35 Linear correlation between dynamic and static fracture toughness, adapted from Marsavina et al.[120] and Linul et al.[96] [Colour figure can be viewed at wileyonlinelibrary.com]

contribution to the fracture toughness may be attributed to the work required to the extract the unique "pull-out" fragments, Figure 36. The fracture toughness of the composite is directly proportional to the fibre content.

Chen and Gibson[127] investigated foam materials by mixing up to 50% volume fraction of 50 μm diameter hollow glass microspheres (3 M Industrial Specialties Division) with epoxy resin. SENB specimens were tested for fracture toughness determination and the performance indices: $(K_{IC}/\rho, K_{IC})^{2/3}/\rho$ and $(K_{IC})^{1/2}/\rho$ were determined. The fracture toughness decreases from the pure epoxy resin to foam material with 45% volume fraction of spheres. However, the performance indices increased with the increase of hollow sphere volume fractions.

The effect of the fibre content and fibre length on tensile, fracture and thermal properties of syntactic foam

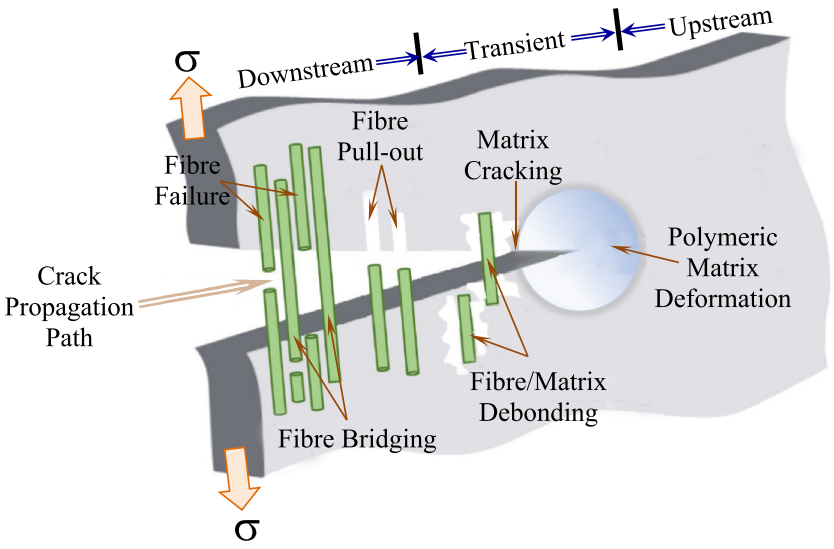

FIGURE 36 Typical failure modes in reinforced polymeric foams and process zone near the crack tip [Colour figure can be viewed at wileyonlinelibrary.com]

was investigated by Wouterson et al.[128] The syntactic foam was produced by mechanical dispersion of 30 vol.% hollow phenolic microspheres (Phenoset BJO-093) as filler in epoxy resin. Short carbon fibre (CF) having 7-μm diameter were used for reinforcement in weight fraction of 1, 2 and 3 wt%. The results showed that a hybrid structure demonstrates a significant increase in the ultimate tensile strength and Young's modulus with increasing fibre volume fraction. Interestingly, the fracture toughness K_{IC} and energy release rate G_{IC} increased by 95% and 90%, respectively, upon introduction of 3 wt% short CFs in syntactic foam, indicating the toughening potential for short CFs in syntactic foam systems. SEM and OM studies identified the presence of several toughening mechanisms. An estimate of the contribution from each toughening mechanism by composite theory and fractography revealed that the specific energy required to create new surfaces was enhanced by the presence of fibres and was the main contributor to the toughness of the short fibre reinforced syntactic foam. However, the variation in fibre length between 3 and 10 mm does not affect the tensile and fracture properties significantly.

Maharsia and Jerro[129] investigated nanoclay hybrid syntactic foams. Four types of hollow glass particles (3 M Corporation) with different densities were used for fabrication. The foams were fabricated with a constant (35%) volume fraction of resin and 65% filler particles. Eight types of nanoclay hybrid foams are made by combining two volume fractions of nanoclay particles (2% and 5%, respectively) with each microballoon type. Results from tensile testing show that strength has increased in all hybrid foams because of the presence of nanoclay particles. Addition of 5% nanoclay results in strength enhancement of between 6% and 22%. Damage tolerance has also increased because of increase in plasticity of matrix because of nanoclay clusters and surfactants on nanoclay particles. It is seen that between 33% and 58% increase in toughness of high-density foams is obtained with the addition of 5% nanoclay particles.

Different microstructures were manufactured using three different types of microspheres, namely, 3 M Scotchlite, TM K15 and K46 glass bubbles and Phenoset BJO-093 hollow phenolic microspheres, and by modifying the volume fractions of microspheres from 0% to 50% volume fraction.[130] The fracture toughness tests were performed using SENB specimens loaded in TPB under quasi-static loading. The fracture toughness and the specific fracture toughness/performance index K_{IC}/ρ increase up to 30 vol% for all types of microspheres and then decrease beyond 30 vol% of filler content. The change in behaviour was attributed to a change in the dominant toughening mechanisms from filler stiffening, crack front bowing to excessive debonding of microspheres in reduced matrix volume.

Wouterson et al.[131] investigated the effect of nanoclay content on tensile and fracture properties of syntactic foam. Results showed that the tensile strength decreased slightly with increasing nanoclay content. The Young's modulus showed an increase of 17% with the addition of 2-wt% clay. Interestingly, the fracture properties reached a maximum for samples containing 1 wt% of nanoclay. SEM and OM studies were performed to identify the toughening mechanisms in nanoclay-reinforced syntactic foam. A comparison of the tensile and fracture results obtained for nanoreinforced syntactic foam against short-fibre reinforced syntactic foam revealed the superiority of micro-reinforcements over nano-reinforcements in improving the tensile properties. Both short microfibres and nanoclay were able to give rise to substantial increase in toughness in polymer syntactic foam.

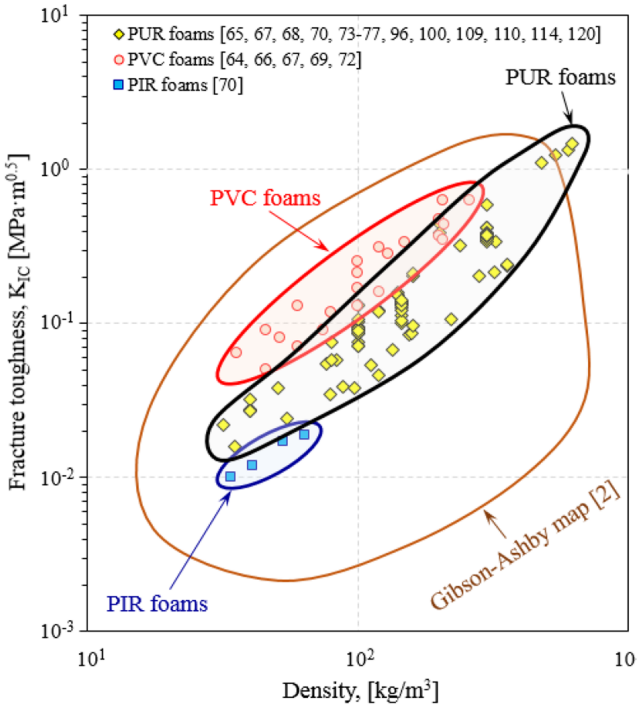

FIGURE 37 Fracture toughness-density chart for families of polymeric foams [Colour figure can be viewed at wileyonlinelibrary.com]

Stewart et al.[132] developed polyurethane foam reinforced with SiC nanoparticles for core in sandwich composites. The functionalization of SiC nanoparticles was performed using a silane-coupling agent to enhance bonding between PU and SiC particles. The SENB specimens loaded in TPB show that the reinforcement of SiC nanoparticles by 1.0 wt% improved the compressive and flexural properties by 50%–70% range. While with the functionalization of SiC particles, an improvement with 200% was observed. The fracture toughness is reduced by SiC reinforcement.

Gómez-Monterde et al.[133] presented an analysis on morphology, mechanical properties and fracture behaviour of solid and foamed plates made of GF-reinforced Polypropylene. The determined fracture parameters were crack tip opening displacement (CTOD) at low strain rate and the fracture toughness (K_{IC}) at impact loading. Foamed specimens presented higher values of CTOD than the solid ones and higher as the foaming ratio increases, because of cells acting as crack arrestors by blunting the crack tip. On the contrary, the fracture toughness K_{IC} decreased with decreasing the apparent density. Because of stress concentration on cell walls, lower density and energy absorption capability, the fracture toughness decreases with approximately 20% for 10% foaming ratio, respectively with 40% for the foaming ratio of 20%. Anisotropy due to fibre orientation was also observed. Fibres were aligned in the filling direction in the surface layers, while they were oriented in the transverse direction in the core. Different properties were obtained with fibres orientation.

Idowu et al.[134] presented a review on three-dimensional graphene foam reinforced polymer matrix composites. Graphene as a filler is being considered to address challenging issues of graphene dispersion and restacking in composite materials because of its three-dimensional interconnected hierarchical structure and its physical–chemical attributes. The stress–strain curve for tensile tests of the graphene foam reinforced polymer matrix composites reveals that the fracture occurs at 45° plane, Nieto et al..[135] The graphene foam reinforced polymer matrix composites allows crack deflection, resulting in enhancement of fracture toughness of the graphene foam-based composite. The same conclusions were observed by Jia et al.[136]

An interesting study on self-healing microvascular polymeric foam for improving the toughness of brittle polyisocyanurate (PIR) foam is presented by Patrick et al.[137] They investigated the healing of brittle PIR foam (Trymer 3000, density 50 kg/m^3) under mode I loading using SENB specimen. The fracture toughness of PIR foam was 0.02 MPa m$^{0.5}$. The healing consists in prefilling of the microvascular channel with the desired healing component and subsequently connecting the open tubing at a wye junction, resulting in a closed system. The expansive nature of the PUR foam reaction provided fast healing, with over 75% recovery in both stiffness and fracture toughness in 1 h at room temperature. The fracture toughness of healed components was 0.018 for horizontal channels, respectively 0.019 MPa·m$^{0.5}$ for vertical channels.

Foam reinforcement was adopted to increase the mechanical and fracture properties of polymeric foams. Glass fibres, CFs, aluminium microfibers, nanoclay particles, SiC nanoparticles and graphene were used to reinforce the foams.

8 | CONCLUDING REMARKS

Efforts in evaluation of the fracture toughness of polymeric foams are clustered around few themes and methodologies. Researches focused on the macroscopic behaviour involving experimental investigations, respectively on the micromechanical aspects of fracture, which are based on analytical and computational analysis.

Analytical and numerical micromechanical models are reviewed and they can successfully be applied to predict the fracture toughness of plastic foams.

However, the fracture toughness values obtained via micromechanical analysis should be experimentally validated.

The analytical micromechanical models estimate the fracture toughness of the foams based on mechanical properties of solid material from cell struts and faces (tensile strength), relative density and some fitting parameters based on cell topology (cell length, strut thickness). There are available models to predict fracture toughness for all fracture modes K_{IC}, K_{IIC} and K_{IIIC}.

The numerical FE micromechanical models allow the investigation of more complex 2D and 3D cellular structures (beams, 2D and 3D solids) with different struts cross sections. The cracks are modelled like broken struts/cells. Usually, the prediction of fracture toughness is based on the applied load, which produce the fracture of the first unbroken strut, and on the LEFM solutions.

At the end of this review, we can conclude that LEFM could be applied for rigid plastic foams. In order to use the LEFM in designing such structures, the fracture toughness of materials should be known, particularly for large structures, if tensile and bending loads are present. Experimental procedure for fracture toughness determination is presented, together with a comprehensive set of experimental results for the fracture toughness.

The fracture toughness of rigid polymeric foams is expressed mainly by K_{IC} and G_{IC}; for flexible foams, the essential work of fracture could be also used.[138]

The experimental results indicate that the fracture toughness does not depend on the specimen shape being a material constant. The density plays the major role on the fracture toughness; this can be observed also in a fracture toughness–density diagram (Figure 37), followed by the solid material contained in the struts and faces.

The foam anisotropy was identified as having different fracture toughness values in the flow and rise direction. This effect is related to the shape of the cells in the two directions and could be quantified considering the cell structure dimensions (strut thickness and cell length). An increase of the fracture toughness was observed at cryogenic temperatures −196°C comparing with those at room temperature.

The investigations on the size effect show that all results are closer to LEFM behaviour. This should be taken into account when design of such structures, because the strength or plasticity criteria are valid only for small structural parts. In the case of large components, the size effect and LEFM should be considered.

The classical fracture criteria, developed for brittle isotropic materials, were applied with success for mixed-mode loading of polymeric foams. The best predictions were obtained for *equivalent stress intensity factor* and for the *maximum energy release rate* criteria for mixed modes I and II, respectively the *maximum tangential strain energy density* criterion for mixed modes I and III.

The dynamic fracture toughness values are higher than the static ones with approximately 2.8 times for all densities between 40 and 300 kg/m^3.

The fracture toughness could be increased by reinforcing the foam with different particles and/or fibres.

ACKNOWLEDGEMENT

This paper was partially funded by the Romanian Ministry of Research and Innovation through projects 10PFE/16.10.2018, PERFORM-TECH-UPT and PN-III-P1-1.2-PCCDI-2017-0391 and by the European Union's Horizon 2020 research and innovation programme under grant agreement no. 857124.

REFERENCES

1. Ashby MF. Cellular solids scaling of proprieties. In: Scheffler M, Colombo P, eds. *Cellular Ceramics: Structure, Manufacturing, Properties and Applications*. Wiley-VCH Verlag Gmbh & Co; 2005:3-16.
2. Gibson LJ, Ashby MF. *Cellular Solids, Structure and Properties*. Second ed. Cambridge University Press; 1997.
3. Mills NJ. *Polymer Foams Handbook*. Butterworth-Heinemann; 2007.
4. Marsavina L. Fracture mechanics of foams. In: Altenbach H, Ochsner A, eds. *Cellular and Porous Materials in Structures and Processes*. Springer; 2010:1-46.
5. Marsavina L, Constantinescu DM. Failure and damage in cellular materials. In: Altenbach H, Sadowski T, eds. *Failure and Damage Analysis of Advanced Materials*. Springer; 2015: 119-190.
6. Grenestedt JL. Effective elastic behavior of some models for perfect cellular solids. *Intern J So Struc*. 1999;36(10):1471-1501.
7. Onck PR, Andrews EW, Gibson LJ. Size effects in ductile cellular solids. Part I: modelling. *Intern J Mecha Sci*. 2001;43: 681-699.
8. Saint-Michel F, Chazeau L, Cavaille J-Y, Chabert E. Mechanical properties of high density polyurethane foams: I. Effect of the density. *Comp Sci and Techn*. 2006;66(15):2700-2708.
9. Christensen RM. A comparison of open cell and closed cell properties for low-density materials. *J Mech of Mate and Struct*. 2007;2(7):1299-1307.
10. Avalle M, Belingardi G, Montanini R. Characterization of polymeric structural foams under compressive impact loading by means of energy-absorption diagram. *Int J Imp Eng*. 2001; 25(5):455-472.
11. Avalle M, Belingardi G, Ibba A. Mechanical models of cellular solids: parameters identification from experimental tests. *Int J of Impact Engineering*. 2007;34(1):3-27.
12. Lagzdins A, Zilaucs A, Beverte I, Andersons J, Cabulis U. A refined strut model for describing the elastic properties of highly porous cellular polymers reinforced with short fibers. *Mech Comp Mate*. 2017;53(3):321-334.
13. Mills NJ, Zhu H. The high strain compression of closed cell polymer foams. *J Mech Phys Solids*. 1999;47(3):669-695.

14. Huang JS, Chow CI. Survival probability for brittle isotropic foams under multiaxial loading. *J Mater Sci*. 2000;35(15):3881-3887.
15. Gupta N, Ricci W. Comparison of compressive properties of layered syntactic foams having gradient in microballoon volume fraction and wall thickness. *Mater Sci Eng A*. 2006;427(1-2):331-342.
16. Alonso IQ, Fleck NA. Damage tolerance of an elastic-brittle diamond-celled honeycomb. *Scr Mater*. 2007;56:693-696.
17. Romijn NER, Fleck NA. The fracture toughness of planar lattices: imperfection sensitivity. *J Mech Phys Solids*. 2007;55(12):2538-2564.
18. Ren XJ, Silberschmidt VV. Numerical modelling of low-density cellular materials. *Comput Mater Sci*. 2008;43:65-74.
19. Pinto H, Amini A, Pena A, Moraga P, Valenzuela M. Fatigue and damage accumulation in open cell aluminium foams. *Fatigue Fract Eng Mater Struct*. 2018;41(2):483-493.
20. Kucherov L, Ryvkin M. Flaw nucleation in a brittle open-cell Kelvin foam. *Int J Fract*. 2012;175(1):79-86.
21. Kucherov L, Ryvkin M. Fracture toughness of open-cell Kelvin foam. *Intern J So Struc*. 2014;51(2):440-448.
22. Fleck NA, Desphande VS, Ashby MF. Micro-architectured materials: past, present and future. *Proc R Soc A*. 2010;466(2121):2495-2516.
23. Ashby MF. The mechanical properties of cellular solids. *Metall Trans A*. 1983;14A:1755-1768.
24. Maiti SK, Ashby MF, Gibson LJ. Fracture toughness of cellular solids. *Scripta Metallur*. 1984;18(3):213-217.
25. Fowlkes CW. Fracture toughness tests of a rigid polyurethane foam. *Intern J Frac*. 1974;10(1):99-108.
26. Mclntyre A, Anderton GE. Fracture properties of a rigid polyurethane foam over a range of densities. *Polymer*. 1979;20(2):247-253.
27. Brezny R, Green DJ. Fracture behavior of open-cell ceramics. *J Amer Ceramic Society*. 1989;72(7):1145-1152.
28. Huang JS, Gibson LJ. Fracture toughness of brittle honeycombs. *Acta Metallurgica et Materialia*. 1991;39(7):1617-1626.
29. Huang JS, Gibson LJ. Fracture toughness of brittle foams. *Acta Metallurgica et Materialia*. 1991;39(7):1627-1636.
30. Green DJ. Fabrication and mechanical properties of lightweight ceramics produced by sintering of hollow spheres. *J. Ame Cer Soc*. 1985;48:403-409.
31. Choi S, Sankar BV. A micromechanical method to predict the fracture toughness of cellular materials. *Intern J So Struc*. 2005;42(5-6):1797-1817.
32. Choi JB, Lakes RS. Fracture toughness of re-entrant foam materials with a negative Poisson's ratio: experiment and analysis. *Int J Fracture*. 1996;80(1):73-83.
33. Fan HL, Fang DN. Enhancement of mechanical properties of hollow-strut foams: analysis. *Mate and De*. 2009;30(5):1659-1666.
34. Chen JY, Huang Y, Ortiz M. Fracture analysis of cellular materials: a strain gradient model. *J Mech Phys Solids*. 1998;26:789-828.
35. Lipperman F, Ryvkin M, Fuchs M. Fracture toughness of two dimensional cellular material with periodic microstructure. *Int J Fracture*. 2007;146(4):279-290.
36. Jelitto H, Schneider GA. A geometric model for the fracture toughness of porous materials. *Acta Mater*. 2018;151:443-453.
37. Jelitto H, Schneider GA. Fracture toughness of porous materials—Experimental methods and data. *Data Brief*. 2019;23:1-12, 103709.
38. Ryvkin M. Analytical solution for a mode III crack in a 3D beam lattice. *Intern J So Struc*. 2012;49(19-20):2839-2847.
39. Huang JS, Lin JY. Mixed-mode fracture of brittle cellular materials. *J Mater Sci*. 1996;31:2647-2652.
40. Srivastava V, Srivastava R. On the polymeric foams: modeling and properties. *J Mater Sci*. 2014;49(7):2681-2692.
41. Jang WY, Kyriakides S, Kraynik AM. On the compressive strength of open-cell metal foams with Kelvin and random cell structures. *Int J Solids Struct*. 2010;47(21):2872-2883.
42. Lu ZX, Liu Q, Huang JX. Analysis of defects on the compressive behaviors of open-cell metal foams through models using the FEM. *Mater Sci Eng A*. 2011;530:285-296.
43. Alkhader M, Vural M. An energy-based an isotropic yield criterion for cellular solids and validation by biaxial FE simulations. *J Mech Phys Solids*. 2009;57(5):871-890.
44. Daxner T. Finite element modelling of cellular materials. In: Altenbach H, Ochsner A, eds. *Cellular and Porous Materials in Structures and Processes*. Springer; 2010:47-106.
45. Ableidinger A. *Some Aspects of the Fracture Behavior of Metal Foams. Diploma Thesis*. Vienna: Vienna University of Technology; 2000.
46. Lee S-J, Wang J, Sankar BV. A micromechanical model for predicting the fracture toughness of functionally graded foams. *Intern J So Struc*. 2007;44(11-12):4053-4067.
47. Arakere NK, Knudsen EC, Wells D, McGill P, Swanson GR. Determination of mixed-mode stress intensity factors, fracture toughness, and crack turning angle for anisotropic foam material. *Intern J So Struc*. 2008;45(18-19):4936-4951.
48. Quintana-Alonso I, Mai SP, Fleck NA, Oakes DCH, Twigg MV. The fracture toughness of a cordierite square lattice. *Acta Mater*. 2010;58(1):201-207.
49. Wang J. *Fracture Toughness of Cellular Materials Using Finite Element Based Micromechanics*. Florida: A dissertation presented to the University of Florida; 2007.
50. Fleck NA, Qiu X. The damage tolerance of elastic-brittle, two dimensional isotropic lattices. *J Mech Phys Solids*. 2007;55(3):562-588.
51. Christodoulou I, Tan PJ. Crack initiation and fracture toughness of random Voronoi honeycombs. *Engin Frac Mech*. 2013;104:140-161.
52. Linul E, Marsavina L. Prediction of fracture toughness for open cell polyurethane foam by finite-element micromechanical analysis. *Iran Polym J*. 2011;20(9):735-746.
53. Murakami Y. *Stress Intensity Factors Handbook*. 1-2 Oxford: Pergamon Press; 1987.
54. Linul E, Serban DA, Marsavina L. Influence of cell topology on mode I fracture toughness of cellular structures. *Physical Mesome*. 2018;21(2):178-186.
55. Thiyagasundaram P, Wang J, Sankar BV, Arakere NK. Fracture toughness of foams with tetrakaidecahedral unit cells using finite element based micromechanics. *Engin Frac Mech*. 2011;78(6):1277-1288.
56. Settgast C, Abendroth M, Kuna M. Fracture mechanical analysis of open cell ceramic foams under multi-axial mechanical loading. *Arch Appl Mech*. 2016;86(1-2):335-349.

57. Rizov V, Mladensky A. Fracture behavior of HT-90 structural foam—A three-dimensional analysis. *Mate and De*. 2009; 30(3):617-621.
58. Landrock AH. *Handbook of Plastic Foams. Types, Properties, Manufacture and Applications*. Park Ridge: Noyes Publications; 1995.
59. Brown R. *Handbook of Polymer Testing: Physical Methods*. New York: Marcel Dekker Inc.; 1999.
60. Brown R. *Handbook of Polymer Testing*. Shawbury: Rapra Technology; 2002.
61. Ward IM, Sweeney J. *An Introduction to the Mechanical Properties of Solid Polymers*. 2nd ed. Chichester: John Wiley and Sons; 2004.
62. Park KB, Kim HT, Her NY, Lee JM. Variation of mechanical characteristics of polyurethane foam: effect of test method. *Dent Mater*. 2019;12(17):1-20, 2672.
63. ASTM. D5045-99: Standard Test Methods for Plane-Strain Fracture Toughness and Strain Energy Release Rate of Plastic Materials, 1999.
64. Poapongsakorn P, Carlsson LA. Fracture toughness of closed-cell PVC foam: effects of loading configuration and cell size. *Composite Struct*. 2013;102:1-8.
65. McIntyre A, Anderton GE. Fracture properties of a rigid PU foam over a range of densities. *Polymer*. 1979;20(2):247-253.
66. Viana GM, Carlsson LA. Mechanical properties and fracture characterisation of cross-linked PVC foams. *J Sanh Struc and Mate*. 2002;4:91-113.
67. Kabir ME, Saha MC, Jeelani S. Tensile and fracture behavior of polymer foams. *Mater Sci Eng A*. 2006;429(1-2):225-235.
68. Marsavina L, Linul E, Fracture toughness of polyurethane foams. Experiments versus micromechanical models, Proceedings of the 18th European Conference on Fracture, Dresden, Germany, 2010.
69. Burman M, Fatigue crack initiation and propagation in sandwich structures, Report No.98–29, Stockholm, 1998.
70. Andersons J, Cabulis U, Stiebra L, Kirpluks M, Sparniņš E. Modeling the mode I fracture toughness of anisotropic low-density rigid PUR and PIR foams. *Int J Fract*. 2017;205(1): 111-118.
71. Jin H, Lu W-Y, Scheffel S, Hinnerichs TD, Neilsen MK. Full-field characterization of mechanical behavior of polyurethane foams. *Intern J So Struc*. 2007;44(21):6930-6944.
72. Kidane A. On the failure and fracture of polymer foam containing discontinuities. *ISRN Materials Science*. 2013;408596. https://doi.org/10.1155/2013/408596
73. Apostol DA, Stuparu F, Constantinescu DM, Marsavina L, Linul E. Crack length influence on stress intensity factors for the asymmetric four-point bending testing of a polyurethane foam. *Materiale Plastice*. 2016;53(2):280-282.
74. Apostol DA, Constantinescu DM, Marsavina L, Linul E. Particularities of the asymmetric four-point bending testing of polyurethane foams. *UPB Sci Bull, Series D*. 2016;78(2):57-66.
75. Marsavina L, Constantinescu DM, Linul E, Apostol DA, Voiconi T, Sadowski T. Refinements on fracture toughness of PUR foams. *Engin Frac Mech*. 2014;129:54-66.
76. Marsavina L, Constantinescu DM, Linul E, Voiconi T, Apostol DA. Shear and mode II fracture of PUR foams. *Engin Fai Analy*. 2015;58:465-476.
77. Aliha MRM, Linul E, Bahmani A, Marsavina L. Experimental and theoretical fracture toughness investigation of PUR foams under mixed mode I+III loading. *Polymer Testing*. 2018;67: 75-83.
78. Bureau MN, Kumar V. Fracture toughness of high density polycarbonate microcellular foams. *J Cellular Plas*. 2006;42(3): 229-240.
79. Saenz EE, A., Carlsson LA, Karlsson A. Characterization of fracture toughness (Gc) of PVC and PES foams. *J Mater Sci*. 2011;46(9):3207-3215.
80. Matteson RC, Carlsson LA, Aviles F, Loup DC. On crack extension in foamed cored sandwich fracture specimens. In: Thomsen OT et al., eds. *Sandwich Structures 7: Advancing with Sandwich Structures and Materials*. Springer; 2005: 121-130.
81. Shivakumar K, Chen H, Bhargava A. Effect of geometric constraint on fracture toughness of PVC foam core sandwich beams. In: Thomsen OT et al., eds. *Sandwich Structures 7: Advancing with Sandwich Structures and Materials*. Springer; 2005:131-142.
82. Saenz EE, Carlsson LA, Karlsson AM. In situ analysis of crack propagation in polymer foams. *J Mater Sci*. 2011;46:5487-5494.
83. Saenz EE, Carlsson LA, Karlsson AM. In situ analysis of fatigue crack propagation in polymer foams. *Engin Frac Mech*. 2013;101:23-32.
84. Huber AT, Gibson LJ. Anisotropy of foams. *J Mater Sci*. 1988; 23(8):3031-3040.
85. Ganpatye AS, Kinra VK. Fracture toughness of space shuttle external tank insulation foam. In: 47th AIAA/ASME/ASCE/-AHS/ASC Structures, Structural Dynamics, and Materials Conference, Newport, Rhode Island, 2006.
86. Arvidson JM, Sparks LL. Low temperature mechanical properties of a polyurethane foam. National Bureau of Standards, U.S. Department of Commerce, Colorado 80303, 1981.
87. Farshidi A, Berggreen C, Carlsson LA. Low temperature mixed-mode debond fracture and fatigue characterisation of foam core sandwich. *J Sandw Struct Mater*. 2018;22(4):1039-1054. https://doi.org/10.1177/1099636218779420
88. Demharter A. Polyurethane rigid foam, a proven thermal insulating material for applications between +130°C and −196°C. *Cryogenics*. 1998;38(1):113-117.
89. Yakushin VA, Zhmud NP, Stirna UK. Physicomechanical characteristics of spray-on rigid polyurethane foams at normal and low temperatures. *Mech Compos Mater*. 2002;38(3): 273-280.
90. Stirna U, Beverte I, Yakushin V, Cabulis U. Mechanical properties of rigid polyurethane foams at room and cryogenic temperatures. *J Cell Plast*. 2011;47(4):337-355.
91. Denay AG, Castagnet S, Roy A, Alise G, Thenard N. Compression behavior of glass-fiber-reinforced and pure polyurethane foams at negative temperatures down to cryogenic ones. *J Cell Plast*. 2013;49(3):209-222.
92. Yakushin V, Cabulis U, Sevastyanova I. Effect of filler type on the properties of rigid polyurethane foams at a cryogenic temperature. *Mech Compos Mater*. 2015;51(4):447-454.
93. Knudsen E, Anisotropic fracture analysis of the BX-265 foam insulation material under mixed-mode loading, PhD Thesis, University of Florida, 2006.

94. Yu YH, Choi I, Nam S, Lee DG. Cryogenic characteristics of chopped glass fiber reinforced polyurethane foam. *Compos Struct*. 2014;107:476-481.
95. Fu SY, Lauke B. Effect of fiber length and fiber orientation distributions on the tensile strength of short fiber reinforced polymers. *Compos Sci Technol*. 1996;56(10):1179-1190.
96. Linul E, Marşavina L, Vălean C, Bănică R. Static and dynamic mode I fracture toughness of rigid PUR foams under room and cryogenic temperatures. *Eng Fract Mech*. 2020;225:1-10, 106274.
97. Bažant ZP. *Scaling of Structural Strength*. London: Hermes-Penton; 2002.
98. Bažant ZP, Yong Z, Goangseup Z, Isaac MD. Size effect and asymptotic matching analysis of fracture of closed-cell polymeric foam. *I J Solis Struct*. 2003;40:7197-7217.
99. Bažant ZP. Size effect in blunt fracture: concrete, rock, metal. *J Engin Mecha ASCE*. 1984;110(4):518-535.
100. Linul E, Marsavina L, Sadowski T, Kneć M. Size effect on fracture toughness of rigid polyurethane foams. *Solid State Pheno*. 2012;188:205-210.
101. Touliatou D, Wheel MA. K-dominance and size effect in mode I fracture of brittle materials with low to medium porosity. *Engin Frac Mech*. 2018;201:269-281.
102. Erdogan F, Sih GC. On the crack extension in plates under plane loading and transverse shear. *J Basic Engn*. 1963;85(4): 519-525.
103. Sih GC. Strain-energy-density factor applied to mixed mode crack problems. *I J Fract*. 1974;10(3):305-321.
104. Hussain MA, Pu SL, Underwood J, Strain energy release rate for a crack under combined mode I and mode II. In: Paris PC, Irwin GR, Editors, Fracture analysis, ASTM STP560, Philadelphia, 1974, 2–28.
105. Richard HA. *Bruchvorhersagen bei ueberlagerter Normal- und Schubbeanspruchung von Rissen*. Dusseldorf: VDI-Verlag; 1985.
106. Richard HA, Fulland M, Sander M. Theoretical crack path prediction. *Fatigue Fract Eng Mater Struct*. 2005;28(1-2):3-12.
107. Hallstrom S, Grenestedt JL. Mixed mode fracture of cracks and wedge shaped notches in expanded PVC foam. *I J Fract*. 1997;88(4):343-358.
108. Noury PM, Shenoi RA, Sinclair I. On mixed-mode fracture of PVC foam. *I J Fract*. 1998;92(2):131-151.
109. Linul E, Voiconi T, Marsavina L. Determination of mixed mode fracture toughness of PUR foams. *Struct Integ and Life*. 2014;14(2):87-92.
110. Linul E, Marsavina L. Experimental determination of mixed-mode fracture toughness for rigid polyurethane foams. In: Pluvinage G, Milovic L, eds. *Fracture at all Scales. Lecture Notes in Mechanical Engineering*. Springer; 2016:221-237.
111. Apostol DA, Constantinescu DM, Marsavina L, Linul E. Mixed-mode testing for an asymmetric four-point bending configuration of polyurethane foams. *Appl Mech Mater*. 2015; 760:239-244.
112. Marsavina L, Linul E, Voiconi T, Constantinescu DM, Apostol DA. On the crack path under mixed mode loading on PUR foams. *Frattura Ed Integrita Strutturale*. 2015;34:444-453.
113. Marsavina L, Constantinescu DM, Linul E, Stuparu FA, Apostol DA. Experimental and numerical crack paths in PUR foams. *Engin Frac Mech*. 2016;167:68-83.
114. Apostol DA, Stuparu F, Constantinescu DM, Marsavina L, Linul E. Experimental and XFEM analysis of mode II propagating crack in a polyurethane foam. *Materiale Plastice*. 2016; 53(4):685-688.
115. Lim IL, Johnston IW, Choi SK, Boland JN. Fracture testing of a soft rock with semi-circular specimens under three-point bending. Part 2—mixed-mode. *Int J Rock Mech Min Sci & Geomech Abstr*. 1994;31(3):199-212.
116. Wu EM. Application of fracture mechanics to anisotropic plates. *ASME J Appl Mech*. 1967;34(4):967-974.
117. Aliha MRM, Mousavi SS, Bahmani A, Linul E, Marsavina L. Crack initiation angles and propagation paths in polyurethane foams under mixed modes I/II and I/III loading. *Theore and Appl Frac Mecha*. 2019;101:152-161.
118. Mills NJ, Kang P. The effect of water immersion on the mechanical properties of polystyrene bead foam used in soft Shell cycle helmets. *J Cellular Plas*. 1994;30(3):196-222.
119. Marsavina L, Sadowski T. Dynamic fracture toughness of polyurethane foam. *Polymer Testing*. 2008;27(8):941-944.
120. Marsavina L, Linul E, Voiconi T, Sadowski T. A comparison between dynamic and static fracture toughness of polyurethane foams. *Polymer Testing*. 2013;32(4):673-680.
121. Rajak DK, Pagar DD, Menezes PL, Linul E. Fiber-reinforced polymer composites: manufacturing, properties, and applications. *Polymers*. 2019;11(10):1667.
122. Serban DA, Weissenborn O, Geller S, Marsavina L, Gude M. Evaluation of the mechanical and morphological properties of long fibre reinforced polyurethane rigid foams. *Polymer Testing*. 2016;49:121-127.
123. Linul E, Vălean C, Linul PA. Compressive behavior of aluminum microfibers reinforced semi-rigid polyurethane foams. *Polymers*. 2018;10(12):1298.
124. Linul E, Linul PA, Valean C, Marsavina L, Silaghi-Perju D. Manufacturing and compressive mechanical behavior of reinforced polyurethane flexible (PUF) foams. *IOP Conf Series: Mate Sci and Engin*. 2018;416:012053.
125. Członka S, Bertino MF, Strzelec K. Rigid polyurethane foams reinforced with industrial potato protein. *Polymer Testing*. 2018;68:135-145.
126. Cotgreave T, Shortall JB. The fracture toughness of reinforced polyurethane foam. *J Mater Sci*. 1978;13(4):722-730.
127. Chen CP, Gibson LJ. Fracture toughness performance indices for microsandwich foams. *J Mater Sci Lett*. 1995;14(9):665-667.
128. Wouterson EM, Boey FYC, Hu X, Wong S-C. Effect of fiber reinforcement on the tensile, fracture and thermal properties of syntactic foam. *Polymer*. 2007;48(11):3183-3191.
129. Maharsia RR, Jerro HD. Enhancing tensile strength and toughness in syntactic foams through nanoclay reinforcement. *Mater Sci Eng A*. 2007;454–455:416-422.
130. Wouterson EM, Boey FYC, Hu X, Wong S-C. Specific properties and fracture toughness of syntactic foam: effect of foam microstructures. *Composites Sci and Tech*. 2005;65(11-12): 1840-1850.
131. Wouterson EM, Boey FYC, Wong S-C, Chen L, Hu X. Nano-toughening versus micro-toughening of polymer syntactic foams. *Composites Sci and Tech*. 2007;67(14):2924-2933.
132. Stewart JK, Mahfuz H, Carlsson LA. Enhancing mechanical and fracture properties of sandwich composites using nanoparticle reinforcement. *J Mater Sci*. 2010;45(13):3490-3496.

133. Gómez-Monterde J, Sánchez-Soto M, Maspoch L. Microcellular PP/GF composites: morphological, mechanical and fracture characterization. *Composites: Part A*. 2018;104:1-13.
134. Idowu A, Boesl B, Agarwal A. 3D graphene foam-reinforced polymer composites. *A Review, Carbon*. 2018;135:52-71.
135. Nieto A, Boesl B, Agarwal A. Multi-scale intrinsic deformation mechanisms of 3D graphene foam. *Carbon*. 2015;85:299-308.
136. Jia J, Sun X, Lin X, Shen X, Mai YW, Kim JK. Exceptional electrical conductivity and fracture resistance of 3D interconnected graphene foam/epoxy composites. *ACS Nano*. 2014;8(6):5774-5783.
137. Patrick JF, Sottos NR, White SR. Microvascular based self-healing polymeric foam. *Polymer*. 2012;53(19):4231-4240.
138. Arencón D, Antunes M, Martínez AB, Velasco JI. Study of the fracture behavior of flexible polypropylene foams using the essential work of fracture (EWF). *Polymer Testing*. 2012;31(2):217-225.

How to cite this article: Marşavina L, Linul E. Fracture toughness of rigid polymeric foams: A review. *Fatigue Fract Eng Mater Struct*. 2020;1–32. https://doi.org/10.1111/ffe.13327

materials

MDPI

Article

Is Fracture Toughness of PUR Foams a Material Property? A Statistical Approach

Adrian Pugna [1], Romeo Negrea [2], Emanoil Linul [3] and Liviu Marsavina [3,*]

[1] Department of Management, University Politehnica Timisoara, Blvd. M. Viteazu, No. 1, 300222 Timisoara, Romania; adrian.pugna@upt.ro
[2] Department of Mathematics, University Politehnica Timisoara, Pta. Victoriei, No. 2, 300006 Timisoara, Romania; romeo.negrea@upt.ro
[3] Department of Mechanics and Strength of Materials, University Politehnica Timisoara, Blvd. M. Viteazu, No. 1, 300222 Timisoara, Romania; emanoil.linul@upt.ro
* Correspondence: liviu.marsavina@upt.ro; Tel.: +40-256-403577

Received: 4 October 2020; Accepted: 27 October 2020; Published: 30 October 2020

Abstract: The published data on the experimentally determined fracture toughness of foams are based on a small number of specimens, having a lack of statistical consistency. The paper proposes a statistical approach on the fracture toughness results of rigid polyurethane (PUR) foams of three different densities. Five types of fracture tests were considered. The results were statistically analyzed using six types of regressions and a meta-analysis to identify the factors influencing the fracture toughness. The statistical analysis indicates that the fracture toughness represents a material property because does not depend on the specimen type. The density plays a major role in the fracture toughness of PUR foams. The irregular shape of the cells induced small anisotropy for low-density foams (100 kg/m^3 and 145 kg/m^3). This effect could not be observed for the foam with 300 kg/m^3 density, for which the cells have a more regular spherical shape. The statistical analysis indicates that the influence of the loading speed is very weak.

Keywords: polyurethane foam; fracture toughness; density; anisotropy; statistical approach

1. Introduction

For structural components, strength and fracture toughness are two important mechanical properties [1,2]. Yield strength is the measure of the stress that a material can withstand before plastic deformation, while the tensile strength is a measure of the maximum stress that a material can support before starting to fracture [3]. Fracture toughness is a measure of the energy required to fracture a material that contains a crack [4]. The relationship between fracture toughness and strength could be seen in a material selection diagram (Figure 1) [5].

It could be observed that foam materials are placed at the bottom left, corresponding with low fracture toughness (tenths of MPa·m$^{0.5}$) and relatively low strength (up to 10 MPa).

In structural integrity applications, the fracture toughness represents a key material parameter, which plays an important role [6]. To measure fracture toughness of metals, extensive efforts have been made to develop reliable fracture toughness test methods since the 1960s. However, for polymeric materials, only the standard ASTM D5045–14 [7] describes the methodology to determine the plane-strain fracture toughness and strain energy release rate of plastic materials. Up to now, there are no standards for the determination of fracture toughness of cellular materials and plastic foams. However, often the methodology proposed in [7] was adopted for determination of fracture toughness of polymeric foams, considering Single Edge Notched Specimens loaded in Three-Point Bending [8–10], respectively Compact Tension specimens [11].

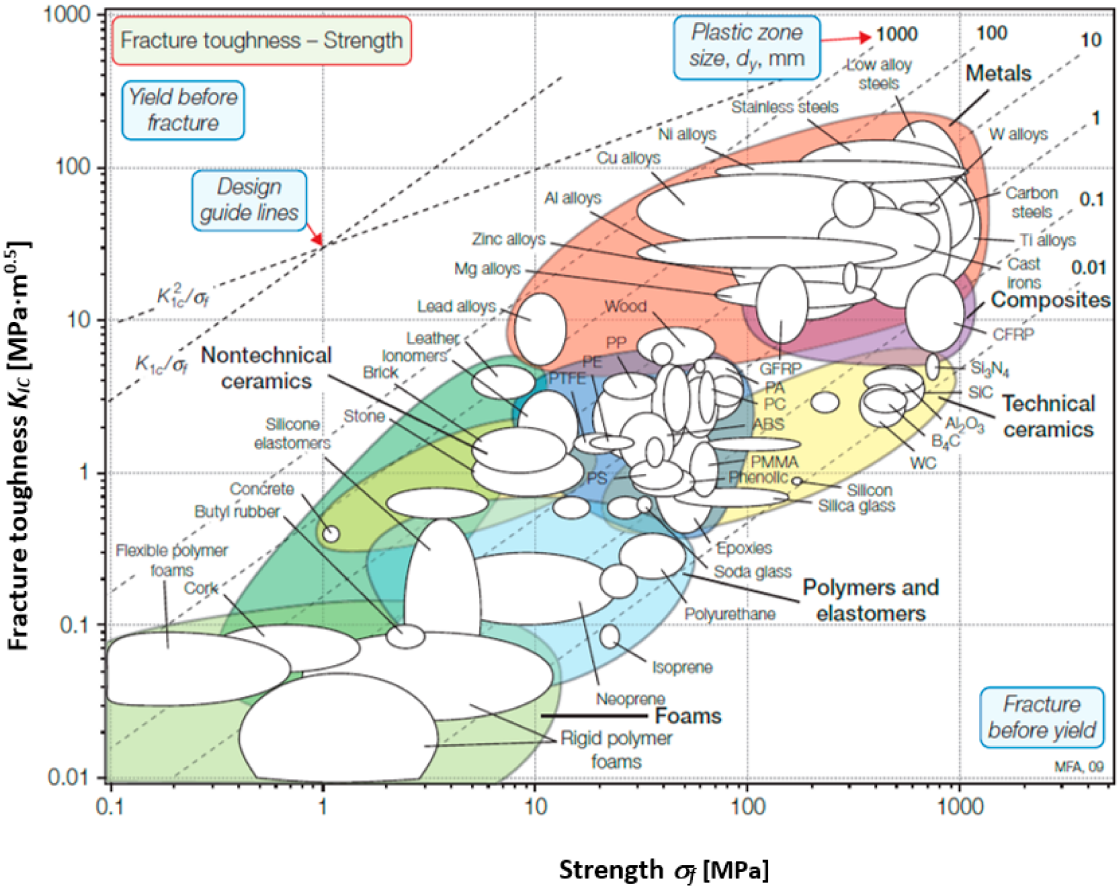

Figure 1. Fracture toughness versus strength [5].

Jelitto and Schneider [12] revised the experimental methods and the fracture toughness data of porous materials including PUR foams, respectively Marsavina and Linul [13] presented a review of the fracture of polymeric foams.

It is also well known that the plastic foams have an elastic-plastic behavior in compression with a long plateau and a densification region Figure 2a [14,15], but a quasi-brittle behavior under tensile and in the presence of notches, cracks, Figure 2b, [16,17].

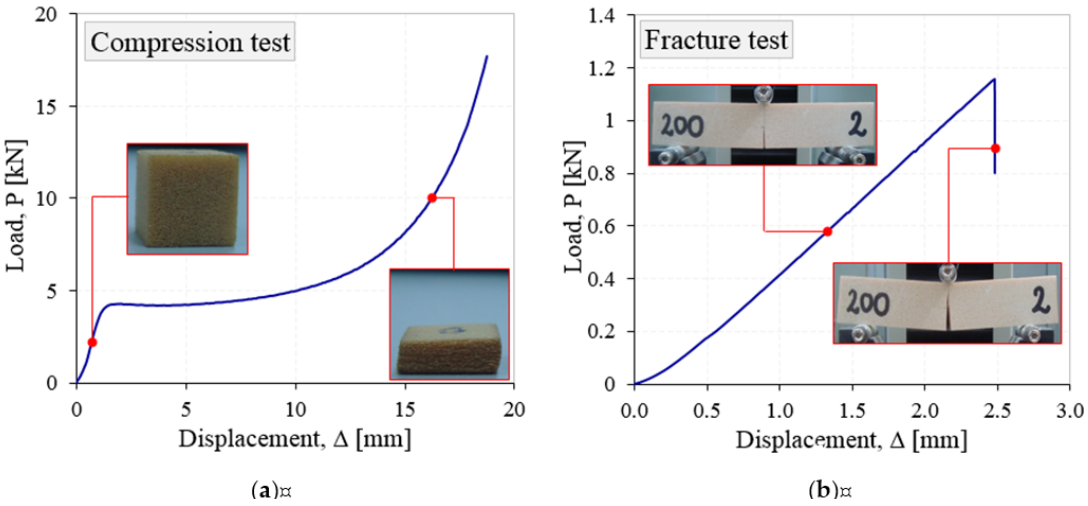

(**a**)¤ (**b**)¤

Figure 2. Load–displacement curves after compression (**a**) and three-point bending (**b**) tests.

A limited number of works provide the fracture toughness of polyurethane (PUR) foams. Fowlkes [18] performed one of the first experimental investigation on fracture toughness of PUR foams with a density of 88 kg/m^3, considering Middle Cracked, Double Edge Crack, Single Edge Crack and Double Cantilever Beam specimens. The fracture toughness was expressed by the critical energy release rate G_{IC} and show that the fracture toughness results does not depend on specimen type. McIntyre and Anderton [8] presented the fracture toughness of PUR rigid foams in the density range 32–360 kg/m^3. The tests were performed using Single Edge Notched Bend (SENB) specimens loaded in three-point bending. The obtained fracture toughness results range between 0.01 MPa·m$^{0.5}$ for the lowest density foam, to 0.243 MPa·m$^{0.5}$ for highest density foam. Kabir et al. [10] compared the fracture toughness of PUR and PVC foams with a density of 260 kg/m^3, observing that the value of the fracture toughness for PVC is 2.2 times higher than the PUR one, and this is due to the higher toughness of the solid material from the cell walls.

Marsavina and Linul [19] experimentally investigated closed-cell rigid PUR foams with densities between 40 kg/m^3 and 200 kg/m^3 using SENB specimens loaded in three-point bending and determined the mode I fracture toughness between 0.034–0.39 MPa·m$^{0.5}$. Fracture toughness of low-density rigid PUR (32–84 kg/m^3) was obtained by Andersons et al. [11] in the range 0.022–0.058 MPa·m$^{0.5}$ using Compact Tension (CT) specimens.

Poapongsakorn and Carlsson [20] using SENB specimens made of PVC foam showed that symmetric four point bending loading give a fracture toughness two times higher comparing with loading in three point bend configuration, due to indentation which occurs in the cracked cross section area, reducing the ligament size.

Based on the experimental data, respectively on micromechanical modeling different authors expresses the fracture toughness of foams to the relative density of the foam (ρ_f/ρ_s), the dimension of the cell l, and tensile strength of the solid material, which forms the foam σ_{fs} in the form:

$$K_{IC} = C\sigma_{fs}\sqrt{\pi\, l}\left(\frac{\rho_f}{\rho_s}\right)^m \left[\text{MPa·m}^{0.5}\right] \quad (1)$$

with C a fitting constant, usually obtained by interrogating the experimental data.

Maiti et al. [21] proposed for the exponent m values of 1.5 for open cells, respectively 2 for closed-cell foams and for C a value of 0.65. Green [22] using an elastic model in shell theory of the hollow sphere found C = 0.28 and m = 1.3, while Choi and Sankar [23] taking into account the crack blunting and the non-singular stress field ahead of the crack tip proposed C = 0.19 and m = 1.

However, all these models are determined usually on few experimental data having a lack of statistical consistency. In this regard, present paper proposes a statistical approach to the fracture toughness of rigid PUR foams. In the following section (Section 2), the investigated materials and experimental methodology are presented. Section 3 presents the influence of density, type of specimen, orientation and loading seed on the fracture toughness of PUR foams and is followed by the statistical assessment (Section 4).

2. Materials and Methods

Polyurethane (PUR) foams of three different densities (100 kg/m^3, 145 kg/m^3, and 300 kg/m^3) were considered. The foams were produced by Necumer GbmH (Bohmte, Germany) under trade name NECURON 100, 160, and 301. Their microstructure is shown in Figure 3. The images were obtained with SEM QUANTATM FEG 250 (Hillsboro, OR, USA) at 1000× magnification.

The mode I fracture toughness tests were performed on different specimens: Single Edge Notch Bend (SENB) loaded in three (3PB) and four-point bending (4PB), Figure 4a,b, Single Edge Crack (SEC), Figure 4c, Semi-Circular Bend Specimen (SCB), Figure 4d, and Edge Notch Bend Disc (ENDB), Figure 4e. The specimens were cut in the flow and rise direction to study the foam anisotropy, but this

was not possible for all types of specimens because the thickness of the foam plates was 50 mm for densities of 100 kg/m^3 and 145 kg/m^3, respectively 25 mm for the foam with 300 kg/m^3 density.

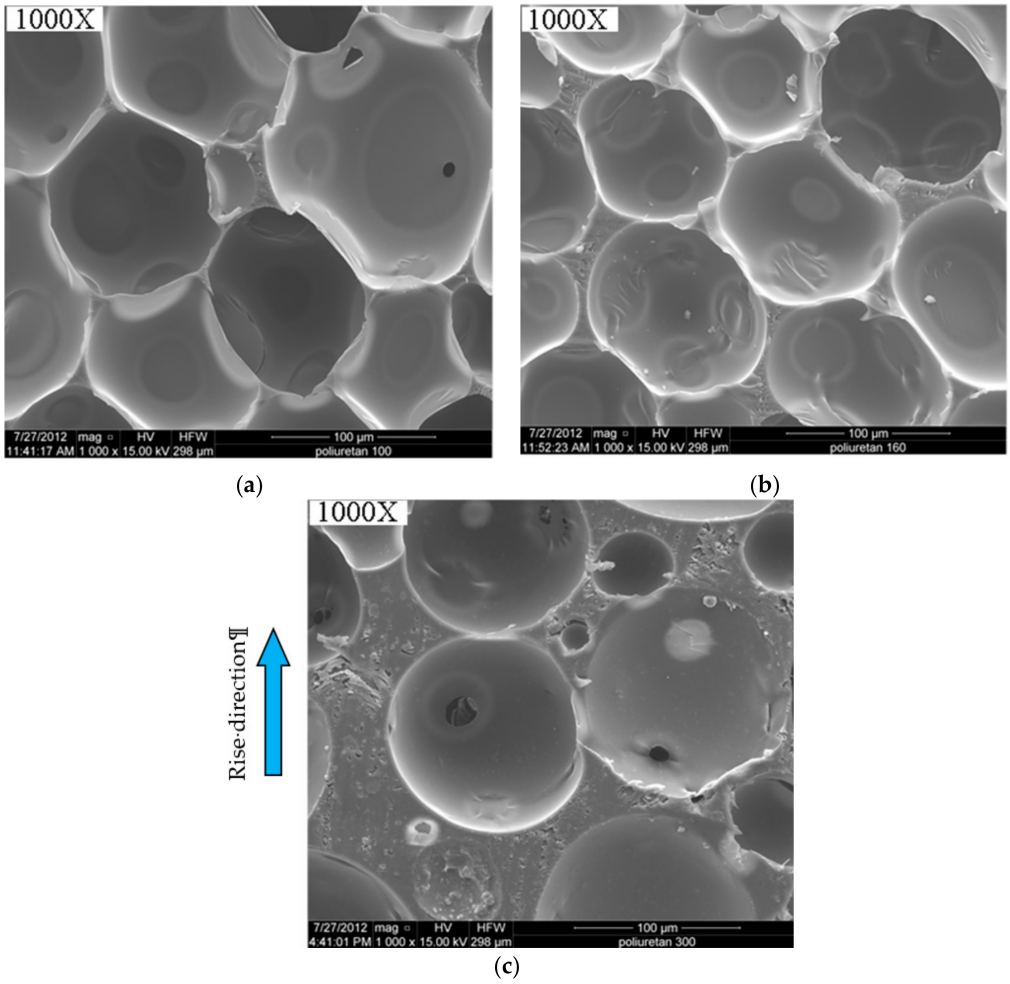

Figure 3. Microstructures of the investigated foams for 100 (**a**); 145 (**b**) and 300 (**c**) kg/m^3.

Tests were carried out at room temperature with a loading speed of 2 and 50 mm/min using a ZWICK Z005 Proline (Ulm, Germany) universal testing machine.

The mode I fracture toughness values were determined with the maximum load P_{max} from load–displacement curves, recorded during the experimental tests. Furthermore, the appropriate relationships, taking into account the geometry and dimensions of the specimens, were considered, Table 1.

Table 1. Fracture toughness calculation.

Specimen Type	Calculation of K_{IC}	Reference
SENB loaded in 3PB	$K_{IC} = \frac{3P_{\max}S}{2BW^2} f_I(a/W)$	[7]
SENB loaded in 4PB	$K_{IC} = \frac{3P_{\max}}{BW} g_I(a/W)$	[24,25]
SEC	$K_{IC} = \frac{p_{\max}}{W\,t} \sqrt{\pi a}\, h_I(\beta\,,\, a/W)$	[26]
SCB	$K_{IC} = \frac{P_{\max}}{2Rt} \sqrt{\pi a}\, j_I(a/R,\, S_1/R,\, S_2/R)$	[27]
ENBD	$K_{IC} = \frac{6P_{\max}S}{RB^2} k_I(a/B, S/R, \beta)$	[28]

The non-dimensional functions $f_I(a/W)$, $g_I(a/W)$, $h_I(\beta, a/W)$, $j_I(a/R, S_1/R, S_2/R)$, $k_I(a/B, S/R, \beta)$ are provided in the literature [7,24–28].

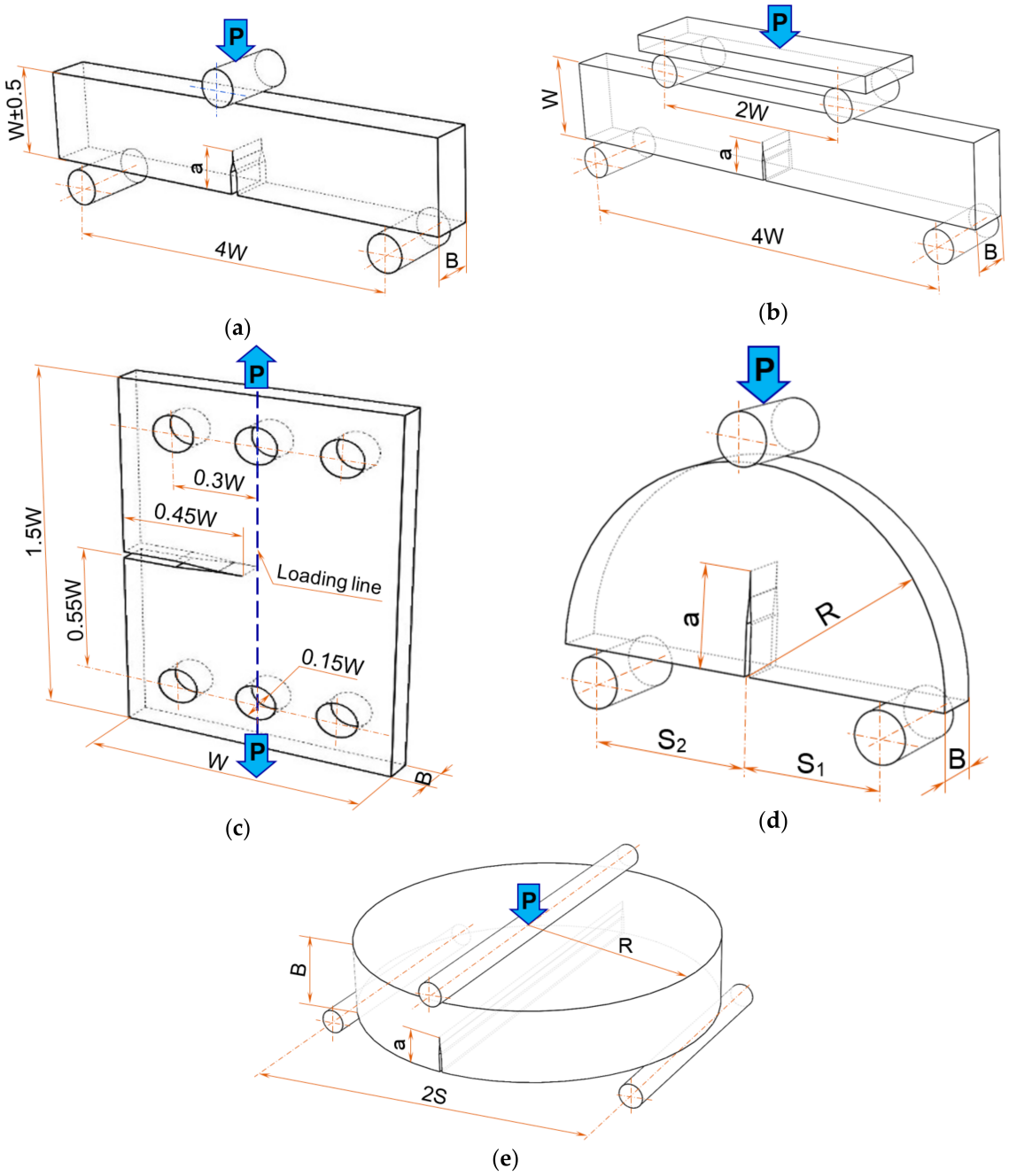

Figure 4. The geometry of the specimens and loading configuration of the fracture toughness tests: (**a**) Single Edge Notch Bend (SENB) specimen loaded in three point bending (B = 12.5 mm, W = 25 mm, a = 12.5 mm); (**b**) SENB specimen loaded in four point bending (B = 11.5 mm, W = 25 mm, a = 16.5 mm); (**c**) Single Edge Crack (SEC) specimen (B = 8 mm, W = 75 mm, a = 33.75 mm); (**d**) Symmetric Semi Circular Bend (SCB) specimen (R = 40 mm, B = 10 mm, S_1 = S_2 = 30 mm, a = 20 mm); (**e**) Edge Notch Bend Disc (ENDB) specimen (R = 75 mm, B = 30 mm, a = 15 mm).

3. Experimental Results

The fracture toughness results for the three investigated foams are presented in Tables 2–4. It could be observed that the average values for the 100 kg/m^3 density PUR foam were between 0.071–0.091 MPa·m$^{0.5}$ in the flow direction, respectively up to 0.106 MPa·m$^{0.5}$ in the rise direction.

Table 2. Fracture toughness results for 100 kg/m^3 polyurethane (PUR) foam density.

Specimen Type	Loading Direction	Loading Speed [mm/min]	Fracture Toughness [MPa·m$^{0.5}$]					
			1	2	3	4	5	Average
SENB-TPB	Flow	2	0.072	0.074	0.075	0.068	–	0.072
SENB-TPB	Rise	2	0.070	0.082	0.078	0.076	–	0.076
SENB-FPB	Flow	2	0.072	0.071	0.070	0.073	0.071	0.071
SEC	Flow	2	0.083	0.090	0.079	0.100	–	0.088
SCB	Flow	2	0.084	0.088	0.090	–	–	0.087
SCB	Flow	50	0.074	0.105	0.095	–	–	0.091
SCB	Rise	2	0.109	0.099	0.116	0.102	–	0.106
SCB	Rise	50	0.089	0.095	–	–	–	0.092
ENDB	Rise	2	0.094	0.093	0.087	–	–	0.091

Table 3. Fracture toughness results for 145 kg/m^3 PUR foam density.

Specimen Type	Loading Direction	Loading Speed [mm/min]	Fracture Toughness [MPa·m$^{0.5}$]						
			1	2	3	4	5	6	Average
SENB-TPB	Flow	2	0.102	0.105	0.099	0.107	0.119	0.124	0.109
SENB-TPB	Rise	2	0.110	0.111	0.109	0.111	0.128	0.125	0.116
SENB-FPB	Flow	2	0.091	0.092	0.099	0.093	0.102	–	0.095
SEC	Flow	2	0.124	0.100	0.128	0.106	0.084	–	0.109
SCB	Flow	2	0.135	0.134	0.129	0.129	–	–	0.132
SCB	Flow	50	0.128	0.136	–	–	–	–	0.132
SCB	Rise	2	0.139	0.138	0.151	0.145	–	–	0.143
SCB	Rise	50	0.128	0.136	–	–	–	–	0.132
ENDB	Rise	2	0.108	0.117	0.113	–	–	–	0.113

Table 4. Fracture toughness results for 300 kg/m^3 PUR foam density.

Specimen Type	Loading Direction	Loading Speed [mm/min]	Fracture Toughness [MPa·m$^{0.5}$]					
			1	2	3	4	5	Average
SENB-TPB	Flow	2	0.325	0.343	0.373	0.330	0.327	0.340
SENB-FPB	Flow	2	0.362	0.362	0.321	0.345	0.349	0.348
SEC	Flow	2	0.432	0.284	0.320	0.311	–	0.337
SCB	Flow	2	0.356	0.384	0.377	–	–	0.372
ENDB	Rise	2	0.343	0.347	0.342	–	–	0.344

The foam with 145 kg/m^3 density has an average value of the fracture toughness in the flow direction in the range 0.095–0.132 MPa·m$^{0.5}$, respectively for the rise direction between 0.116–0.143 MPa·m$^{0.5}$.

Finally, for the foam with a density of 300 kg/m^3, the fracture toughness values were obtained between 0.337–0.372 MPa·m$^{0.5}$ in the flow direction, respectively 0.344 MPa·m$^{0.5}$ in the rise direction.

Overall, it could be pointed out that the fracture toughness increases with density [29].

It could be observed that the anisotropy effect is higher for low-density foams (100 kg/m^3 and 145 kg/m^3) and diminished for 300 kg/m^3 density. This could be explained based on the cell topology (cells have different shapes in flow and rise direction), while for the foam with 300 kg/m^3 density cells are more regular like spheres [30].

4. Discussion: A Statistical Approach

The statistical analysis aimed at two objectives. The first is to determine the relationships between the fracture toughness of foams and different variables measured in several experiments. For this purpose, the regression method will be used [31]. The second goal is to analyze if the fracture toughness depends on the different densities and different types of specimens. This problem is equivalent to the problem of determining the effect size. For the second objective, the meta-analysis method will be considered [32].

For the statistical analysis it is denoted Y for the response variable, the mean value of the fracture toughness and five predictor variable: X1 - specimen type (1 = ”SENB-TPB”, 2 = ”SENB-FPB”, 3 = ”SEC”, 4 = ”ASCB”, 5 = ”ENDB”), X2—loading speed (2 or 50), X3 - density (100 kg/m^3, 145 kg/m^3 or 300 kg/m^3), X4 = direction plane (1 = ”in-plane-flow”, 0 = ”out of plane-rise”), X5 = number of measurements (2, 3, 4, 5).

The correlation matrix (see Table 5) shows some possible linear relations between the response and the predictors, also some relations between the predictors are given. Each cell of this matrix represents the Pearson correlation coefficient between any two of the variables X1, X2, X3, X4, X5, or Y describes above.

Table 5. Correlation matrix.

Variable	X1	X2	X3	X4	X5	Y
X1	1.00000000	0.3034885	−0.03203788	−0.3367175	−0.7642309	0.0396120
X2	0.30348849	1.0000000	−0.23335505	−0.1021899	−0.6698430	−0.1988581
X3	−0.03203788	−0.2333551	1.00000000	0.1993570	0.1841807	0.9853670
X4	−0.33671751	−0.1021899	0.19935697	1.0000000	0.2661637	0.1681640
X5	−0.76423093	−0.6698430	0.18418069	0.2661637	1.0000000	0.1289626
Y	0.03961200	−0.1988581	0.98536705	0.1681640	0.1289626	1.0000000

The multiple linear regression method and the backward selection procedure were used. The optimization process led to the conclusion that the response variable fracture toughness depends only on one predictor variable (density). Different regression models were analyzed. The goal of the regression analysis was to find the best relation between the response variable Y (mean value of the fracture toughness) and the predictor X3 (density). There exists some studies that indicated a linear relation ($Y = a + b \times X3$), a quadratic relation ($Y = a + c \times X3^2$) or a power relation ($Y = a \times X^{1.3}$, see [22]). In our analysis, we consider these models and other related models as follows:

1. Linear model, $Y = a + b \times X3$ (Table 6).

Results: The coefficient of determination $R^2 = 0.9789$, adjusted coefficient of determination $Ra^2 = 0.9696$. The model is statistically supported, with an error of less than 1% and a coefficient of determination of over 96% (below are the statistical indicators, using the R software (R version 4.0.0).

Table 6. Statistical parameters for the linear regression model.

	Estimate	Std. Error	t Value	Pr (>|t|)
a	−5.895e−02	0.984e−03	−6.561	1.69e−06 ***
b	1.337e−03	5.045e−05	26.492	<2e−16 ***
Residual Standard Error: 0.01836 on 21 Degrees of Freedom				
Multiple R-Squared: 0.9709, Adjusted R-Squared: 0.9696				
F-Statistic: 701.8 on 1 and 21 DF, *p*-Value: < 2.2e−16				

*** The value is less than 0.001.

The above table presents:

- Column Estimate—the estimation values of the parameters (estimations using least square method).
- Column Std. Erros—the statistical standard deviation of the parameters.

- Column t-value—the value of t test, which it is used to verify the null hypothesis H_0: a = 0, respectively H_0: b = 0, the expression of this test is estimated value / standard deviation.
- Column Pr(>|t|)—the probability to not reject the null hypothesis. It is obvious that some null value of the parameters (accept the null hypothesis) are not desirable because this means that the predictor is not significant, so a value small as possible is good to accept the proposed model.
- Residual standard error—the sum of values between the observed (measured) value and the value predicted by model (it is desirable to be small as possible), degrees of freedom is the number of observations minus the number of parameters.
- Multiple R-squared—the coefficient of determination 1-(Residual sum of squares/Total sum of squares), (Residual sum of squares is the sum of square distance between the observed values and the values predicted by model, total sum of squares is the sum of square distance between the observed values and the statistical (arithmetical) mean of observations), it is obvious that this value should be large as possible;
- Adjusted R-squared is a correction expression of the coefficient of determination (because this coefficient tends to increase with increasing number of parameters (i.e., predictors).
- F-statistic—the value of F-test to verify the null hypothesis H_0 a = b = 0 (both parameters are zero).
- *p*-value is the probability to not reject the null hypothesis, of course, a low value as possible it useful to accept the model.

2. Quadratic Model, $Y = a + c \times X3^2$ (Table 7)

Coefficient of determination $R^2 = 0.9847$, adjusted coefficient of determination $Ra^2 = 0.9839$.

Table 7. Statistical parameters for the quadratic regression model.

	Estimate	Std. Error	t Value	Pr (>|t|)
a	5.229e−02	3.70e−03	13.17	1.29e−11 ***
c	3.283e−06	8.939e−08	36.73	<2e−16 ***
Residual Standard Error: 0.01334 on 21 Degrees of Freedom				
Multiple R-Squared: 0.9847, Adjusted R-Squared: 0.9839				
F-Statistic: 1349 on 1 and 21 DF, *p*-Value: < 2.2e−16				

*** The value is less than 0.001.

3. Polynomial (second-order) model $Y = b \cdot X3 + c \cdot X3^2$ (Table 8)

Coefficient of determination $R^2 = 0.9943$, adjusted coefficient of determination $Ra^2 = 0.9938$.

Table 8. Statistical parameters for the polynomial regression model.

	Estimate	Std. Error	t Value	Pr (>|t|)
b	6.066e−04	5.165e−05	11.744	1.08e−10 ***
c	1.831e−06	2.071e−07	8.845	1.59e−08 ***
Residual Standard Error: 0.01475 on 21 Degrees of Freedom				
Multiple R-Squared: 0.9943, Adjusted R-Squared: 0.9938				
F-Statistic: 1842 on 1 and 21 DF, *p*-Value: < 2.2e−16				

*** The value is less than 0.001.

4. Power model $Y = a \cdot X3^b$ (Table 9)

Coefficient of determination $R^2 = 0.9421$, adjusted coefficient of determination $R_a^2 = 0.9393$.

This model can be obtained using a "linearization" method, applying the logarithm function the power model become a "linear" model. The linearization method does not lead the best estimates of parameters, but it gives an "initial" solution for the nonlinear least square method.

Table 9. Statistical parameters for the power regression model.

	Estimate	Std. Error	t Value	Pr (>|t|)
a	−8.41281	0.34679	−24.26	<2e−16 ***
b	1.28048	0.06927	18.48	1.8e−14 ***
Residual standard error: 0.1363 on 21 Degrees of Freedom				
Multiple R-Squared: 0.9421, Adjusted R-Squared: 0.9393				
F-Statistic: 341,7 on 1 and 21 DF, *p*-Value: 1.801e−14				

*** The value is less than 0.001.

From above, we observe that a good model seems to be by the form $Y = a \cdot X3^b$. We use a nonlinear regression procedure to estimate the parameters "a" and "b" (see Table 10).

Table 10. Statistical parameters for the nonlinear regression model.

	Estimate	Std. Error	t Value	Pr (>|t|)
a	1.430e−04	3.721e−05	3.844	0.000943 ***
b	1.366e + 00	4.723e−02	28.924	<2e−16 ***
Residual Standard Error: 0.01565 on 21 Degrees of Freedom				
Number of Iterations to Convergence: 7				
Achieved Convergence Tolerance: 5.974e−07				

*** The value is less than 0.001.

In a nonlinear regression can be computed just a quasi-coefficient of determination using the same relation as that described after the Table 6. To compare more nonlinear regression models can be used some informational criterion as AIC (Akaike's Information Criterion, 2 * number of parameters—logarithm of the likelihood function) or BIC (Bayesian Informational Criterion). Also, we can mention that for the "initial" values b = 1 or b = 2, the nonlinear least square method yields the same value b = 1.366.

Using the above estimation (b = 1.366) we consider the following power model (5):

5. Power model $Y = a + b \cdot X3^{1.366}$ (Table 11)

Coefficient of determination $R^2 = 0.9793$, adjusted coefficient of determination $R_a^2 = 0.9783$.

Table 11. Statistical parameters for the power regression model $Y = a + b \cdot X3^{1.366}$.

	Estimate	Std. Error	t Value	Pr (>|t|)
a	2.370e−13	5.853e−03	0.405	0.69
b	1.416e−04	4.488e−06	31.544	<2e−16 ***
Residual Standard Error: 0.01549 on 21 Degrees of Freedom				
Multiple R-Squared: 0.9793, Adjusted R-Squared: 0.9783				
F-Statistic: 995 on 1 and 21 DF, *p*-Value: < 2.2e−16				

*** The value is less than 0.001.

Also, these values are obtained using the linearization method.

Because the *p*-value of the free term (intercept) is too big (0.69) we will analyze the above model without intercept (6):

6. Power model $Y = b \cdot X3^{1.366}$ (Table 12)

Coefficient of determination $R^2 = 0.9937$, adjusted coefficient of determination $R_a^2 = 0.9934$. Again, we used the linearization method to calculate these values.

Table 12. Statistical parameters for the power regression model $Y = b \cdot X3^{1.366}$.

	Estimate	Std. Error	t Value	Pr (>|t|)
B	1.431e−04	2.428e−06	58.93	<2e−15 ***
Residual Standard Error: 0.01519 on 21 Degrees of Freedom				
Multiple R-Squared: 0.9937, Adjusted R-Squared: 0.9934				
F-Statistic: 3472 on 1 and 21 DF, *p*-Value: < 2.2e−16				

*** The value is less than 0.001.

Statistically, the best models are the polynomial model (model d) and the last power model (model h) (because explains 99 % of situations). All models are made with an error of less than 1%. (chosen significance level alpha = 0.01). Because are just some very small differences between the values of coefficient of determination at these models can be sustain that are equally good statistically. Also, follows the remark that for nonlinear model we obtained a value of this coefficient based on linearization method, the nonlinear model seems to be better.

A meta-analysis was performed to study possible measurement errors (Table 13). The values for density = 100 kg/m^3 were considered as the control group and the values for density = 145 kg/m^3 as the experimental group. Data obtained using the R software and the meta-package [33]. The fixed effect model provides a weighted average of a series of study estimates. A common model used to synthesize heterogeneous research is the random effects model of meta-analysis. For details of the values from below table, see [32,33].

Table 13. Meta-analysis of densities.

Number of Studies Combined: k = 9				
	SMD	**95%-CI**	**z**	***p*-Value**
Fixed Effect Model	3.0705	[1.9954; 4.1455]	5.60	<0.0001
Random Effects Model	3.7582	[2.1870; 5.3294]	4.69	<0.0001
Quantifying Heterogeneity: tau^2 = 1.9157; H = 1.27 [1.00; 1.87]; I^2 = 37.5% [0.0%; 71.3%]				
Test of Heterogeneity:				
	Q	**DF**	***p*-Value**	
	12.80	8	0.1187	
Details on Meta-Analytical Method: Inverse Variance Method DerSimonian-Laird Estimator for tau^2 Hedges' g (bias-Corrected Standardized Mean Difference)				

It is observed that there is a difference between the fixed and the random effect, in other words, the difference between the average values depends on a fixed effect (density difference) and there are only small differences due to chance (normal statistical errors).

In addition, a meta-analysis was performed to study whether there was an effect on the difference between the types of specimens (Table 14). The SEC specimen was considered as a control model and the ENDB specimen as an experimental model.

It is observed that the fixed effect coincides with the random one, in other words, the difference is only due to chance and it cannot be stated that there is a difference due to the choice of a certain type of specimen.

Table 14. A meta-analysis of specimen types.

Number of Studies Combined: k = 3				
	SMD	**95%-CI**	**z**	***p*-Value**
Fixed Effect Model	0.2373	[−0.6350; 1.1095]	0.53	0.5940
Random Effects Model	0.2373	[−0.6350; 1.1095]	0.53	0.5940
Quantifying Heterogeneity: $tau^2 = 0$; H = 1.00 [1.00; 1.00]; I^2 = 0.0% [0.0%; 0.0%]				
Test of Heterogeneity:				
	Q	**DF**	***p*-Value**	
	0.05	2	0.9743	
Details on Meta-Analytical Method: Inverse Variance Method DerSimonian-Laird Estimator for tau^2 Hedges' g (bias-Corrected Standardized Mean Difference)				

5. Conclusions

The statistical analysis based on the experimental results indicates that the fracture toughness represents a material property of PUR foams, because does not depend on the specimen type. From the practical point of view, this conclusion is important, allowing to consider any type of specimen, based on the availability, to determine the fracture toughness. On other hand, the fracture criterion based on the stress intensity factor K_I and on the critical value, also known as fracture toughness K_{IC}: $K_I \leq K_{IC}$, could be successfully applied to structures made of PUR foams. The size effect shows that for large PUR foams structures the linear elastic fracture mechanics applies [13,27] and the fracture parameters have a crucial role on the integrity assessment.

The density plays a major role in the fracture toughness of PUR foams. The statistical analysis based on the experimental data shows that the linear model, the power models, and the square root model fitted the micromechanical models described by eq. (1) with resulting values for m = 1, 1.366, 1.5, all having a coefficient of determination higher than 0.94. The highest being obtained for the power model with m = 1.366. Also, a combined model between model with m = 1 and model with m = 2 seems to be good. These results based on the statistical analysis are in agreement with other published data [21–23].

The irregular shape of the cells induced small anisotropy for low-density foams (100 kg/m^3 and 145 kg/m^3). This effect could not be observed for the foam with 300 kg/m^3 density, for which the cells have a more regular spherical shape.

The statistical analysis indicates that the influence of the loading speed is very weak.

Author Contributions: Conceptualization, L.M. and A.P.; experimental investigation, E.L. and L.M.; statistical analysis, A.P. and R.N.; writing—original draft preparation, L.M. and R.N.; writing—review and editing L.M. and A.P.; supervision, A.P. All authors have read and agreed to the published version of the manuscript.

Funding: This research was funded by the Romanian Ministry of Education and Research, grant number PN-III-P1-1.2-PCCDI-2017-0391, and the APC was funded by the Romanian Ministry of Education and Research CNFIS-FDI-2020-0358.

Conflicts of Interest: The authors declare no conflict of interest.

References

1. Wang, H.; Li, T.-T.; Wu, L.; Lou, C.-W.; Huang, S.-Y. Multifunctional, Polyurethane-Based Foam Composites Reinforced by a Fabric Structure: Preparation, Mechanical, Acoustic, and EMI Shielding Properties. *Materials* **2018**, *11*, 2085. [CrossRef] [PubMed]
2. Linul, E.; Marşavina, L.; Vălean, C.; Bănică, R. Static and dynamic mode I fracture toughness of rigid PUR foams under room and cryogenic temperatures. *Eng. Fract. Mech.* **2020**, *225*, 106274. [CrossRef]

3. Horak, Z.; Dvorak, K.; Zarybnicka, L.; Vojackova, H.; Dvorakova, J.; Vilimek, M. Experimental Measurements of Mechanical Properties of PUR Foam Used for Testing Medical Devices and Instruments Depending on Temperature, Density and Strain Rate. *Materials* **2020**, *13*, 4560. [CrossRef] [PubMed]
4. Thiyagasundaram, P.; Wang, J.; Sankar, B.V.; Arakere, N.K. Fracture toughness of foams with tetrakaidecahedral unit cells using finite element based micromechanics. *Eng. Fract. Mech.* **2011**, *78*, 1277–1288. [CrossRef]
5. Ashby, M.F. Materials Selection in Mechanical Design. *Mater. Des.* **2011**, 72–76. [CrossRef]
6. Arencón, D.; Antunes, M.; Martínez, A.; Velasco, J.I. Study of the fracture behavior of flexible polypropylene foams using the Essential Work of Fracture (EWF). *Polym. Test.* **2012**, *31*, 217–225. [CrossRef]
7. ASTM International. *Standard Test Methods for Plane-Strain Fracture Toughness and Strain Energy Release Rate of Plastic materials*; ASTM International: Conshohocken, PA, USA,, 2014.
8. McIntyre, A.; Anderton, G.E. Fracture properties of a rigid PU foam over a range of densities. *Polymer* **1979**, *20*, 247–253. [CrossRef]
9. Kabir, E.; Saha, M.; Jeelani, S. Tensile and fracture behavior of polymer foams. *Mater. Sci. Eng. A* **2006**, *429*, 225–235. [CrossRef]
10. Viana, G.M.; Carlsson, L.A. Mechanical properties and fracture characterisation of cross-linked PVC foams. *J. Sandw. Struct. Mater.* **2002**, *4*, 91–113. [CrossRef]
11. Andersons, J.; Cabulis, U.; Stiebra, L.; Spārniņš, E.; Kirpluks, M. Modeling the mode I fracture toughness of anisotropic low-density rigid PUR and PIR foams. *Int. J. Fract.* **2017**, *205*, 111–118. [CrossRef]
12. Jelitto, H.; Schneider, G.A. Fracture toughness of porous materials - Experimental methods and data. *Data Brief.* **2019**, *23*, 103709. [CrossRef] [PubMed]
13. Marsavina, L.; Linul, E. Fracture toughness of rigid polymeric foams: A review. *Fatigue Fract. Eng. Mater. Struct.* **2020**, *43*, 2483–2514. [CrossRef]
14. Linul, E.; Vălean, C.; Linul, P.-A. Compressive Behavior of Aluminum Microfibers Reinforced Semi-Rigid Polyurethane Foams. *Polymers* **2018**, *10*, 1298. [CrossRef] [PubMed]
15. Park, K.-B.; Kim, H.-T.; Her, N.-Y.; Lee, J.M. Variation of Mechanical Characteristics of Polyurethane Foam: Effect of Test Method. *Materials* **2019**, *12*, 2672. [CrossRef]
16. Marsavina, L. Fracture Mechanics of Foams. In *Cellular and Porous Materials in Structures and Processes*; Altenbach, H., Ochsner, A., Eds.; Springer: Wien, Austria, 2010; Volume 521, pp. 1–46.
17. Marşavina, L.; Constantinescu, D.M. *Failure and Damage in Cellular Materials*; Altenbach, H., Sadowski, T., Eds.; Springer: Wien, Austria, 2015; Volume 560, pp. 119–190.
18. Fowlkes, C.W. Fracture toughness tests of a rigid polyurethane foam. *Int. J. Fract.* **1974**, *10*, 99–108. [CrossRef]
19. Marsavina, L.; Linul, E. Fracture toughness of polyurethane foams. Experiments versus micromechanical models. In Proceedings of the 18th European Conference on Fracture, Dresden, Germany, 30 August–3 September 2010; pp. 1–8.
20. Poapongsakorn, P.; Carlsson, L.A. Fracture toughness of closed-cell PVC foam: Effects of loading configuration and cell size. *Compos. Struct.* **2013**, *102*, 1–8. [CrossRef]
21. Maiti, S.; Ashby, M.; Gibson, L. Fracture toughness of brittle cellular solids. *Scr. Met.* **1984**, *18*, 213–217. [CrossRef]
22. Green, D. Fabrication and Mechanical Properties of Lightweight Ceramics Produced by Sintering of Hollow Spheres. *J. Am. Ceram. Soc.* **1985**, *68*, 403–409. [CrossRef]
23. Choi, S.; Sankar, B. A micromechanical method to predict the fracture toughness of cellular materials. *Int. J. Solids Struct.* **2005**, *42*, 1797–1817. [CrossRef]
24. Murakami, Y.; Keer, L.M. Stress Intensity Factors Handbook, Vol. 3. *J. Appl. Mech.* **1993**, *60*, 1063. [CrossRef]
25. Apostol, D.A.; Stuparu, F.; Constantinescu, D.M.; Marsavina, L.; Linul, E. Crack Length Influence on Stress Intensity Factors for the Asymmetric Four-point Bending Testing of a Polyurethane Foam. *Mater. Plast.* **2016**, *53*, 280–282.
26. Marsavina, L.; Constantinescu, D.M.; Linul, E.; Voiconi, T.; Apostol, D.A. Shear and mode II fracture of PUR foams. *Eng. Fail. Anal.* **2015**, *58*, 465–476. [CrossRef]
27. Marsavina, L.; Constantinescu, D.M.; Linul, E.; Apostol, D.A.; Voiconi, T.; Sadowski, T. Refinements on fracture toughness of PUR foams. *Eng. Fract. Mech.* **2014**, *129*, 54–66. [CrossRef]
28. Aliha, M.R.M.; Linul, E.; Bahmani, A.; Marsavina, L. Experimental and theoretical fracture toughness investigation of PUR foams under mixed mode I+III loading. *Polym. Test.* **2018**, *67*, 75–83. [CrossRef]

29. Andersons, J.; Kirpluks, M.; Cabulis, U. Reinforcement Efficiency of Cellulose Microfibers for the Tensile Stiffness and Strength of Rigid Low-Density Polyurethane Foams. *Materials* **2020**, *13*, 2725. [CrossRef]
30. Linul, E.; Şerban, D.A.; Marşavina, L. Influence of Cell Topology on Mode I Fracture Toughness of Cellular Structures. *Phys. Mesomech.* **2018**, *21*, 178–186. [CrossRef]
31. Zarr, R.R.; Pintar, A.L. *Standard Reference Materials: SRM 1453, Expanded Polystyrene Board, for Thermal Conductivity from 281 K to 313 K*; NIST Special Publication: Gaithersburg, MD, USA, 2012; p. 175.
32. Kulinskaya, E.; Morgenthaler, S.; Staudte, R.G. *Meta analysis: A Guide to Calibrating and Combining Statistical Evidence*; John Wiley & Sons Ltd: Chichester, UK, 2008; pp. 85–104.
33. Guido, S. *General Package for Meta-Analysis*; Springer: Berlin/Heidelberg, Germany, 10 February 2020; pp. 76–88.

Continuum Mech. Thermodyn.
https://doi.org/10.1007/s00161-020-00924-x

ORIGINAL ARTICLE

Dan-Andrei Şerban · Radu Negru · Hannelore Filipescu · Liviu Marşavina

Investigations on the influence of the triaxial state of stress on the failure of polyurethane rigid foams

Received: 24 March 2020 / Accepted: 28 August 2020

Abstract This paper investigates the failure strain as a dependence of the stress triaxiality and the Lode angle parameter for polyurethane rigid foams (PUR) of two densities (100 and 300 kg/m^3). Tests were carried out in tension for various configurations, resulting in different states of stress triaxiality at various Lode angles in the critical areas. The failure strain was determined for each setup using finite element analysis, as the tests were replicated with numerical models. The displacement at failure recorded in the experiments was imposed for the models, determining the failure strain as a function of stress triaxiality and the Lode angle parameter. The results were validated through the analysis of the failure of sandwich structures with aluminium faces and PUR cores.

Keywords PUR foam · Failure · Stress triaxiality · Experiment · Numerical simulation

List of symbols

d	Plastic displacement
D	Damage evolution parameter
e^{c}	Logarithmic compressive strain
e^{t}	Logarithmic tensile strain
I_1	First invariant of the stress tensor
J_2	Second invariant of the deviatoric stress tensor
J_3	Third invariant of the deviatoric stress tensor
p	Hydrostatic pressure
p^{c}	Yield stress in hydrostatic compression
p^{t}	Yield stress in hydrostatic tension
q	von Mises equivalent stress
r	Normalized third invariant
s^{c}	True compressive stress
s^{t}	True tensile stress
γ	Bai–Wierzbicki Lode angle-dependent parameter
ε^{c}	Engineering compressive strain

Communicated by Luca Placidi and Emilio Barchiesi.

D.-A. Şerban (✉)· R. Negru · L. Marşavina
Department of Mechanics and Strength of Materials, Politehnica University Timişoara, Timisoara, Romania
E-mail: dan.serban@upt.ro

H. Filipescu
Department of Mechatronics, Politehnica University Timişoara, Timisoara, Romania

Published online: 09 September 2020

ε^{t}	Engineering tensile strain
$\bar{\varepsilon}_{\mathrm{D}}^{\mathrm{pl}}$	Critical plastic strain
$\bar{\varepsilon}^{\mathrm{pl}}$	Equivalent plastic strain
$\dot{\bar{\varepsilon}}^{\mathrm{pl}}$	Equivalent plastic strain rate
η	Stress triaxiality
$\bar{\theta}$	Lode angle
ν	Poisson's ratio
ξ	Lode angle parameter
$\boldsymbol{\sigma}$	Stress tensor
$\bar{\boldsymbol{\sigma}}$	Effective stress tensor
σ^{c}	Engineering compressive stress
σ^{t}	Engineering tensile stress
σ_{ij}	Stress tensor components
σ_i	Principal stresses
$\boldsymbol{\sigma}'$	Deviatoric stress tensor
σ'_{ij}	Deviatoric stress tensor components
σ_{y}	Equivalent yield stress
Φ	Yield function
ψ	Dissipated plastic energy
ω	Damage initiation parameter

1 Introduction

Polyurethane rigid (PUR) foams represent a class of lightweight materials that, due to their mechanical and thermal properties, are used in a wide range of applications such civil engineering (thermal insulating panels), naval industry (composite panels with good floatability), railway transportation, automotive and aerospace applications (composite panels with good mechanical properties at low specific weights) [1–3].

Previous work performed by the authors was concerned with the experimental determination of the flexural properties of sandwich beams composed of 1050 H24 aluminium alloy faces and PUR cores of two densities (100 kg/m^3 and 300 kg/m^3), bonded together using Araldite AW 106 resin/Hardener HV 953U epoxy adhesive [4]. Two types of beams were tested, one with compact cores and the other with a perforated pattern [4].

The aim of this study is to develop constitutive models for the sandwich beam components that can accurately replicate the mechanical response as well as the occurring damage. Emphasis was placed on the calibration of constitutive models for the polyurethane foam, as the complex state of stress that occurs during the flexural loading of the perforated core has a decisive role on the failure of the beams.

Due to the brittle failure of PUR foams, previous studies were concerned with the application of various linear elastic fracture mechanics concepts (such as the Generalized Maximum Tangential Stress model, the Theory of Critical Distances, or the Averaged Strain Energy Density theory) in evaluating the structural integrity [5–7]. In this work, an elastic–plastic approach was considered, the failure of the material being modelled with the assumption that the critical plastic strain is a function of the stress triaxiality and of the Lode angle parameter.

2 Plasticity and damage

The mechanical behaviour of materials is assumed to be dependent on three invariants:

- the first invariant of the stress tensor I_1

$$I_1 = \mathrm{tr}\,(\boldsymbol{\sigma}) = \sum_{i=1}^{3} \sigma_{ii} \tag{1}$$

- The second invariant of the deviatoric stress tensor J_2

$$J_2 = \frac{1}{2} \sum_{i,j=1}^{3} \left(\sigma'_{ii} \sigma'_{jj} - \sigma'_{ij} \sigma'_{ji} \right) \tag{2}$$

- The third invariant of the deviatoric stress tensor J_3

$$J_3 = \det\left(\sigma'\right) = \sum_{i,j,k=1}^{3} \sigma_{ij}^{'}\sigma_{jk}^{'}\sigma_{ki}^{'} \tag{3}$$

In order to better understand the influence of these invariants, physical interpretations are often used in defining various material models.

The hydrostatic pressure (mean stress) p is defined as a function of the first invariant of the stress tensor. The sign of p denotes whether the body or element is subjected to tensile loadings ($p > 0$) or compressive loadings ($p < 0$). Expressed as a function of the principal stresses, it is defined as [8]:

$$p = \frac{I_1}{3} = \frac{\sigma_1 + \sigma_2 + \sigma_3}{3}[\text{MPa}] \tag{4}$$

The von Mises equivalent stress q is defined as a function of the second invariant of the deviatoric stress, and it is linked to the distortional energy consumed during deformation:

$$q = \sqrt{3J_2} = \frac{1}{\sqrt{2}}\left[(\sigma_1 - \sigma_2)^2 + (\sigma_2 - \sigma_3)^2 + (\sigma_3 - \sigma_1)^2\right]^{\frac{1}{2}}[\text{MPa}] \tag{5}$$

Considering the aforementioned stress measures, the stress triaxiality η is defined as:

$$\eta = \frac{p}{q}[-] \tag{6}$$

The third invariant can be normalized to a corresponding stress value r, defined as:

$$r = \left[\frac{27}{2}J_3\right]^{\frac{1}{3}} = \left[\frac{1}{2}(2\sigma_1 - \sigma_2 - \sigma_3)(2\sigma_2 - \sigma_1 - \sigma_3)(2\sigma_3 - \sigma_1 - \sigma_2)\right]^{\frac{1}{3}}[\text{MPa}] \tag{7}$$

The influence of the third invariant is expressed through the Lode angle parameter ξ:

$$\xi = \left[\frac{r}{q}\right]^3 = \frac{3}{2}\sqrt{3}\frac{J_3}{J_2^{\frac{3}{2}}} \in [-1, 1] \tag{8}$$

The Lode angle parameter characterizes the loading type a body/element is subjected to. Its extreme values denote uniaxial compression and equibiaxial tension ($\xi = -1$), uniaxial tension and equibiaxial compression ($\xi = 1$), while for shear $\xi = 0$.

The most commonly used yield criterion was formulated by Richard von Mises, and it is expressed as a function of the second invariant of the stress deviator J_2:

$$\Phi = J_2^2 - \frac{\sigma_y^2}{3} \tag{9}$$

Though accurate for steels, other classes of materials (such as aluminium alloys) exhibit different yielding behaviours when the Lode angle parameter does not equal -1 or 1. In consequence, several third invariant-dependent yield criteria were proposed, such as Hosford's criterion, Eq. (10a) [9], or the Bai–Wierzbicki criterion, Eq. (10b) [10].

$$\Phi = (\sigma_1 - \sigma_2)^{2k} + (\sigma_2 - \sigma_3)^{2k} + (\sigma_3 - \sigma_1)^{2k} - 2\sigma_y^{2k} \tag{10a}$$

$$\Phi = q - \sigma_y\left[1 - c_\eta\left(\eta - \frac{1}{3}\right)\right]\left[c_\theta^s + \left(c_\theta^{ax} - c_\theta^s\right)\left(\gamma - \frac{\gamma^{m+1}}{m+1}\right)\right] \tag{10b}$$

where γ is a parameter dependent on the Lode angle $\bar{\theta}$

$$\gamma = \frac{\sqrt{3}}{2 - \sqrt{3}}\left[\sec\left(\frac{\bar{\theta}\pi}{6}\right) - 1\right] \tag{10c}$$

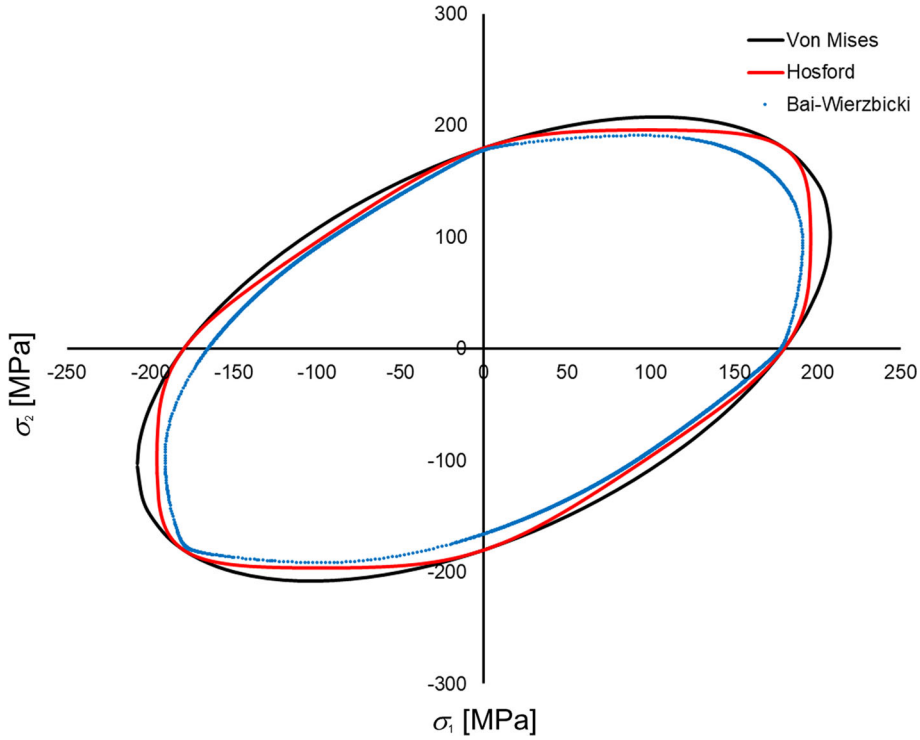

Fig. 1 von Mises, Hosford and Bai–Wierzbicki yield surfaces for plane stress conditions

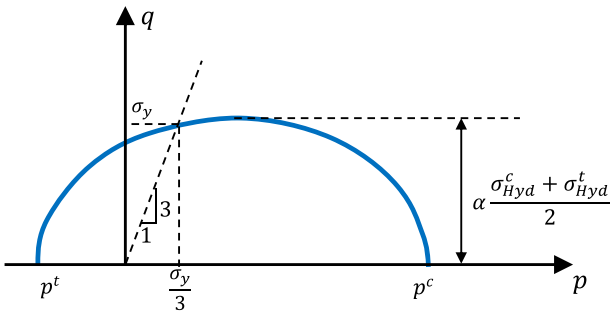

Fig. 2 Deshpande–Fleck yield surface in the p–q plane

$$\bar{\theta} \quad = \quad 1 - \frac{2}{\pi}\arccos\left(\xi\right) \tag{10d}$$

and $c_\eta \quad c_\theta^s$, c_θ^{ax}, c_θ^s and m are material parameters that are calibrated from experimental data (Fig. 1).

Constitutive models for crushable cellular materials take into account the effects of the hydrostatic pressure on yielding. The most commonly used model was proposed by Deshpande and Fleck [11] and defines the yield function as:

$$\Phi = \sqrt{q^2 + \alpha^2\left[p^{\mathrm{c}} - p^{\mathrm{t}}\right]^2} - \alpha\frac{p^{\mathrm{c}} + p^{\mathrm{t}}}{2} \tag{11}$$

where p^{c} and p^{t} are the yield stress in hydrostatic compression and tension, respectively, and α is a parameter dependent on the hydrostatic yield stress and on the uniaxial yield stress in compression. The shape of the initial yield surface in the p–q plane is presented in Fig. 2.

The damage formulation assumed in this work is based on the principle of nucleation and subsequent growth of voids in the material during loading [12]. This process modelled in two steps: the initiation of damage when a certain criterion is met (void nucleation) and the evolution of damage, which consists of the progressive reduction in element stiffness (void growth) [13,14].

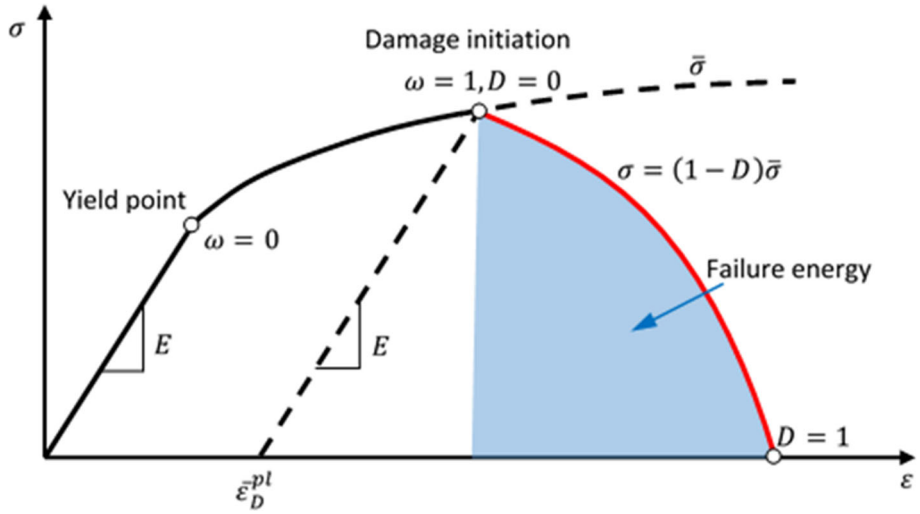

Fig. 3 Stress–strain evolution at an integration point for the ductile damage model

The chosen model for the damage initiation criterion assumes that the degradation of the material occurs when a certain equivalent critical plastic strain $\bar{\varepsilon}_{\mathrm{D}}^{\mathrm{pl}}$ is reached, which is a function of the stress triaxiality, the Lode angle parameter ξ and the equivalent plastic strain rate $\dot{\bar{\varepsilon}}^{\mathrm{pl}}$

$$\bar{\varepsilon}_{\mathrm{D}}^{\mathrm{pl}} = f\left(\eta, \xi, \dot{\bar{\varepsilon}}^{\mathrm{pl}}\right) \tag{12}$$

Therefore, the damage initiation parameter ω is expressed as:

$$\omega = \int \frac{d\bar{\varepsilon}^{\mathrm{pl}}}{\bar{\varepsilon}_{\mathrm{D}}^{\mathrm{pl}}} \tag{13}$$

where $\bar{\varepsilon}^{\mathrm{pl}}$ is the equivalent plastic strain:

$$\bar{\varepsilon}^{\mathrm{pl}} = \int \dot{\bar{\varepsilon}}^{\mathrm{pl}} \mathrm{d}t = \int \left(\sqrt{\frac{2}{3}\dot{\varepsilon}_{ij}^{\mathrm{pl}}\dot{\varepsilon}_{ij}^{\mathrm{pl}}}\right) \mathrm{d}t \tag{14}$$

When $\omega = 1$, the damage initiation conditions are met and the stress at an integration point will be calculated with the relation:

$$\boldsymbol{\sigma} = (1 - D)\,\bar{\boldsymbol{\sigma}} \tag{15}$$

where $\boldsymbol{\sigma}$ is the stress tensor, $\bar{\boldsymbol{\sigma}}$ is the effective (undamaged) stress tensor and D is the damage evolution parameter. The damage evolution parameter D progressively reduces the effective stress in an integration point, and if reaches a value of 1 (when a given criterion is reached, such as dissipated energy ψ or plastic displacement d), the element is excluded from the analysis. The damage evolution can be defined as a linear function, an exponential function or can be input as tabular data [13]

In summary, this degradation model assumes that when a critical plastic strain is reached (and subsequently $\omega = 1$), the effective stress from an integration point is gradually reduced through a damage evolution law ($D = f(\psi)$ or $D = f(d)$) until $D = 1$ and $\boldsymbol{\sigma} = 0$, at which point the element is considered to have failed and is removed (Fig. 3).

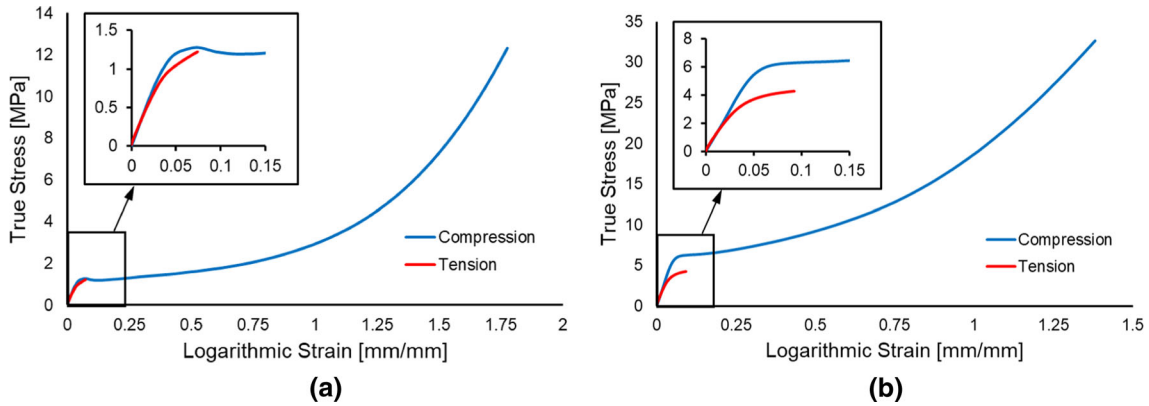

Fig. 4 Tensile and compressive results for 100 kg/m^3 (**a**) and 300 kg/m^3 (b)

3 Preliminary tests and material model calibration

3.1 Polyurethane rigid foams

The mechanical properties of the polyurethane foams were investigated for compression, tension and bending. Compression tests were performed on 25 mm sided cubes, while tensile tests were performed on ISO 527 dog-bone specimens [15]. The recorded (engineering) stress–strain values were converted to true stress–logarithmic strain values with the equations:

$$e^{\mathrm{c}} = -\ln\left(1 - \left|\varepsilon^{\mathrm{c}}\right|\right) \tag{16a}$$

$$e^{\mathrm{t}} = \ln\left(1 + \varepsilon^{\mathrm{t}}\right) \tag{16b}$$

$$s^{\mathrm{c}} = \frac{\left|\sigma^{\mathrm{c}}\right|}{\left(1 + \nu\left|\varepsilon^{\mathrm{c}}\right|\right)^2} \tag{16c}$$

$$s^{\mathrm{t}} = \frac{\sigma^{\mathrm{t}}}{\left(1 - \nu\varepsilon^{\mathrm{t}}\right)^2} \tag{16d}$$

The true stress–logarithmic strain curves in absolute values for tension and compression are presented in Fig. 4 for both investigated densities. Tensile tests show an elastic–plastic response characteristic for a semi-brittle material (low plastic strains at failure) while the compression tests exhibit the three stages of deformation characteristic to cellular materials [16].

It can be observed that the tensile and compressive stiffness is similar in the case of both densities, but the tensile yield points are lower, the difference being more pronounced for the 300 kg/m^3 density.

Considering the fact that the tensile behaviour of the materials determines the failure, the material models were calibrated after the tensile stress–strain curves. Having no volumetric data, the material parameters required to calibrate the Deshpande–Fleck model were chosen as $p^{\mathrm{c}} = p^{\mathrm{t}} = \sigma_{\mathrm{y}}$ and $\alpha = 0$, thus resulting a von Mises yield function. The hardening functions extracted from the true stress–logarithmic strain curves [17,18] and implemented in Abaqus yield accurate results (Fig. 5).

3.2 Tests on aluminium sheets and AW106 adhesive

The mechanical properties of the aluminium and adhesive were evaluated in tensile loadings on dogbone specimens [15,19] at room temperature, with a crosshead travel of 1 mm/min, the strains being recorded with an extensometer. The material models consisted of linear elasticity with von Mises plasticity and isotropic hardening, the plasticity data being extracted from the true stress–logarithmic strain values as described above. A damage model was calibrated for each material, considering the recorded failure plastic strain at a stress triaxiality value of 0.33 (corresponding to the uniaxial tensile loading). For the adhesive, the values were input as tabular data, while for the aluminium, the Johnson–Cook damage model (Eq. (17), [20]) was calibrated,

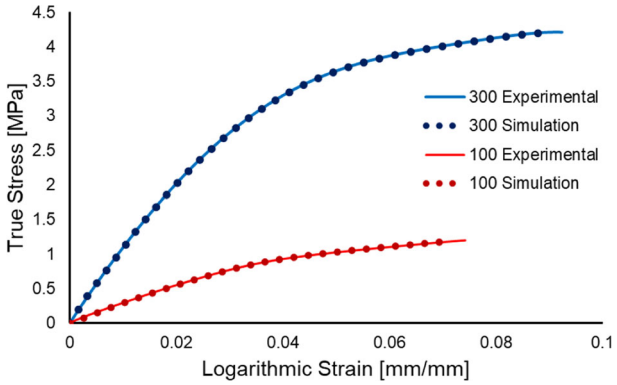

Fig. 5 Experimental and numerical results for tensile tests

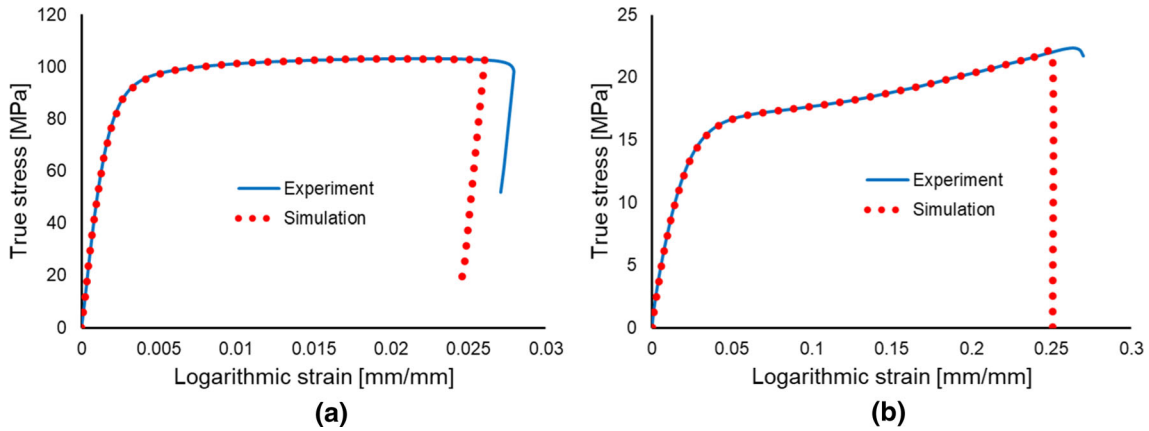

Fig. 6 Experimental an numerical results for aluminium sheets (a) and adhesive (b)

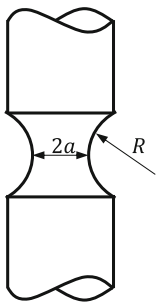

Fig. 7 Notched round bar specimen

with the parameters $d_1 = 0.0104$, $d_2 = 0.097$ and $d_3 = 5.358$.

$$\bar{\varepsilon}_{\mathrm{D}}^{\mathrm{pl}}(\eta) = d_1 + d_2^{-d_3\eta} \tag{17}$$

Numerical analyses were performed in order to evaluate the material models, yielding good results (Fig. 6).

4 Determination of failure strain–stress triaxiality data on notched round specimens

The use of notched round bar specimens (Fig. 7) for the determination of the failure strain as a function of the stress triaxiality has been extensively used for metals [21–23].

The relation between the $a/2R$ ratio and stress triaxiality was evaluated according to Bridgman's analytical formula [23] and through numerical analyses (the values presented in Fig. 8 corresponding to the

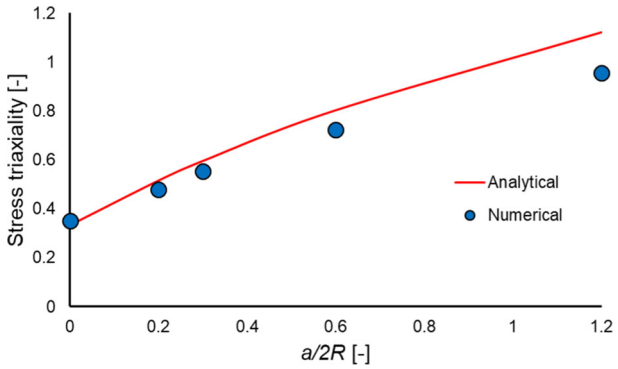

Fig. 8 Analytical and numerical results for the a/2R influence on the stress triaxiality

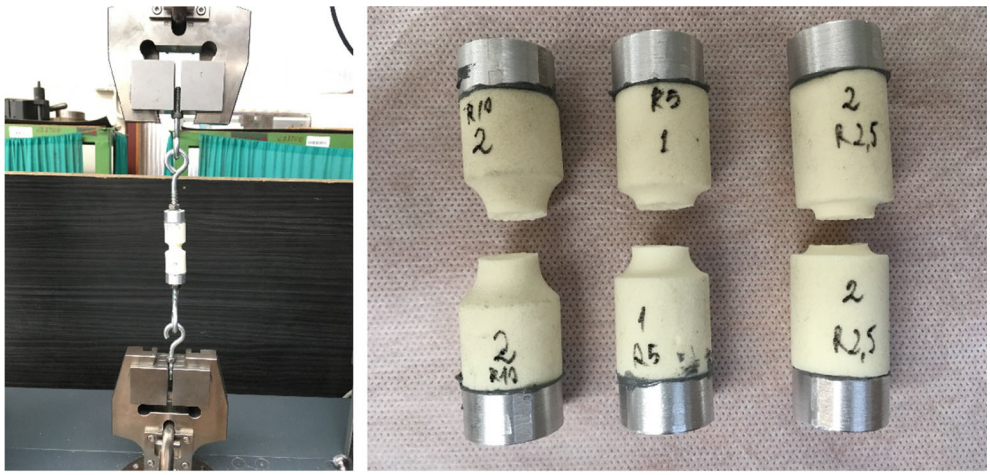

Fig. 9 Notched cylindrical specimen setup (**a**) and fractured samples (**b**)

onset of plasticity). For the experimental procedures, five $a/2R$ ratios were chosen: 0 (plane stress tension); 0.2; 0.3; 0.6; 1.2.

$$\eta = \frac{1}{3} + \ln\left(1 + \frac{a}{2R}\right) \tag{18}$$

The specimens used in this study were machined (through turning) from cylinders with a diameter of 20 mm, the notches being obtained using profiled tools. The diameter of the critical region was $2a = 12$ mm for all specimens, the profiled tools having radii R of 2, 5 mm, 5 mm, 10 mm and 15 mm, respectively. The overall height of the specimens was around 60 mm.

In order to avoid the effect of direct clamping, the specimens were fixed to aluminium cylindrical tabs (using the AW106 adhesive) and the gripping was perform with the help of steel hooks that were threaded into the tabs in order to align the specimens with the machine axis (Fig. 9a).

The tests were performed at 1 mm/min crosshead travel speed with preload of $5N$. Three specimens were tested for each configuration, and the graphs depicting representative stress–displacement curves for each geometry are presented in Fig. 10.

Figure 10 shows that the third invariant of the stress deviator (and consequently the Lode angle parameter) has an influence on the plasticity of the polyurethane foams (with a more pronounced effect on the 300 kg/m^3 density), as lower values for the radii (and higher stress concentration) determine an earlier yielding point. In consequence, the Von Mises yield surface might not determine accurate simulation results.

In order to determine the critical plastic strain and stress triaxiality values, each specimen was measured before testing and CAD models were generated respecting the dimensions. For the mesh, second-order tetrahedral elements were used (C3D10M), with mesh refinement in the notch region (the number of element varying from 0.8×10^6 to 1.7×10^6 as shown in Fig. 11), using the material models described in Paragraph 3.1.

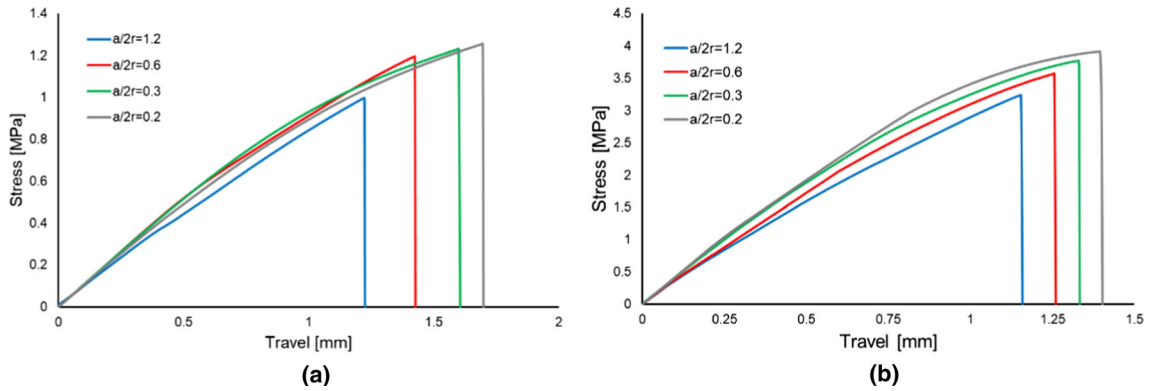

Fig. 10 Experimental results for the notched round specimen tests for 100 kg/m^3 (**a**) and 300 kg/m^3 (**b**)

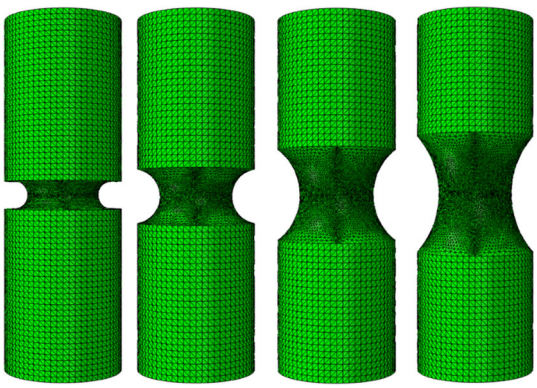

Fig. 11 Meshed models used in numerical analyses

The clamping system was considered rigid, and thus, the recorded displacement at failure was attributed to the top surface of the specimen (the bottom surface being fixed). When the given displacement is reached, node paths were defined across the critical region, recording the variation in equivalent plastic strain, stress triaxiality, von Mises equivalent stress and the third invariant with the radius. The results are plotted in Fig. 13 for both densities with the origin of the coordinate system corresponding to the centre of the specimen.

From Fig. 12, it can be observed that neither parameter is constant throughout the cross sections of the specimens at failure. Considering the extreme values, Fig. 13 presents the variation in the critical plastic strain with the stress triaxiality for the contour (assuming that the failure was initiated at the surface of the specimen) and for the middle of the cross section (assuming that the failure was initiated in the centre of the specimen). It can be observed that, at a given stress triaxiality, the model assuming that the failure occurs in the centre of the specimens fails much earlier. For instance, using the critical plastic strain–stress triaxiality curve obtained from the centre of the specimen would determine a shorter travel at failure for the specimens with $a/2R = 1.2$: at a stress triaxiality of 0.5, the critical plastic strain at the surface of the specimens would be 0.024 mm/mm, as opposed to the 0.077 mm/mm, as obtained by the imposed displacement at failure. This may be due to the influence of the Lode angle parameter, as it is reaches a value of $\xi = 0.43$ at the surface of the specimen while in the centre it remains constant at $\xi = 1$ for the failure of all geometries. Therefore, it can be hypothesized that the failure initiates at the surface of the specimen, where the Lode angle parameter is smaller, and, for larger values (maximal value of 1 in the case of the centre of the specimen), the critical plastic strain would be higher than the one recorded during the analyses.

5 Validation of the failure model on composite beams

The composite sandwich beam models consisted of five components: two 1.5-mm-thick aluminium faces, two 0.5-mm-thick adhesive layers and a 28-mm-thick PUR core. Two core geometries were considered, one

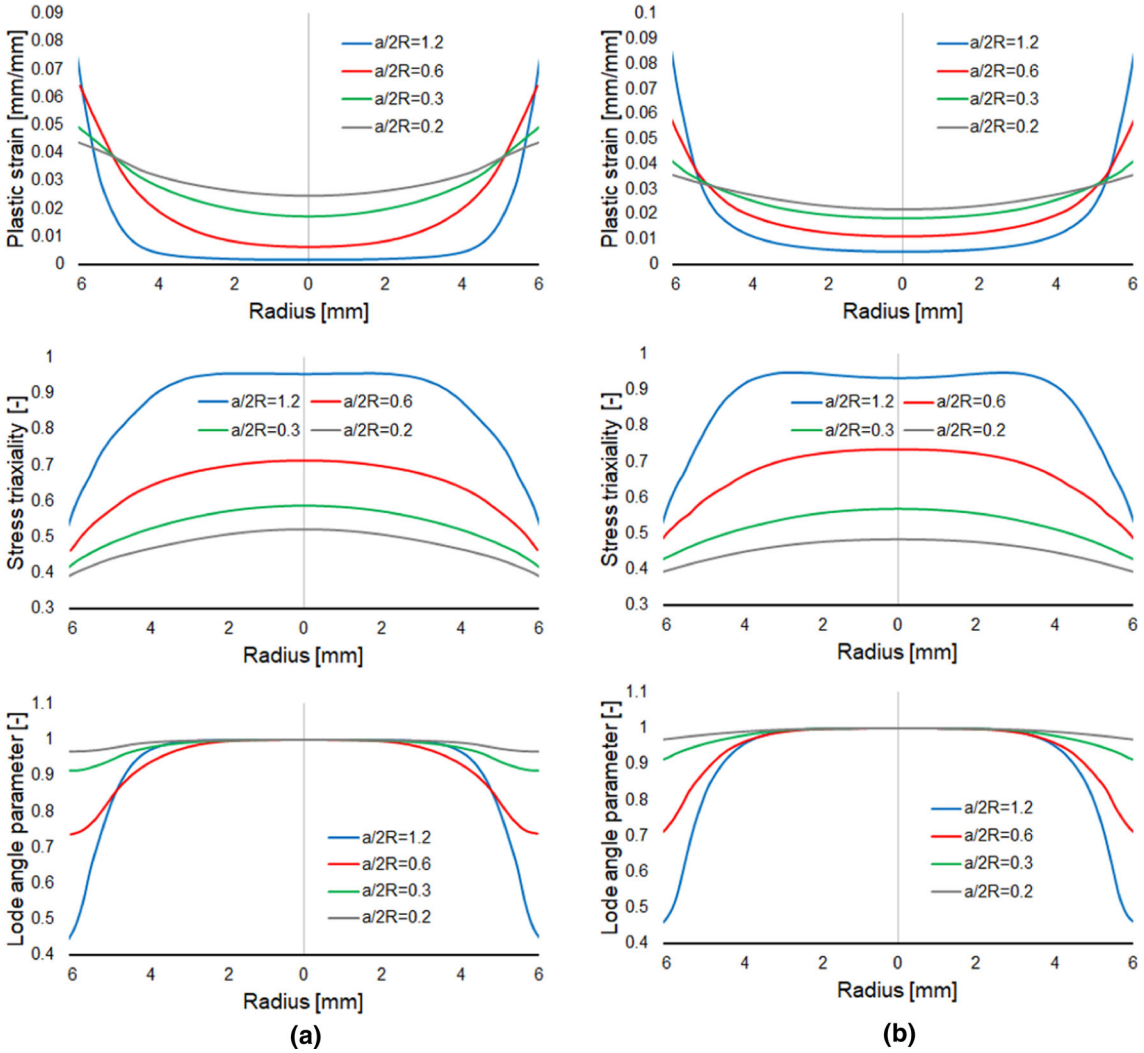

Fig. 12 Plastic strain, stress triaxiality and Lode angle parameter variation with radius for 100 kg/m^3 (**a**) and 300 kg/m^3 (**b**)

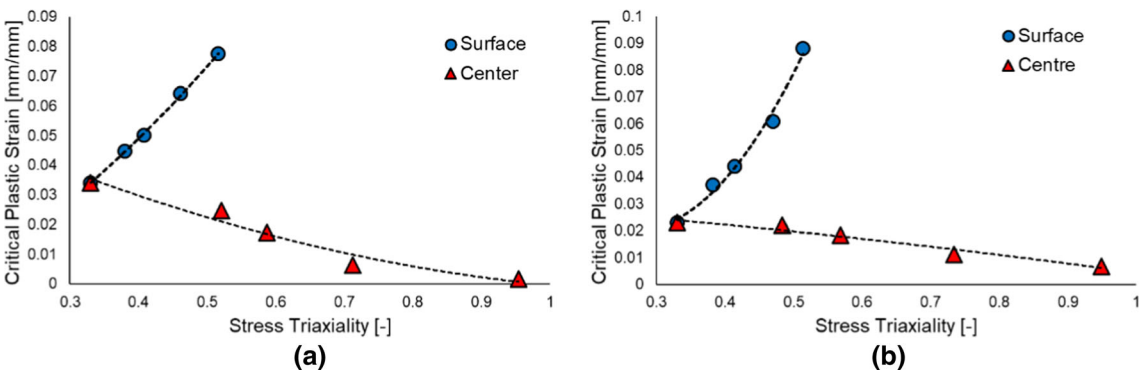

Fig. 13 Critical plastic strain variation with stress triaxiality in the centre on the specimen and at the surface for 100 kg/m^3 (**a**) and 300 kg/m^3 (**b**)

compact and one with a perforated pattern, with holes of ϕ7.5 mm and ϕ18 mm (Fig. 14a). The length of the beams was 400 mm and the width 70 mm.

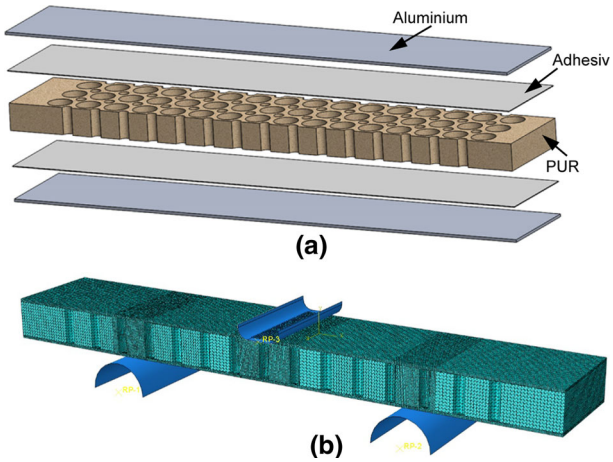

Fig. 14 Exploded view of the composite sandwich beam components, presenting the geometry of the perforated core (**a**) and the meshed model (**b**)

Table 1 Damage input data

	Equivalent plastic strain	Stress triaxiality	Lode angle parameter		Equivalent plastic strain	Stress triaxiality	Lode angle parameter
100 kg/m^3	0.0341	0.33	1	300 kg/m^3	0.023	0.33	1
	0.0447	0.371	0.968		0.0372	0.382	0.964
	0.0501	0.408	0.915		0.044	0.414	0.904
	0.0641	0.461	0.736		0.0609	0.471	0.699
	0.0775	0.516	0.434		0.0881	0.514	0.451

The numerical analyses were performed in Abaqus using the *Explicit* solver. The quasi-static analyses were conducted using mass scaling, in order to reduce the computational time. All components were meshed with C3D10M elements (second-order tetrahedral elements with modified formulation), the size varying between 0.5 mm and 2 mm (a number of 10^6 elements, Fig. 14b).

The supports consisted of 20 mm radius rigid cylinders and the indentor was a filleted 30 mm wide rigid prism. The interaction properties consisted of normal behaviour with the "hard contact" formulation and tangential behaviour with a penalty formulation and a friction coefficient of 0.3.

The material models used in the analyses were described above, the damage data input for the PUR foams being presented in Table 1.

The damage input data represent spatial curves (the equivalent plastic strain at failure as a function of the stress triaxiality and the Lode angle parameter). The software determines the critical plastic strain for other η and ξ values through linear interpolations [13]. For the damage evolution law, a linear formulation was used with a failure energy of $0.01J$, as all the specimens exhibited sudden failure (Fig. 10).

The force–displacement curves for the experimental data and numerical analyses are presented in Fig. 15 for the compact core and in Fig. 16 for the perforated core (Fig. 17).

The beams having compact cores with densities of 100 kg/m^3 exhibited core indentation, while the beams with 300 kg/m^3 compact core failed through face yielding and subsequent core fracture (Fig. 16). Both these phenomena were replicated in the numerical analyses. The resulting force–deflection results are in good accordance with the experimental data, with some discrepancies in modelling the post-yielding behaviour of the 100 kg/m^3 specimens.

The beams with perforated cores failed through core shear, images of the failed beams with perforated cores compared to the numerical results being presented in Fig. 18, showing a good agreement in terms of crack propagation. In both scenarios, the initial failure occurred at the foam–adhesive interface (due to the stress concentration caused by different materials properties) with the crack propagating along the interface. Midway between the support and the indentor, the crack shifted its path along a 45° angle, until it reached the opposing interface. Regardless of the fact that the numerical model did not capture the crack split that occurred

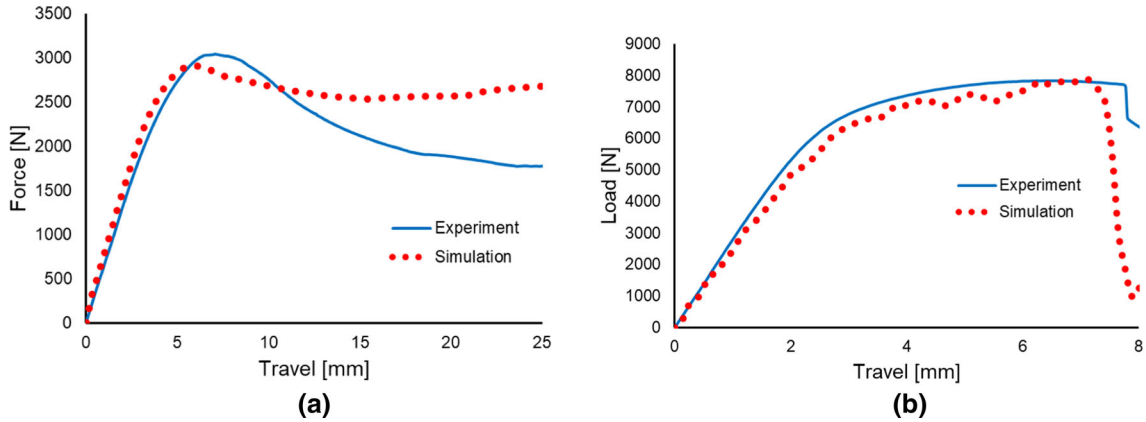

Fig. 15 Experimental and numerical results for flexural tests on composite beams with compact cores for 100 kg/m^3 cores (**a**) and 300 kg/m^3 cores (**b**)

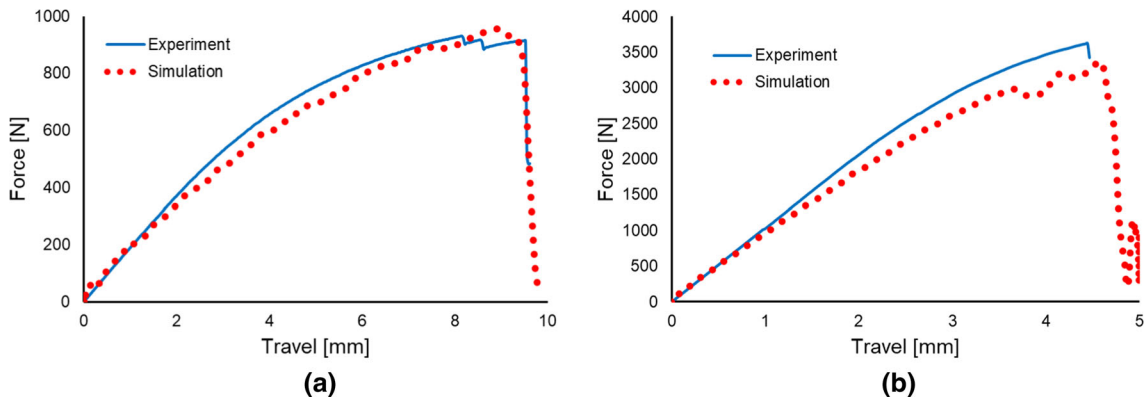

Fig. 16 Experimental and numerical results for flexural tests on composite beams with perforated cores for 100 kg/m^3 cores (**a**) and 300 kg/m^3 cores (**b**)

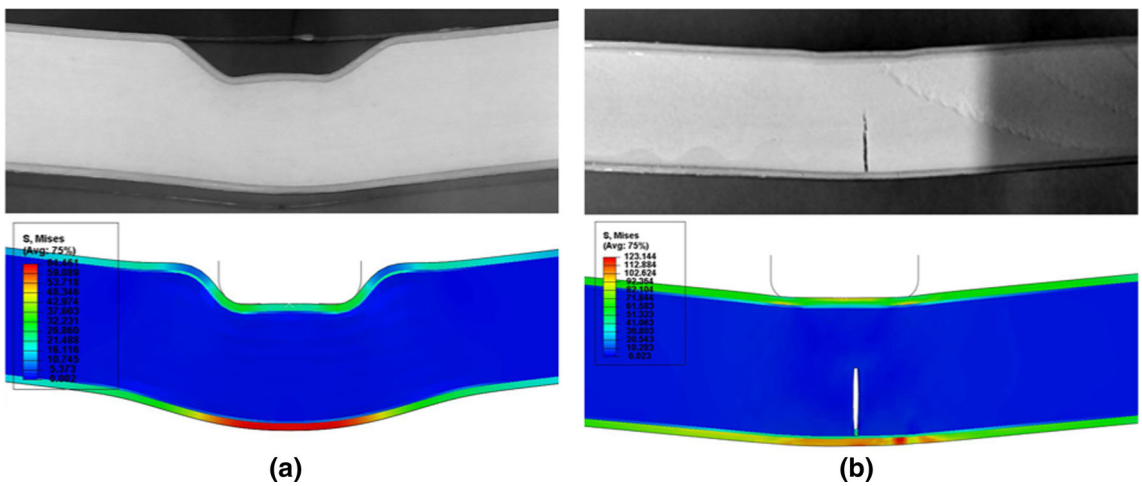

Fig. 17 Fractured specimen and simulation results for tests on composite beams with compact cores for 100 kg/m^3 (**a**) and 300 kg/m^3 (**b**)

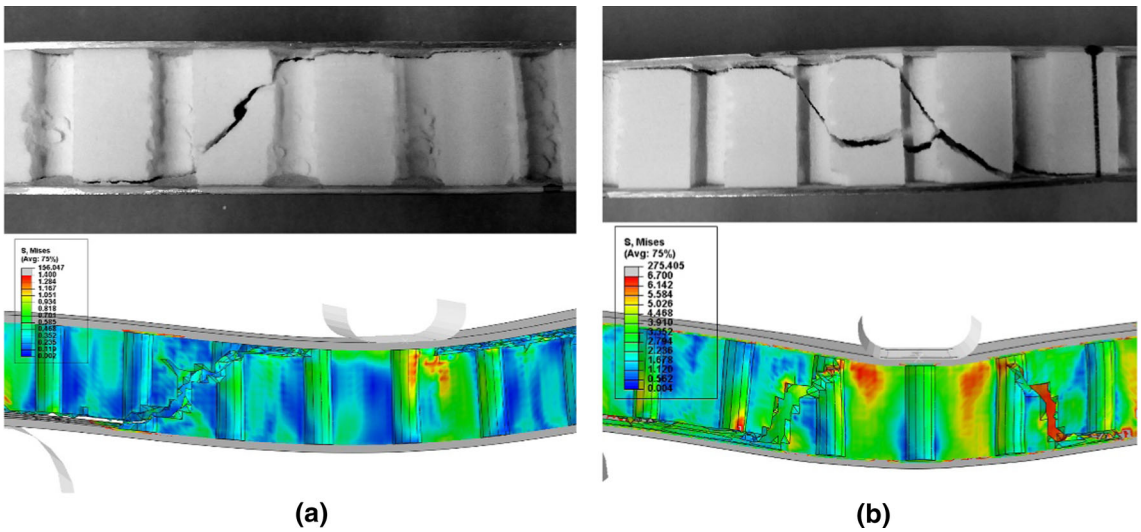

Fig. 18 Fractured specimen and simulation results for tests on composite beams with perforated cores for 100 kg/m^3 (**a**) and 300 kg/m^3 (**b**)

in the pictured 300 kg/m^3 specimen, the force–travel curves were in good agreement and the predicted failure deflections were accurate.

6 Discussions and conclusions

In this work, a damage model for semi-brittle materials was proposed, which assumes that the critical plastic strain is a function of the triaxial state of stress. The model was calibrated for positive stress triaxiality values, obtained through tests on cylindrical notched specimens with various radii, and was evaluated for flexural loadings of composite beams with aluminium faces and PUR cores.

Previous studies on the failure of rigid polyurethane foams assumed a linear elastic response, and the failure was evaluated with the help of fracture mechanics. Even though the investigated theories are able to predict the failure of PUR foams, their application to structures with complex geometries is cumbersome. This work assumes a different approach, which considers that failure occurs in the plastic domain, the critical strain being influenced by the triaxial state of stress, the third invariant of the stress deviator and the strain rate. This macroscopic failure model has the advantage of a facile numerical implementation, being suitable for the analysis of any type of structure and loading.

Though initially developed for metals and subsequently applied to polymers, the ductile damage model was shown in this study that is able to predict in a relatively accurate manner the damage and failure of the investigated semi-brittle materials subjected to complex stress states. The principle of void nucleation and growth can be considered valid for this class of materials, as this damage mechanism can be attributed to the fracture of the struts, which will determine void-like defects when a given number of cell walls fail.

Furthermore, this study shows that the triaxial state of stress is having a significant role in determining the failure of semi-brittle materials as more simplistic models; for example, ones based on principal stresses and strains at failure (used in XFEM analyses for instance) are unable to model the failure loci at different stress states. Consequently, this approach could be applied to other areas, such as fracture mechanics and fatigue. However, other continuum mechanics concepts, such as third invariant-dependent yield surfaces, should be applied in order to obtain an accurate response for this class of materials.

Numerical data obtained from the analyses on notched cylindrical specimens showed that the Lode angel parameter is crucial in understanding the failure in PUR foams. Thus, a complete failure model should include the influence of the Lode angle parameter, and further testing is required in order to obtain the failure surface ($\bar{\varepsilon}_{\mathrm{D}}^{\mathrm{pl}} = f(\eta, \xi)$) for the investigate PUR foams [10]. The influence of the strain rate was not considered, as only quasi-static tests were performed.

For the simulations performed on the notched cylindrical specimens, the use of 3D elements was chosen in detriment of a simplified 2D axisymmetric elements because of the increased number of integration points,

which determine a more accurate stress and strain distribution. In addition, identical C3D10M elements are used in the three-point bending analyses, assuring consistency between the material model evaluation and validation. The drawback of this approach is that the element size must be small in order to obtain convergence, which leads to long simulation times.

The simulation results for three-point bending showed a good agreement with the experimental values, even with the limited amount of data used to calibrate the failure model, concluding that this approach can be successfully applied in the design stage for components that are manufactured from PUR foams. Future work will focus on the determination of the failure loci for other stress triaxiality and Lode angle parameter values (obtained from biaxial, shear or Arcan tests) in order to obtain a complete failure surface.

Acknowledgements This work was supported by the Romanian National Authority for Scientific Research and Innovation, CCCDI—UEFISCDI, projects number PD 13/2018 and CCCDI—UEFISCDI, project number PN-III-P1-1.2-PCCDI-2017-0391/CIA_CLIM.

References

1. Gibson, L., Ashby, M.: Cellular Solids: Structure and Properties. Cambridge University Press, Cambridge (1997)
2. Şerban, D., Linul, E., Voiconi, T., Marsavina, L., Modler, N.: Numerical evaluation of two-dimensional micromechanical structures of anisotropic cellular materials: case study for polyurethane rigid foams. Iran. Polym. J. **24**, 515–529 (2015)
3. Şerban, D., Voiconi, T., Linul, E., Marşavina, L., Modler, N.: Viscoelastic properties of PUR foams: impact excitation and dynamic mechanical analysis. Materiale Plastice **52**, 537–541 (2015)
4. Marşavina, L., Şerban, D., Pop, C., Negru, R.: Experimental investigation of failure modes for sandwich beams. In: 16th International Conference on Fracture and Damage Mechanics. Key Engineering Materials, vol. 754, pp. 115–118 (2017)
5. Negru, R., Marşavina, L., Filipescu, H.: Evaluation of generalized MTS criterion for mixed-mode fracture of polyurethane materials. In: Advances in Fracture and Damage Mechanics XII, Key Engineering Materials, vol. 557–558, pp. 117–120 (2014)
6. Negru, R., Marşavina, L., Voiconi, T., Linul, E., Filipescu, H., Belgiu, G.: Application of TCD for brittle fracture of notched PUR materials. Theor. Appl. Fract. Mech. **80**, 87–95 (2015)
7. Marşavina, L., Berto, F., Negru, R., şerban, D., Linul, E.: An engineering approach to predict mixed mode fracture of PUR foams based on ASED and micromechanical modelling. Theor. Appl. Fract. Mech. **91**, 148–154 (2017)
8. Zapara, M.A., Tutyshkin, N.D., Müller, W.H., Weinberg, K., Wille, R.: A physico-mechanical approach to modeling of metal forming processes—part I: theoretical framework. Contin. Mech. Thermodyn. **20**, 231–254 (2008)
9. Hosford, W.: A generalized isotropic yield criterion. J. Appl. Mech. **39**(2), 607–609 (1972)
10. Bai, Y., Wierzbicki, T.: A new model of metal plasticity and fracture with pressure and Lode dependence. Int. J. Plast. **24**, 1071–1096 (2008)
11. Deshpande, V., Fleck, N.: Multi-axial yield behaviour of polymer foams. Acta Materialia **49**, 1859–1866 (2001)
12. Tutyshkin, N.D., Lofink, P., Müller, W.H., Wille, R., Stahn, O.: Constitutive equations of a tensorial model for strain-induced damage of metals based on three invariants. Contin. Mech. Thermodyn. **29**, 251–269 (2017)
13. Abaqus, "User's Manual," vol. Analysis (2017)
14. Şerban, D., Marşavina, L., Modler, N.: Finite element modelling of the progressive damage and failure of thermoplastic polymers in puncture impact. In: Proceedings of the XXIII Italian Group of Fracture Meeting, Procedia Engineering, vol. 109, pp. 97–104 (2015)
15. ISO 527, Plastics—Determination of Tensile Properties, International Standard Organization (1996)
16. Bleistein, T., Jung, A., Diebels, S.: A microsphere-based material model for open cell metal foams. Contin. Mech. Thermodyn. **32**, 255–267 (2020)
17. Şerban, D., Weber, G., Marşavina, L., Silberschmidt, V., Hufenbach, W.: Tensile properties of semi-crystalline thermoplastic polymers: effects of temperature and strain rates. Polym. Test. **32**, 413–425 (2013)
18. Şerban, D., Marşavina, L., Rusu, L., Negru, R.: Numerical study of the behavior of magnesium alloy AM50 in tensile and torsional loadings. Arch. Appl. Mech. **89**(5), 911–917 (2019)
19. ISO 6892-1, Metallic materials—tensile testing—part 1: method of test at room temperature. International Standard Organization (2019)
20. Murugesan, M., Jung, D.W.: Johnson Cook material and failure model parameters estimation of AISI-1045 medium carbon steel for metal forming applications. Materials **12**, 609 (2009)
21. Bao, Y., Wierzbicki, T.: On the cut-off value of negative triaxiality for fracture. Eng. Fract. Mech. **72**, 1049–1069 (2005)
22. Pineau, A., Benzerga, A., Pardeon, T.: Failure of metals I: Brittle and ductile fracture. Acta Materialia **107**, 424–483 (2016)
23. Bridgman, P.: Studies in Large Plastic Flow and Fracture—with Special Emphasis on the Effects of Hydrostatic Pressure. McGraw-Hill, New York (1952)